

A Dissertation Submitted to Hiroshima University
In Partial Fulfillment of the Requirements
for the Degree of Doctor of Science

Rheological behaviors of the subducting oceanic
crust: Evidences from naturally and
experimentally deformed blueschists
(沈み込む海洋地殻のレオロジー：天然と実験
により変形した青色片岩からの制約)

September 2013

Graduate School of Science, Hiroshima University
Department of Earth and Planetary Systems Science
Daeyeong Kim

A Dissertation Submitted to Hiroshima University
In Partial Fulfillment of the Requirements
for the Degree of Doctor of Science

Rheological behaviors of the subducting oceanic
crust: Evidences from naturally and
experimentally deformed blueschists
(沈み込む海洋地殻のレオロジー：天然と実験
により変形した青色片岩からの制約)

September 2013

Graduate School of Science, Hiroshima University
Department of Earth and Planetary Systems Science

Daeyeong Kim

Supervisor: Dr. Ikuo Katayama

Contents

1. Main thesis

Fabrics of naturally and experimentally deformed blueschists and its implications for rheological behaviors of the subducting plate (沈み込む海洋地殻のレオロジー：天然と実験により変形した青色片岩からの制約)
Daeyeong Kim

2. Published papers

- (1) Kim, D., Katayama, I., Michibayashi, K., Tsujimori, T. 2013a. Deformation fabrics of natural blueschists and implications for seismic anisotropy in subducting oceanic crust. *Physics of the Earth and Planetary Interiors*, **444**, 8–21, doi:10.1016/j.pepi.2013.06.011.
- (2) Kim, D., Katayama, I., Michibayashi, K., Tsujimori, T. 2013b. Rheological contrast between glaucophane and lawsonite in naturally deformed blueschist from Diablo Range, California. *Island Arc*, **22**, 63–73, doi:10.1111/iar.12003.

Main thesis

CONTENTS OF THE MAIN THESIS

Rheological behaviors of the subducting oceanic crust: Evidences from naturally and experimentally deformed blueschists

Abstract

Chapter I General introduction

1.1. Interesting events in subduction zone

1.2. Importance of blueschist

Chapter II Rheological contrast between glaucophane and lawsonite in naturally deformed blueschist from Diablo Range, California

2.1. Introduction

2.2. Sample description

2.2.1. Geological outline

2.2.2. Mineral assemblages and textures

2.2.3. Mineral chemistry

2.3. Microstructural and fabric analyses

2.4. Discussions

2.4.1. Deformation mechanisms of glaucophane and lawsonite

2.4.2. Deformation conditions for the Diablo Range blueschist

2.4.3. Rheological contrast between glaucophane and lawsonite

2.4.4. Slip systems and seismic anisotropy

2.5. Conclusions

Chapter III Deformation fabrics of natural blueschists and implications for seismic anisotropy in subducting oceanic crust

3.1. Introduction

3.2. Sample localities

3.2.1. The New Idria serpentinite body, Diablo Range, California

3.2.2. The Ward Creek schist, Franciscan Complex, California

3.2.3. The Omi serpentinite mélangé, Hida Mountains, Japan

- 3.3. Analytical techniques
- 3.4. Description of microstructures and chemical compositions of amphibole
- 3.5. Results
 - 3.5.1. Microscopic analyses
 - 3.5.2. EBSD patterns
 - 3.5.3. Seismic anisotropy
- 3.6. Discussion
 - 3.6.1. Deformational mechanisms of glaucophane, lawsonite, and epidote
 - 3.6.2. P–T conditions of deformation
 - 3.6.3. Seismic properties of lawsonite and epidote blueschists in the subducting oceanic slab
- 3.7. Conclusions

Chapter IV Deformation mechanisms of glaucophane and lawsonite: Implications from experimentally deformed blueschists

- 4.1. Introduction
- 4.2. Experimental procedures
- 4.3. Results
 - 4.3.1. Mechanical data of pure shear experiments
 - 4.3.2. Microstructures of specimens deformed under simple shear regime
 - 4.3.3. EBSD measurements
- 4.4. Discussion and conclusions

Chapter V Summary

Chapter VI Acknowledgements

Chapter VII References

**Rheological behaviors of the subducting oceanic crust: Evidences from naturally
and experimentally deformed blueschists**

(沈み込む海洋地殻のレオロジー：天然と実験により変形した青色片岩
からの制約)

Daeyeong Kim

ABSTRACT

Subduction zone could generate strong stresses especially within subducting slab and also it makes special high pressure and low temperature environments. Ergo study on blueschist is important to understand active stresses in subduction zone and in addition to reveal geofluid circulations owing to abundant hydrous phases in it. Fabric analyses of naturally and experimentally deformed blueschists were investigated to delineate its implications for seismic anisotropy and source of seismicity in subducting oceanic crust.

The first subproject dealt rheological contrast of glaucophane and lawsonite in natural blueschist from the New Idria serpentinite body, Diablo Range, California. Anhedral to subhedral glaucophane shows strong crystal-preferred orientations (CPOs) with small grain size, irregular grain boundary, and high aspect ratio, indicating recovery and dynamic recrystallization possibly accommodated by dislocation creep. Euhedral to subhedral lawsonite deforms by rigid body rotation due to angular or straight grain boundary. Glaucophane-rich layer contains higher aspect ratio, lower angle to foliation, stronger CPOs, and higher seismic anisotropy of glaucophane and lawsonite than those in lawsonite-rich layer, suggesting the strain localization into the glaucophane-rich layer. On the other hand, glaucophane has higher aspect ratio, lower angle to foliation, stronger CPOs, and higher seismic anisotropy than lawsonite,

supporting the strain localization into the glaucophane rather than lawsonite. All the results of the study therefore imply the dominant roles of glaucophane rather than lawsonite for rheological behaviors of subducting oceanic crust.

Seismic anisotropy of lawsonite and epidote blueschists from the Diablo Range and Franciscan Complex in California, and the Hida Mountains in Japan was investigated for the second subproject. Glaucophane is characterized by very fine grains aligned along the foliation, high aspect ratio, and strong CPOs identified by a (100)[001] system. These results with a bimodal distribution of grain size in some specimens probably suggest recovery and dynamic recrystallization of glaucophane. Though lawsonite and epidote have high aspect ratio and strong CPOs of (100)[010], straight grain boundary and euhedral crystal shape indicate rigid body rotation as predominant deformation mechanism. Seismicity calculations of glaucophane from CPOs show the fastest propagation of P-waves along the lineation, and the S-wave polarization parallel to the foliation ($AV_P = 20.4\%$, $AV_S = 11.48\%$), implying possible generation of a trench-parallel seismic anisotropy due to the slowest V_S polarization being normal to the subducting slab. Lawsonite has the fast propagation of P-waves subnormal to the foliation lawsonite and S-wave polarization subnormal to the [001] maxima ($AV_P = 9.6\%$, $AV_S = 19.88\%$), indicating probable occurrence of a trench-normal anisotropy. Epidote displays similar patterns of seismic anisotropy with glaucophane nevertheless intensity is relatively low ($AV_P = 9.0\%$, $AV_S = 8.04\%$). The AV_S of lawsonite blueschist (5.6%–9.2%) therefore is weaker than that of epidote blueschist (8.4%–11.1%), in consistent to the occurrence of strong trench-parallel anisotropy beneath Ryukyu arc and weak trench-parallel anisotropy beneath NE Japan. Intensity of seismic anisotropy suggests that glaucophane and lawsonite can satisfactorily cause trench-parallel seismic anisotropy beneath NE Japan. The results

consequently demonstrate that trench-parallel seismic anisotropy in forearc beneath NE Japan could be attributed to the combination of glaucophane and lawsonite, and also that trench-normal anisotropy in backarc could possibly be generated by seismic anisotropy of lawsonite.

Thirdly deformation mechanisms of glaucophane and lawsonite in experimentally deformed blueschists were conducted using a Griggs-type solid-medium apparatus housed at Hiroshima University. Mechanical data of pure-shear experiments at 500 °C and 0.5–2 GPa display pressure-sensitive increase of shear stress at low confining pressure and pressure-insensitive increase of stress at high pressure, probably influenced by a change of deformation mechanism of blueschist. Brittle deformation features in simple-shear experiments investigated at 400–500 °C and 1–2.5 GPa are dominant at 1–2 GPa experiments, in contrast to abundant strain-localized area at 2.5 GPa. Glaucophane has a systematic decrease of *J*-index with an increase of shear strain and confining pressure, and angular change of slip plane to shear direction is similar to that of strain ellipsoid at >2 GPa. These results might be attributed to the change of deformation behaviors of glaucophane from brittle failure to brittle-ductile transition at ~2 GPa. On the other hand, though lawsonite exhibits angle of slip plane to shear direction is comparable to that of strain ellipsoid at 2.5 GPa, relatively abundant relict phases in specimens deformed at 2.5 GPa, and weak relation among *J*-index, shear strain, and confining pressure indicate no change of deformation mechanism within the experimental conditions. The results of the study therefore imply brittle or semi-brittle behaviors of glaucophane as a source of observed seismicity in subducting oceanic crust beneath NE Japan. However additional experiments at higher pressure are needed to reveal the upper limit of brittle-ductile transition.

Chapter I

GENERAL INTRODUCTION

1.1. Interesting events in subduction zone

Subduction zone is one of the most active areas in the upper crust and mantle hence there are lots of interesting topics we can find. Oceanic crust, formed at mid-ocean ridge, meets continental crust in subduction zone and subducts beneath the continental crust by difference in density, related with the age of oceanic crust, then cause variations in subducting angle. By subduction of crustal materials, fluid could be delivered into deeper mantle, therefore fluid circulation could be one of the most interesting subjects in subduction zone. Also by environmental change, specific rock types and phases stabilized at high pressure and low temperature can be formed. For instance, basalt transforms via blueschist to eclogite with relatively low geothermal gradients in subduction zone.

Kita et al. (2006) firstly reported the distribution of seismicity within subducting oceanic crust beneath NE Japan that is characterized by abundant seismicity in blueschist-facies, relatively rare in transition zone, and no in eclogite-facies. The results imply the occurrence of seismicity possibly originated by the phase transition from blueschist to eclogite. Thus deformation behavior or dehydration embrittlement of blueschist could be the cause of seismicity in subducting oceanic crust. Especially blueschist contains a large amount of hydrous phases such as glaucophane, lawsonite, and epidote, therefore study for deformation behavior or dehydration embrittlement of blueschist is crucial to be a subject for understanding the source of the seismicity distribution in subducting oceanic crust especially beneath NE Japan.

Subduction zone has specific seismic anisotropic patterns. Using seismic properties, we can access the information about the origin of the slab, the nature of the mantle wedge, slab rollback, and delineate back-arc spreading and the presence of melt (e.g., Wiens et al., 2008). Particularly the polarization directions of fast propagations and the delay time between the arrivals of fast and slow shear-waves can detect trench-parallel and trench-normal shear-waves in subduction zone. The causes of trench-parallel seismic anisotropic patterns were usually estimated to be the flow of the mantle (Long and Silver, 2008) or the crystal preferred orientations (CPOs) of minerals such as olivine (Jung and Karato, 2001) and serpentine (Katayama et al., 2009). However precise origin of the seismic anisotropy is difficult to detect by the shear-wave splitting method, therefore additional studies especially for the subducting slab need to be followed. During the rock-type change from blueschist to eclogite, dehydration occurs due to different mineral assemblages in both rocks. The fluid caused by dehydration generates large volume of magma hence the rock-type change could be also related with occurrence of volcanic arc. Accordingly complex seismic anisotropic patterns characterized by trench-parallel in forearc and trench-normal in backarc beneath NE Japan could be related with the rock-type change from blueschist to eclogite. Especially during the rock type change, glaucophane in blueschist is consumed and omphacite in eclogite is formed. Therefore the deformation behavior or dehydration of blueschist could be the key to delineate the source of complex anisotropic patterns beneath NE Japan.

1.2. Importance of blueschist

Blueschist, formed by transformation of basalt (oceanic crust) at ~15 km depth (Fig. 1.1), contains lots of fluid (~5.9 wt% in lawsonite blueschist and ~2.6 wt% in

epidote blueschist; Peacock, 1993) within defects and hydrous minerals such as glaucophane (~2.0–2.5 wt%), lawsonite (10–11.5 wt%), and epidote (~2.0 wt%) (Schmidt and Poli, 1998; Sinogeikin et al., 2000; Mao et al., 2007; Bezacier et al., 2010). In addition, these hydrous phases contain strong seismic anisotropy of single crystal (38.1 % of AV_P and 27.3 % of AV_S for glaucophane, 74 % of AV_S and V_P/V_S for lawsonite and 1.1 % of AV_P for epidote) (Bezacier et al., 2010; Sinogeikin et al., 2000; Fujimoto et al., 2010). However the study for blueschist is rare owing to scarce occurrence in the crust, therefore the study especially for deformation behaviors of blueschist could be fundamentally significant to understand many phenomena related with seismic observations in subduction zone.

Here I record some results of projects for blueschist conducted during my PhD course. This study was carried on by three subprojects using naturally and experimentally deformed blueschists. Strain is normally localized into specific minerals or layers (e.g., Herwegh et al., 2008), thus in Chapter 2, I described rheological contrasts between glaucophane and lawsonite in naturally deformed blueschist from Diable Range, California. In Chapter 3, the results of interesting seismic anisotropic patterns calculated from crystal-preferred orientation of glaucophane, lawsonite, and epidote in natural blueschists are presented. Through the results, I delineate the main source of complex seismic anisotropic patterns beneath NE Japan. Finally in Chapter 4, deformation behaviors of glaucophane and lawsonite in experimentally deformed blueschists were investigated using a Griggs-type solid medium apparatus at Hiroshima University. By the subproject, the reason why seismicity in subducting oceanic crust is distributed only in blueschist, rather than in eclogite is fundamentally approached.

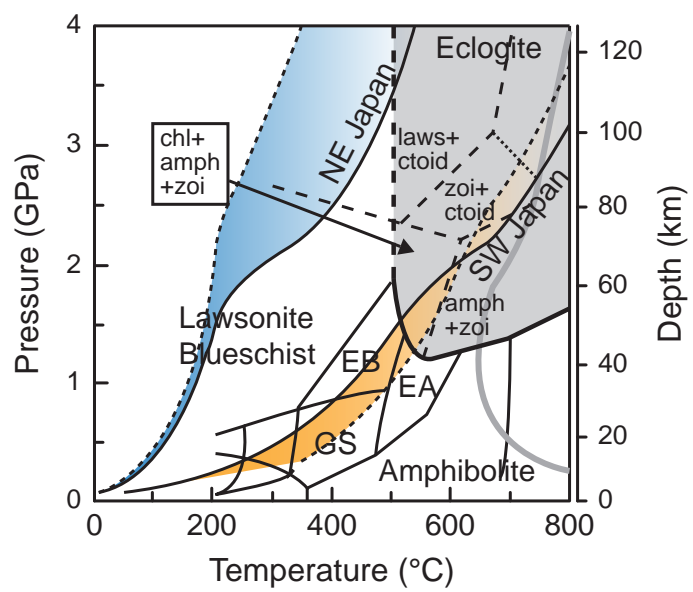


Fig. 1.1. A phase diagram showing transformation of oceanic crust (modified from Peacock and Wang, 1999).

Chapter II

RHEOLOGICAL CONTRAST BETWEEN GLAUCOPHANE AND LAWSONITE IN NATURALLY DEFORMED BLUESCHIST FROM DIABLO RANGE, CALIFORNIA

Main contents of this chapter have been published in *Island Arc* (2013, vol 22, 63–73, doi:10.1111/iar12003).

Abstract

Deformation microstructures for a lawsonite blueschist from the New Idria serpentinite body, Diablo Range, are examined to unravel rheological behaviors of glaucophane and lawsonite, which constitute main mineral assemblages of subducting oceanic crust at relatively cold geotherm. Developments of crystal-preferred orientations (CPOs) with small grain size, irregular grain boundary and high aspect ratio of glaucophane signify deformation mechanism as recovery and dynamic recrystallization possibly accommodated by dislocation creep, while lawsonite deforms by rigid body rotation on the basis of euhedral grains with angular or straight grain boundary. Higher aspect ratios, lower angle to foliation and stronger CPOs of both minerals in glaucophane-rich layer rather than those in lawsonite-rich layer indicate the strain localization into the glaucophane-rich layer. Additionally fabric strength (the degree of crystal alignment) and seismic anisotropy are higher in the glaucophane-rich layer than that of the lawsonite-rich layer, which is consistent with the microstructural analyses. All my results therefore suggest the dominant roles of

glaucophane rather than lawsonite for rheological behavior and seismic anisotropy of blueschist.

2.1. Introduction

Investigations on strength contrast among minerals or competence contrast among layers can be important to understand geological problems such as the depth of earthquakes and viscous coupling between the crust and mantle. Especially in subduction zone, dehydration of hydrous phases and formation of high-pressure minerals occur with high stress regime. Those phenomena are crucial to comprehend the crust-mantle circulations.

Blueschist usually forms at low-temperature and high-pressure conditions by subduction and metamorphism of oceanic crust originated from mid-ocean ridge basalt (MORB). High-pressure minerals such as glaucophane and lawsonite can be preserved as an inclusion that formed during subduction or a matrix that grew during exhumation. Although dissolution-precipitation creep is one of the dominant deformation mechanism of calcic amphibole at low temperature (e.g., Imon et al., 2004), rigid-body rotation (Ildefonse et al., 1990), dislocation creep with recovery (Reynard et al., 1989) and dynamic recrystallization (Zucali et al., 2002) are possible deformation mechanisms of natural glaucophane deformed at relatively high pressures. Deformation mechanisms and slip systems of glaucophane during retrograde stage, however, are poorly understood.

I therefore conducted fabric analyses of lawsonite blueschist from the New Idria serpentinite body in Diablo Range, California to delineate rheological behaviors of subducting oceanic crust. The body underwent blueschist-facies overprint during exhumation (Tsujimori et al., 2007), therefore it represents the rock deformed during

retrograde process which might be similar deformational conditions with subduction (especially in the case of grain size). Deformation mechanisms and relative strength between glaucophane and lawsonite are mainly discussed.

2.2. Sample description

2.2.1. Geological outline

The New Idria serpentinite body in Diablo Range, a part of the Coalinga anticline, borders the Upper Cretaceous Panoche and Moreno Formations of the Great Valley Group and Franciscan Complex. The body containing numerous tectonic blocks of greenstone and low-grade blueschists comprises primary chrysotile-lizardite serpentinite and minor antigorite serpentinite which have been a moderately depleted harzburgite based on chemical compositions of relict minerals (Coleman, 1980; Tsujimori et al., 2007). The presence of high-grade tectonic blocks composed of retrograded eclogite and garnet-amphibolite indicates the origin of the New Idria serpentinite from mantle depth (Tsujimori et al., 2007). The investigated lawsonite blueschists were collected as a boulder at near eclogite locality along the Clear Creek (Fig. 2.1).

2.2.2. Mineral assemblages and textures

In this study, I selected a sample, which contains distinctively representative two parts, a glaucophane-rich layer (GRL) and a lawsonite-rich layer (LRL) (Fig. 2.2): This helps to clarify rheological contrast between glaucophane and lawsonite, and its effects to active slip systems and seismic anisotropy of subducting oceanic crust. The GRL primarily comprises glaucophane (89%), lawsonite (8%) and rare phengite around lawsonite with minor accessory minerals (titanite and apatite) (Figs. 2.2A and

C). Glaucophane as a main component of the matrix is highly foliated and elongated with very fine grain size, suggesting possible formation of glaucophane during the exhumation process. Often irregular grain boundary of glaucophane is observed (Fig. 2.3). Lawsonite having subhedral to euhedral shape with straight grain boundaries is preserved as porphyroclasts wrapped mostly by glaucophane. The LRL chiefly comprises glaucophane (64%), lawsonite (21%) and phengite (11%) enclosing lawsonite (Figs. 2.2B and D). Grain sizes of minerals are somewhat larger than those in the GRL.

2.2.3. Mineral chemistry

Major elements of these minerals were measured using the JEOL JXA-8200 (EPMA), housed at Hiroshima University. I employ the average of maximum and minimum estimates on the basis of total cations as 13 for T- and C- sites, and 15 for T-, C- and B-sites, respectively, for the contents of ferric iron in amphibole (Table 1) (Leake et al., 1997). All sodic amphiboles ($^{[B]}Na \geq 1.5$) in both GRL and LRL are classified as glaucophane by definitions such as $(Na + K)_A < 0.50$, $Mg/(Mg + Fe^{2+}) \geq 0.5$, and $^{[6]}Al \geq Fe^{3+}$ (Fig. 2.4). Only few grains in the LRL have core-rim structures characterized by the increase of $Fe^{3+}/(Fe^{3+} + ^{[6]}Al)$ defining tschermakite substitution and the decrease of Al and Na contents from core to rim, classifying the rim composition as winchite or actinolite (Fig. 2.4). The decrease of Al contents from the core to the rim suggests the formation of amphibole during retrograde stage, due to the systematic correlation between pressure and Al_2O_3 content of sodic amphibole (Maruyama et al., 1986). In addition, mineral assemblages (Gln + Lws + Ph + Ttn) are similar to those in blueschist-facies overprinting stage of high-grade blocks from New Idria (Tsuji-mori et al., 2007), except the lack of jadeite. I therefore adopt

temperature ranges of 200–290 °C for pumpellyite-zone metabasites (Maruyama and Liou, 1988) and pressure ranges (> 1.0 GPa) for Jd + Qz stability field (Tsuji-mori et al., 2007) in this sample.

2.3. Microstructural and fabric analyses

Measurements of aspect ratios, angle to the foliation and grain size for minerals in XZ sections (the plane perpendicular to the foliation and parallel to the lineation) of the GRL and LRL were conducted by the image-analysis software ImageJ 1.44, in which best-fit ellipses for each grain were computed for reducing the complexity of various shapes (Fig. 2.3C) (e.g., Mezger, 2010). Aspect ratios of glaucophane in each domain are distinctively diverse (12.8 for average in the GRL and 6.0 in the LRL), in contrast to relatively alike results of aspect ratios in lawsonite (5.0 for average in the GRL and 3.6 in the LRL) (Fig. 2.5, Table 2.2). Angles to foliation of glaucophane in both layers exhibit almost similar results within 30°, while lawsonite in the LRL shows more scattered patterns than that in the GRL. Grain size of glaucophane in the GRL (7 μm of mean value) is relatively smaller than that in the LRL (12 μm), while distributions of grain size for lawsonite are comparable (18 μm in the GRL and 20 μm in the LRL) (Fig. 2.5, Table 2.2).

The Kikuchi bands were acquired for XZ sections and analyzed using the HKL–EBSD system attached to the Hitachi S-3400N at Shizuoka University. To unravel the effects of chemical zonings in glaucophane and lawsonite, automatic mappings (1 μm of step size) for each domain were carried out. After I confirmed identical crystallographic orientation throughout the whole grain, the EBSD patterns were manually indexed. Pole figures were plotted using the software PFctf, made by D. Mainprice and J- and M-indexes were employed for estimating fabric strength

(Mainprice and Silver, 1993; Ismaïl and Mainprice, 1998; Skemer et al., 2005). As a result, glaucophane and lawsonite in both layers have a certain and alike CPOs for each mineral except slightly scattered patterns in the LRL. Glaucophane exhibits the [001] axes parallel to the lineation, the (100) planes vertical to foliation plane, and relatively weak central maxima in the (010) planes (Figs. 2.6A and C). Glaucophane in the GRL ($M = 0.20$, $J = 18.0$) displays higher fabric strength than that in the LRL ($M = 0.18$, $J = 16.0$) (Fig. 2.6 and Table 2.2). The CPOs of lawsonite are characterized by vertical maxima in the [001] axes, horizontal maxima in the [010] axes, and weak patterns in the [100] axes (Figs. 2.6B and D). M- and J-indexes of lawsonite in the GRL are estimated as $M = 0.21$ and $J = 9.6$, while those in the LRL are $M = 0.15$ and $J = 7.8$ (Fig. 2.6 and Table 2.2).

I computed the seismic properties of glaucophane and lawsonite in the GRL and LRL. The seismic anisotropy of P-wave (AV_P) is defined by the maximum and minimum velocities in two different propagating paths, hence the percentage AV_{Pmax} can be calculated using the formula $200(V_{Pmax} - V_{Pmin}) / (V_{Pmax} + V_{Pmin})$. The S-wave anisotropy (AV_S) is described as two different velocities of two orthogonally polarized S-waves separately propagated through an anisotropic medium, therefore the percentage AV_{Smax} is calculated by the formula $200(V_{S1} - V_{S2}) / (V_{S1} + V_{S2})$, in which V_{S1} and V_{S2} are faster and slower velocities, respectively. The elastic constants (C_{ij}) of glaucophane (Bezacier et al., 2010) and lawsonite (Sinogeikin and Bass, 2000) are employed for calculating seismicity of crystals with Voigt–Reuss–Hill averaging scheme. The V_P , AV_S and orientation of V_{S1} polarization of glaucophane and lawsonite in both layers are projected to lower hemispheres (Fig. 2.7). Seismic velocities in the GRL are 6.73–8.68 km/s of V_P , 4.34–4.93 km/s of V_{S1} and 4.27–4.57 km/s of V_{S2} for glaucophane with strong anisotropy ($AV_{Pmax} = 25.3\%$ and $AV_{Smax} = 13.9\%$) and 7.68–

8.55 km/s of V_P , 4.11–4.55 km/s of V_{S1} and 3.64–4.29 km/s of V_{S2} for lawsonite with P- and S-wave seismic anisotropy as 10.7% and 21.3% (Figs. 2.7A and B). The V_P , V_{S1} and V_{S2} in the LRL are calculated to 7.15–8.74 km/s, 4.52–4.82 km/s and 4.29–4.60 km/s for glaucophane ($AV_P = 20.0\%$ and $AV_S = 9.9\%$) and 7.65–8.35 km/s, 3.93–4.56 km/s, 3.74–4.19 km/s for lawsonite ($AV_P = 8.8\%$ and $AV_S = 19.4\%$), respectively (Figs. 2.7C and D). The V_{Pmax} of glaucophane in both layers is developed along the lineation parallel to the [001] axes and the AV_{Smax} and V_{S1max} polarization are established as girdle type along the foliation perpendicular to the (100) planes in CPOs, while lawsonite shows the V_{Pmax} normal to the foliation associated with the [001] axes and the AV_{Smax} and V_{S1max} polarization in central maxima.

2.4. Discussions

2.4.1. Deformation mechanisms of glaucophane and lawsonite

Microstructural investigations suggested cataclastic deformation (Nyman et al., 1992), rigid-body rotation (Ildefonse et al., 1990; Siegesmund et al., 1994) and dynamic recrystallization (Cumbest et al., 1989) as possible deformation mechanisms of natural amphibole. Glaucophane is a relatively weak mineral among amphiboles attributed to diverse slip systems and an inclination for recovery and recrystallization processes (Reynard et al., 1989; Zucali et al., 2002). In addition, small grain size is normally attributed to strain-induced recrystallization during or after crystal plastic deformation (e.g., Drury and Urai, 1990). Glaucophane in the analyzed samples shows small grain size (possibly owing to grain size reduction) and well-developed CPOs normally considered as products of dynamic recrystallization (Díaz Aspiroz et al., 2007). The result can be also supported by grain size distribution of glaucophane into $< 2 \mu\text{m}$ and 4–22 μm for the LRL and possibly $< 2 \mu\text{m}$ and 4–14 μm for the GRL

(Fig. 2.5). Therefore glaucophane is likely deformed by recovery and dynamic recrystallization mechanisms perhaps accommodated by dislocation creep. Irregular or curved grain boundaries of glaucophane designate the presence of annealing and grain growth ascribed to the reduction of interfacial free energy in a low stress regime (Fig. 2.3B) (Evans et al., 2001). Dissolution and precipitation creep can be operated under low temperatures at the presence of aqueous fluids; however, this may not be the main controlling mechanism for the analyzed sodic amphiboles because of the stronger fabric for fine-grained glaucophane and weak chemical zoning, whereas calcic amphiboles are deformed by dissolution and precipitation as evident by shape preferred orientation and clear chemical zoning (e.g., Imon et al. 2004). On the other hand, deformation mechanism of lawsonite is poorly understood. Lawsonite in the sample exhibits also relatively strong CPOs, however, grains are euhedral with angular or straight boundary and are partly wrapped by phengite (Fig. 2.2). The wide range of stability field of lawsonite with these microstructures intimates that predominant deformation mechanism is possibly rigid body rotation.

2.4.2. Deformation conditions for the Diablo Range blueschist

Lawsonite eclogite normally occurs at deeper than 45 km depth in subduction zones (Tsuji-mori et al., 2006), nevertheless its exhumation to the surface is rare without alteration. The Diablo Range in California exceptionally maintains unaltered lawsonite eclogite, implying rapid exhumation probably due to slab breakoff. Lawsonite in the analyzed sample might be formed during prograde metamorphism and suffered maximum pressure condition (1.3 GPa) of the New Idria serpentinite body (Tsuji-mori et al., 2007). On the other hand, glaucophane may appear during a retrograde *P-T* path on the basis of chemical compositions in the core (glaucophane)

and rim (winchite or actinolite). The strongly aligned grains for both lawsonite and glaucophane are proved by low degrees of angle to the foliation (Fig. 2.5), indicating the presence of deformation during or after the blueschist-facies overprinting. The development of CPO might be imputed to the flow of dynamically recrystallized small grains, suggesting syn-kinematic microstructures. Consequently main deformation event to form these microstructures was occurred at temperatures ranging from 200 to 290°C and pressures over 1.0 GPa (Tsujimori et al., 2007). The deformation at a relatively higher pressure may cause the operation of plastic deformation in sodic amphibole rather than the cataclastic deformation.

2.4.3. Rheological contrast between glaucophane and lawsonite

Deformation is generally concentrated into specifically weak minerals or layers (e.g., Ebert et al., 2007), therefore strength contrast between glaucophane and lawsonite against deformation can help to understand the rheology of the subducting slab. For examining this concept, I assume that the analyzed rock is composed only of two phases, glaucophane and lawsonite. Microscopic observations designate that grains of glaucophanes and lawsonite in the GRL are comparatively smaller than those in the LRL (Fig. 2.2). The results of image analyses for glaucophane and lawsonite in the GRL intimate higher aspect ratios, larger grain size and well-aligned long-axes along foliation than those in the LRL (Fig. 2.5). Higher fabric strength in the GRL is also revealed based on M- and J-indexes, which is corresponding to aspect ratio (Fig. 2.8 and Table 2.2). All lines of evidence demonstrate that strain is localized into the GRL rather than the LRL, denoting glaucophane is weaker than lawsonite against deformation. My study, therefore, proves that rheology of subducting oceanic crusts can be primarily influenced by glaucophane. These are in agreement with the

results of Teyssier et al. (2010) who reported lawsonite vorticity owing to the treats of lawsonite and glaucophane as a rigid grain and a ductile matrix, respectively.

2.4.4. Slip systems and seismic anisotropy

Slip systems are usually managed by physical variables such as pressure (P), temperature (T), stress (strain or strain rate), and water fugacity (Carter and Avé Lallemant, 1970; Zhang and Karato, 1995; Jung and Karato, 2001; Jung et al., 2006). The analyzed sample experienced almost comparable histories for P , T and water fugacity hence in this study strain could be the only concern for slip systems of glaucophane in the GRL and the LRL. Pole figures of glaucophane show vertical maxima in the (100) planes and horizontal maxima in the [001] axes, insinuating slip plane and direction, respectively (Figs. 2.5A, C). The results advocate that the strength of stress or strain can scarcely influence the slip systems of glaucophane. Duplicate glaucophane LPOs, which can be used for estimating the slip system, are reported for lawsonite blueschists deformed at 2 GPa and 430 °C (Teyssier et al., 2010) and at 0.7–0.9 GPa and < 350 °C (Fujimoto et al., 2010). These reveal same slip systems of glaucophane in diverse P - T conditions when other factors (strain and water fugacity) are fixed, therefore glaucophane possibly has identical slip systems during subduction or exhumation.

The CPOs of lawsonite show the [010] axis subparallel to the lineation and the [001] axis normal to the foliation, possibly developed by solid body rotation (Figs. 2.5B, D). This pattern is different from that reported in lawsonite, (100)[001] (Teyssier et al., 2010) and (001)[100] (Fujimoto et al., 2010). These disagreements are probably attributed to the difference in deformation mechanism, deformational P-

T conditions or degree of rotation, nevertheless strain rate, stress (or strain) and water fugacity are needed to contemplate.

To evaluate impacts of strain localization to seismic anisotropy, I computed the seismic properties of glaucophane and lawsonite in the GRL and LRL (Fig. 2.7). The degree of seismic anisotropy of glaucophane and lawsonite in the LRL is relatively higher than those in the GRL, in agreement with aspect ratio and fabric strength (Fig. 2.7 and Table 2.2). Those are mainly caused by strain localization, because they were calculated from CPOs. However glaucophane and lawsonite have different CPOs, therefore seismic anisotropy of rock mass were computed for comprehending the effects of mineral abundances (Fig. 2.9) (Mainprice et al., 2000). The highest AV_{Pmax} for the GRL and LRL was calculated as 20.0 and 25.3%, respectively, for the rock comprising 100% glaucophane, while the highest AV_{Smax} as 19.4 and 21.3%, respectively, for the rock containing 100% lawsonite. The lowest AV_{Pmax} and AV_{Smax} are modeled as the rock composed of glaucophane 70% and lawsonite 30% for AV_P , and of glaucophane 30% and lawsonite 70%. The distinctive ‘concave’ feature is probably attributed to directions of seismic anisotropy originated from CPOs (Figs. 2.6 and 2.7). Consequently I denote here that seismic anisotropy of rock mass especially composing of highly anisotropic phases is controlled by the abundance of rock-forming minerals.

2.5. Conclusions

In summary, I investigated fabric analyses of a Diablo Range blueschist, which preserves distinctive two layers mostly composed of glaucophane and lawsonite. Results of higher aspect ratio, lower angle to the foliation and higher fabric strength of glaucophane in representative two layers advocate strain partitioning into the

glaucophane-rich layer (GRL) rather than the lawsonite-rich layer (LRL), and also indicate weaker glaucophane than lawsonite against deformation. To conclude, my discovery supports the idea that glaucophane mainly manages rheology and seismic anisotropy of subducting oceanic crusts.

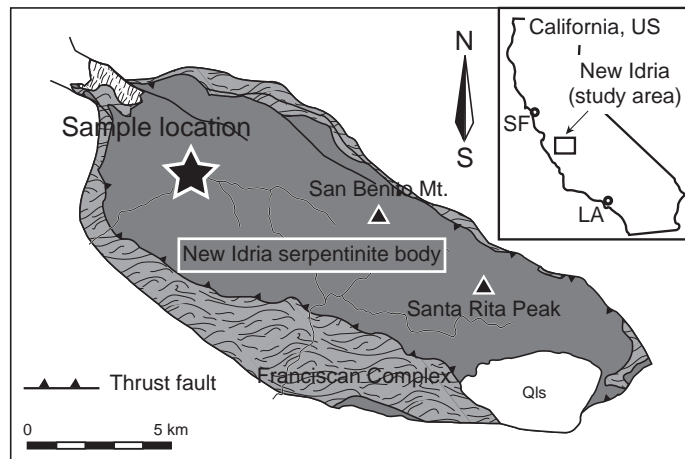


Fig. 2.1. Simplified geologic map and the sample location, expressed by the symbol 'star'. See Tsujimori et al. (2007) for larger-scaled map. Qls- Holocene-Pleistocene alluvium.

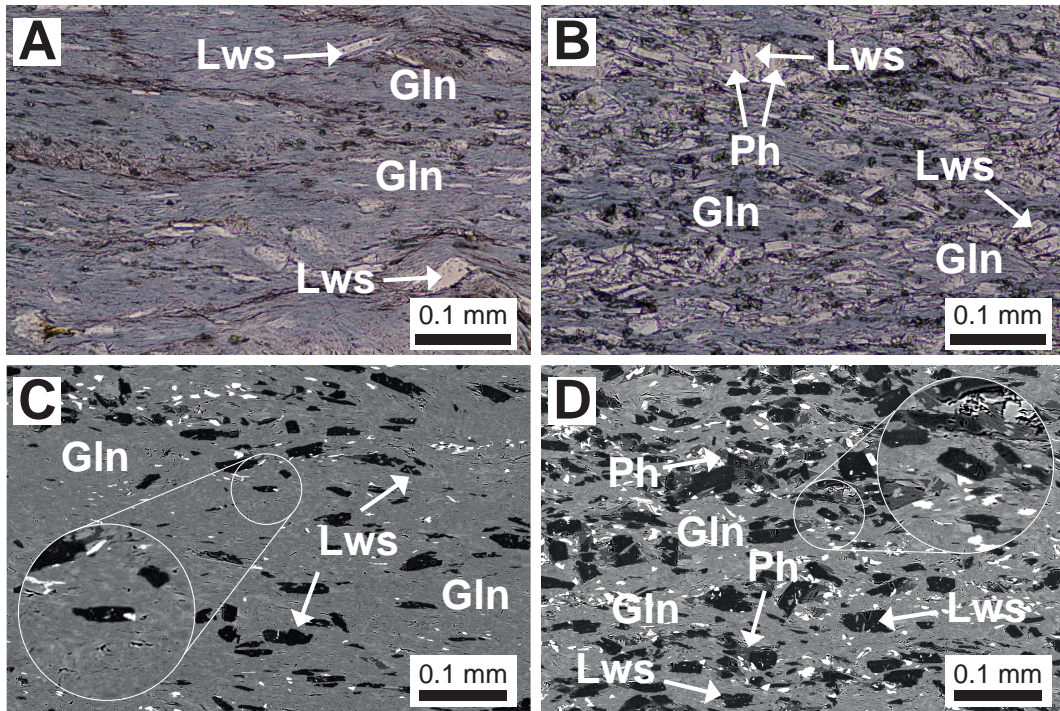


Fig. 2.2. Photomicrographs and BSE images of two representative domains. A and C show glaucophane-rich layer defined by abundant glaucophane (89%), lawsonite (8%) and rare phengite, while B and D display lawsonite-rich layer characterized by high concentrations of lawsonite (21%) partly wrapped by secondary phengite (dark grey in BSEI). Enlarged figures show euhedral grain shape or straight grain boundaries of lawsonite. Mineral abbreviations are followed to Whitney and Evans (2010).

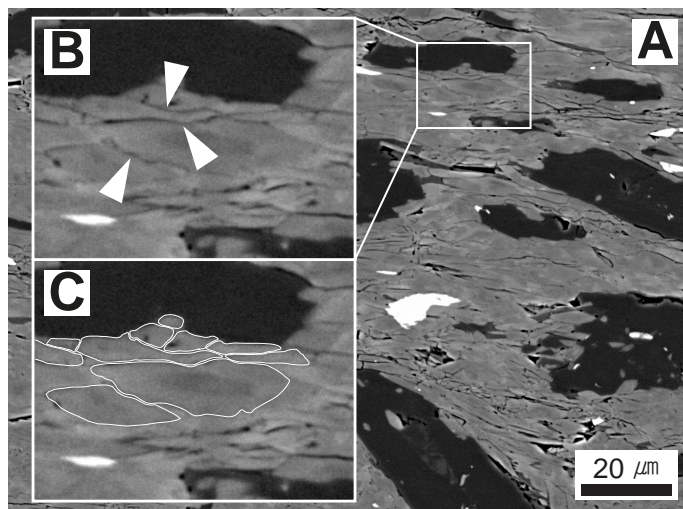


Fig. 2.3. Microstructures of glaucophane. B shows large scale image of white rectangle in A. Sharp apexes of triangles indicate curved or irregular grain boundary of glaucophane. C displays an example for the image analyses.

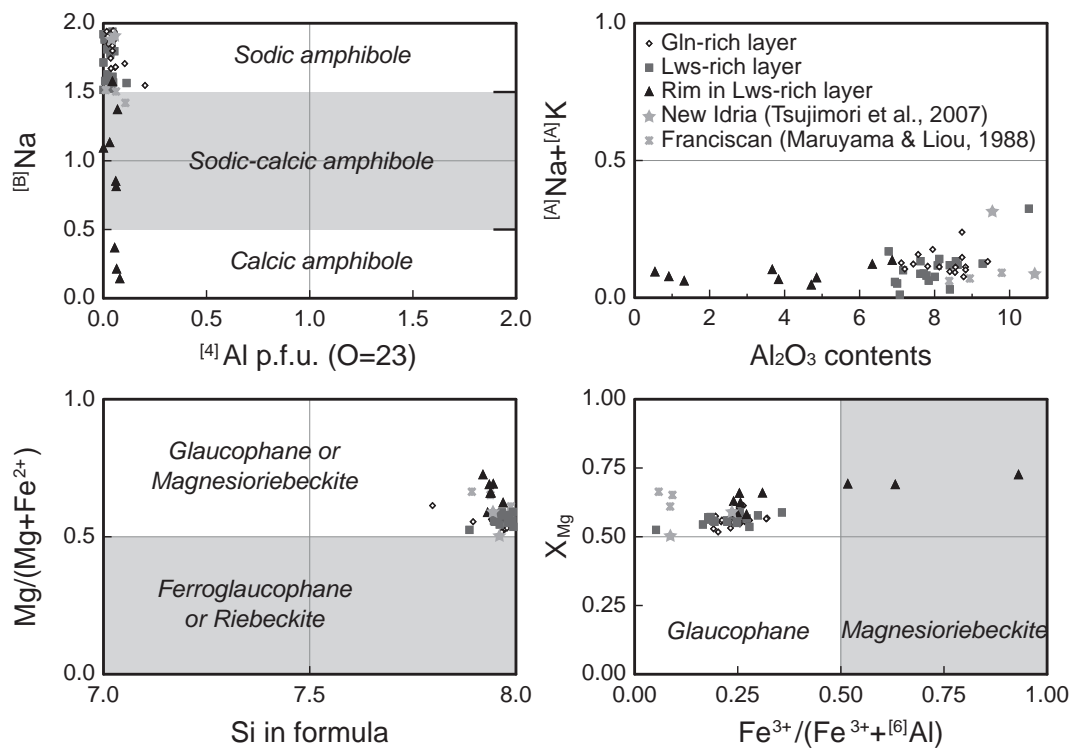


Fig. 2.4. Chemical compositions of amphibole. The contents of ferric iron in amphibole were calculated by the average of maximum and minimum estimates based on total cations as 15 for T-, C- and B-sites and 13 for T- and C-sites. Major elements of amphiboles in New Idria (Tsujimori et al., 2007) and those in Franciscan complex (Maruyama & Liou, 1988) were also marked for comparisons.

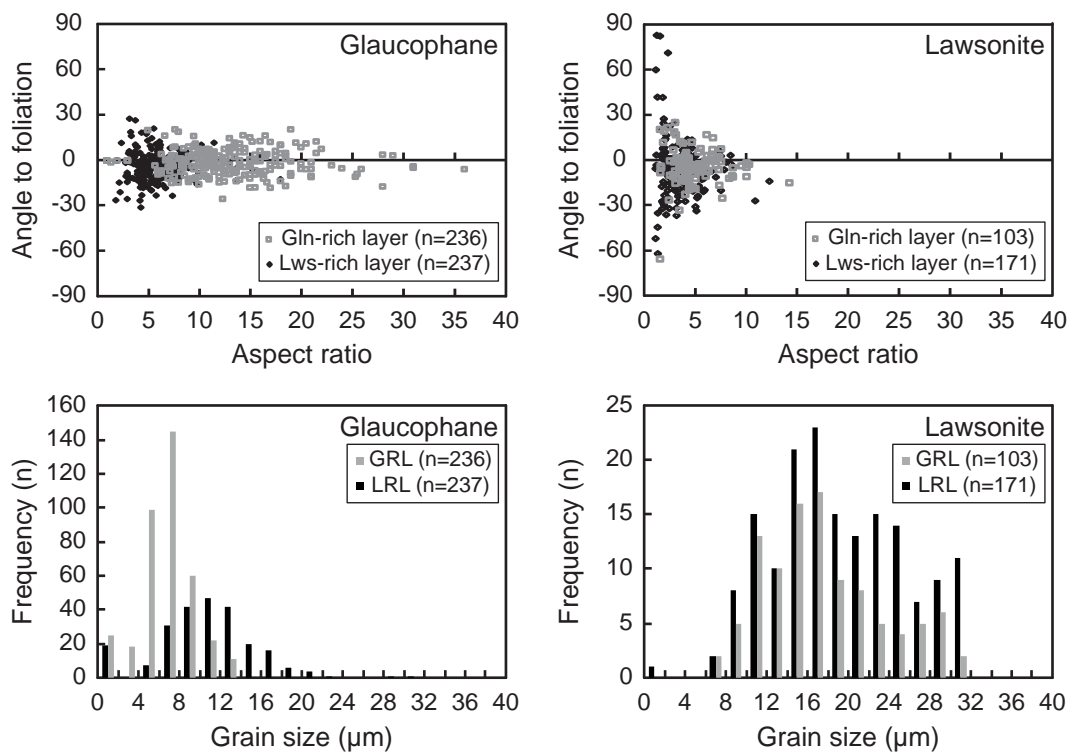


Fig. 2.5. Diagrams for angle to foliation and aspect ratio, and frequency and grain size calculated by image-analysis software ImageJ 1.44 (<http://rsb.info.nih.gov/ij/>). Best-fit ellipses were employing for diminishing the complexity of diverse shapes.

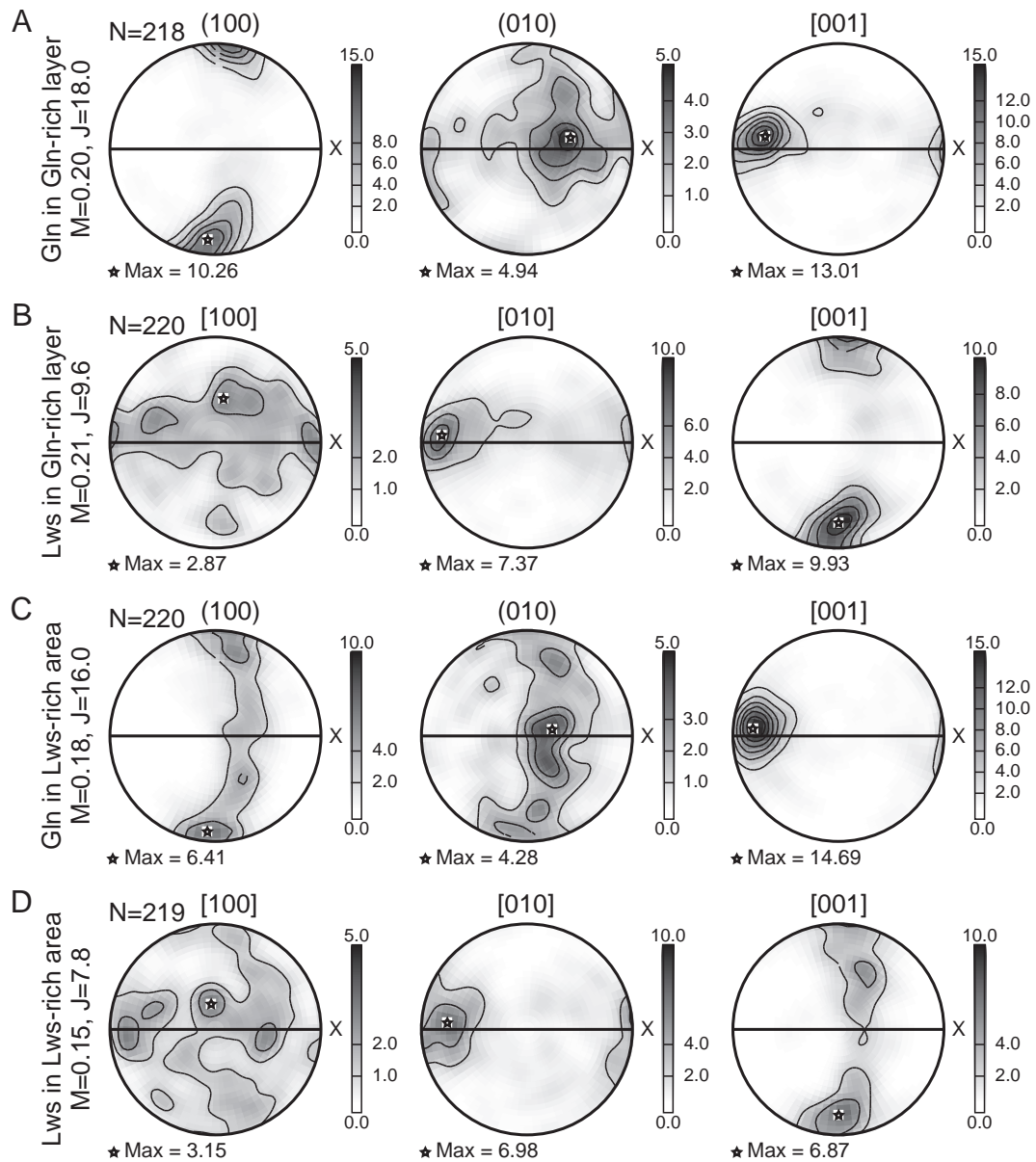


Fig. 2.6. Pole figures of glaucophane and lawsonite in glaucophane-rich (A and B) and lawsonite-rich layers (C and D). Poles were plotted employing equal-area projection in lower hemisphere. Density of poles was expressed as contours by the multiples of uniform distribution (m.u.d.). The bold line in the middle of poles and X-axis presents the directions of foliation and lineation, respectively.

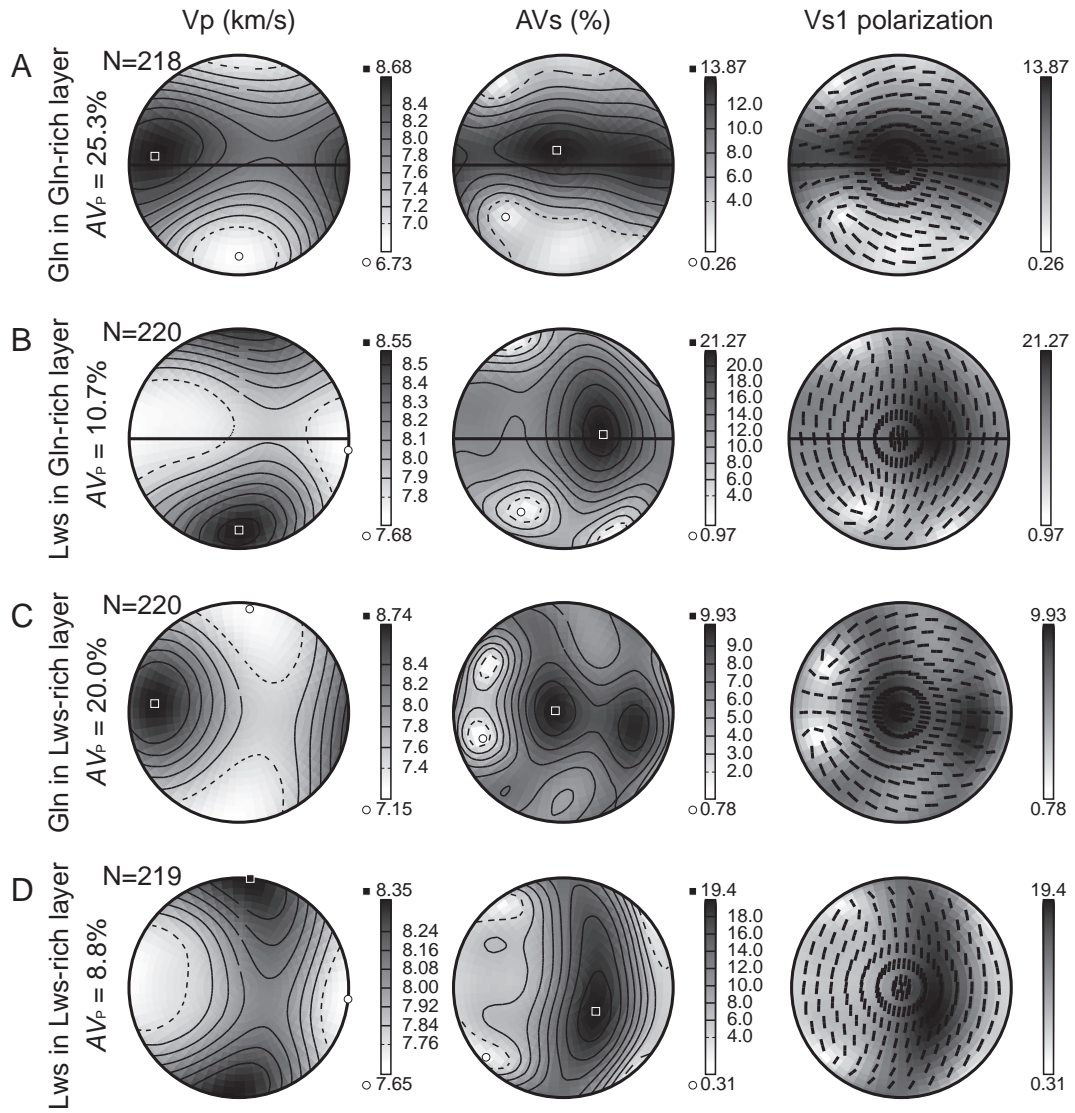


Fig. 2.7. Computed seismic anisotropy of glaucophane (A, C) and lawsonite (B, D) in the glaucophane-rich and lawsonite-rich layers, respectively. Equal area projection and the Voigt–Reuss–Hill averaging scheme were employed in lower hemisphere.

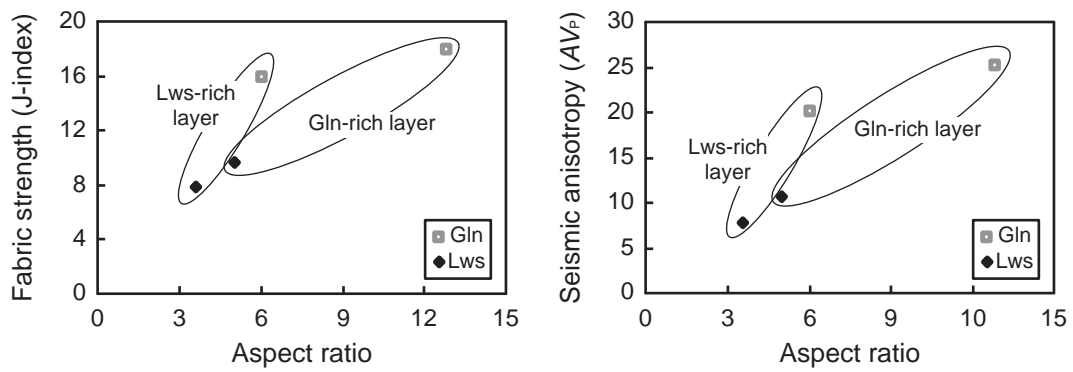


Fig. 2.8. Comparisons of fabric strength, seismic anisotropy and aspect ratio. Calculations of fabric strength (J-index) were followed to Mainprice and Silver (1993) and P-wave seismic anisotropy was computed using the software ANISctf made by D. Mainprice.

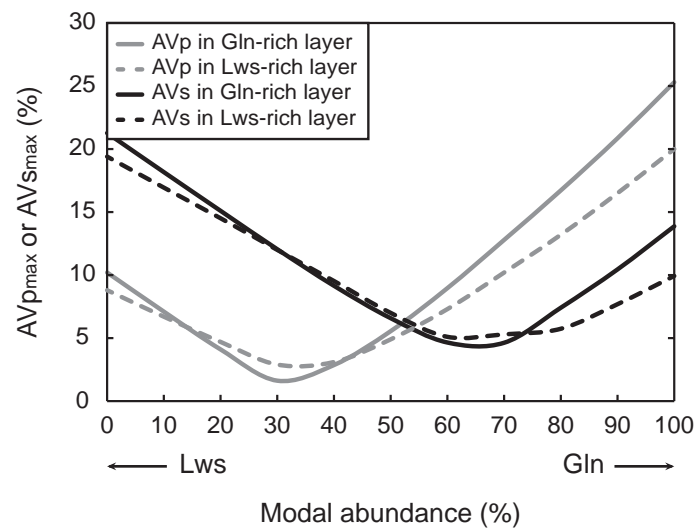


Fig. 2.9. A graph for P- and S-wave seismic anisotropy according to modal abundance. The calculations of seismic properties were conducted with every 10% step.

Table 1. Representative chemical compositions of minerals in each domain

Area	Gln-rich layer						Lws-rich layer						
	Gln		Lws		Ph		Gln			Lws		Ph	
Spot no.	14	16	1	5	6	4	33	40	48c ^a	49r ^b	79	80	17
SiO ₂	56.05	56.05	56.13	38.36	37.67	52.45	55.86	56.77	56.09	56.00	37.92	37.66	52.86
TiO ₂	0.00	0.03	0.03	0.03	0.13	0.03	0.08	0.08	0.06	0.05	0.09	0.19	0.06
Al ₂ O ₃	8.12	7.21	8.54	31.55	30.95	24.19	8.01	8.40	9.28	6.87	30.90	31.12	23.11
Cr ₂ O ₃	0.00	0.06	0.03	0.00	0.07	0.10	0.00	0.04	0.05	0.08	0.02	0.05	0.08
FeO	16.12	16.21	15.94	1.48	0.97	3.79	14.81	15.20	14.71	15.54	1.31	0.96	3.27
MnO	0.09	0.16	0.12	0.00	0.02	0.06	0.08	0.09	0.06	0.25	0.01	0.00	0.02
MgO	8.33	8.84	7.87	0.01	0.05	4.22	8.79	8.66	8.14	9.32	0.04	0.02	4.73
CaO	1.06	2.16	0.62	17.33	17.08	0.03	0.65	0.74	0.56	2.80	16.78	17.09	0.03
Na ₂ O	7.09	6.46	7.25	0.00	0.01	0.15	7.10	7.37	7.42	6.15	0.02	0.00	0.07
K ₂ O	0.00	0.00	0.02	0.01	0.01	10.76	0.00	0.02	0.02	0.10	0.02	0.02	10.80
P ₂ O ₅	0.00	0.00	0.00	0.00	0.00	0.00	0.00	0.00	0.00	0.00	0.00	0.00	0.00
Total	96.86	97.16	97.53	88.77	86.96	95.79	95.36	97.37	96.38	97.14	87.12	87.09	95.04
O.N.	23.00	23.00	23.00	8.00	8.00	11.00	23.00	23.00	23.00	23.00	8.00	8.00	11.00
Si	7.96	7.96	7.98	2.01	2.02	3.51	7.99	7.97	7.95	7.96	2.02	2.01	3.56
Ti	0.00	0.00	0.00	0.00	0.01	0.00	0.01	0.01	0.01	0.01	0.00	0.01	0.00
Al	1.36	1.21	1.43	1.95	1.95	1.91	1.35	1.39	1.55	1.15	1.94	1.96	1.83
Cr	0.00	0.01	0.00	0.00	0.00	0.01	0.00	0.00	0.01	0.01	0.00	0.00	0.10
Fe ³⁺ ^c	0.45	0.43	0.43	0.07	0.04		0.46	0.46	0.36	0.41	0.06	0.04	
Fe ²⁺	1.91	1.93	1.90			0.21	1.77	1.78	1.74	1.85			0.18
Mn	0.01	0.02	0.01	0.00	0.00	0.00	0.01	0.01	0.01	0.03	0.00	0.00	0.00
Mg	1.76	1.87	1.67	0.00	0.00	0.42	1.88	1.81	1.72	1.97	0.00	0.00	0.47
Ca	0.16	0.33	0.09	0.97	0.98	0.00	0.10	0.11	0.08	0.43	0.96	0.98	0.00
Na	1.95	1.78	2.00	0.00	0.00	0.02	1.97	2.01	2.04	1.69	0.00	0.00	0.01
K	0.00	0.00	0.00	0.00	0.00	0.92	0.00	0.00	0.00	0.02	0.00	0.00	0.93
P	0.00	0.00	0.00	0.00	0.00	0.00	0.00	0.00	0.00	0.00	0.00	0.00	0.00
Total	15.11	15.10	15.09	5.01	5.00	7.00	15.08	15.10	15.11	15.11	5.00	5.00	6.99
gln	0.73	0.65	0.77				0.74	0.75	0.82	0.62			
mrh	0.25	0.24	0.23				0.25	0.25	0.20	0.23			
act	0.31	0.64	0.19				0.20	0.22	0.17	0.83			
ts	0.00	0.00	0.00				0.00	0.00	0.00	0.00			

^a Including chemical compositions of core

^b Denoting chemical compositions of rim

^c Employing the average of maximum and minimum ferric iron in glaucophane (Leake et al., 1997)

Table 2. Comparisons of two main domains

Domain	Modal abundance ^a	Active slip-system		Fabric strength		Seismic anisotropy	
		Gln	Lws	Gln	Lws	AV_P	AV_S
Gln-rich layer	Gln89 Lws8	[001](100)	[010](001)	M=0.20, J=18.0	M=0.21, J=9.6	21.5%	10.8%
Lws-rich domain	Gln64 Lws21	[001](100)	[010](001)	M=0.18, J=16.0	M=0.15, J=7.8	11.7%	5.4%

^a Excluding phengite, sphene and apatite (abundances of each mineral are less than 2%)

Chapter III

DEFORMATION FABRICS OF NATURAL BLUESCHISTS AND IMPLICATIONS FOR SEISMIC ANISOTROPY IN SUBDUCTING OCEANIC CRUST

Main contents of this chapter have been published in *Physics of the Earth and Planetary Interiors* (2013, vol 222, 8–21)

Abstract

Investigations of microstructures are important to understand the seismic anisotropy of subducting oceanic crust hence systematic fabric analyses of glaucophane, lawsonite, and epidote in naturally deformed blueschists from the Diablo Range and Franciscan Complex in California, and the Hida Mountains in Japan are reported. Glaucophanes in the analyzed samples comprise very fine grains that are well aligned along the foliation and have high aspect ratios and strong crystal preferred orientations (CPOs) characterized by a (100)[001] pattern. These characteristics with a bimodal grain size distribution from some specimens probably signify the occurrence of dynamic recrystallization for glaucophane. Though lawsonite and epidote exhibit high aspect ratios and a strong CPO of (001)[010], straight grain boundaries and euhedral crystal shape indicates that rigid body rotation was the dominant deformation mechanism. The P-wave (AV_P) and S-wave (AV_S) seismic anisotropies of glaucophane ($AV_P = 20.4\%$, $AV_S = 11.5\%$) and epidote ($AV_P = 9.0\%$, $AV_S = 8.0\%$) are typical of the crust; consequently, the fastest propagation of P-waves is parallel to the [001] maxima, and the polarization of S-waves parallel to the

foliation can form a trench-parallel seismic anisotropy owing to the slowest V_S polarization being normal to the subducting slab. The seismic anisotropy of lawsonite ($AV_P = 9.6\%$, $AV_S = 19.9\%$) is characterized by the fast propagation of P-waves subnormal to the lawsonite [001] maxima and polarization of S-waves perpendicular to the foliation and lineation, which can generate a trench-normal anisotropy. The AV_S of lawsonite blueschist (5.6%–9.2%) is weak compared with that of epidote blueschist (8.4%–11.1%). Calculations of the thickness of the anisotropic layer indicate that glaucophane and lawsonite contribute to the trench-parallel and trench-normal seismic anisotropy beneath NE Japan, but not enough to produce that beneath the Ryukyu arc. My results demonstrate, therefore, that lawsonite has a strong influence on seismic velocities in the oceanic crust, and that lawsonite might be the cause of complex anisotropic patterns in subduction zones.

3.1. Introduction

The propagation of seismic waves is a powerful tool for understanding the rheological behavior of the Earth at depth. In subduction zones, seismic properties can provide information about the origin of the slab, the nature of the mantle wedge, slab rollback, and help us to understand back-arc spreading and to detect the presence of melts (e.g., Wiens et al., 2008). In particular, trench-parallel and trench-perpendicular shear-waves are observed in subduction zones from the polarization directions of fast propagations and the delay time between the arrivals of fast and slow shear-waves. These shear waves have been explained by theories that involve the flow of the mantle (Long and Silver, 2008) or the crystal preferred orientations (CPOs) of minerals such as olivine (Jung and Karato, 2001) and serpentine (Katayama et al., 2009). The precise source of the seismic anisotropy in subduction zones, however, is

not well defined by the shear-wave splitting method, and further studies of the mantle wedge and the subducting slab are therefore essential. In addition, recent studies have emphasized the importance of minerals such as glaucophane and lawsonite in blueschists for explaining the low velocity layer (LVL) (Chantel et al., 2012; Mookherjee and Bezacier, 2012).

The decrease of seismicity in the upper seismic zone of subducting oceanic crust might be related to a change in rock type from blueschist to eclogite (Kita et al., 2006), signifying the importance of rock-forming minerals in explaining the seismic properties. Glaucophane, lawsonite, and epidote are characterized by high water contents (~2.0–2.5 wt% for glaucophane, 1.0–11.5 wt% for lawsonite, and 1.95 wt% for epidote) and strong P-wave (AV_P) and S-wave (AV_S) seismic anisotropies in single crystals ($AV_P = 38.1\%$ and $AV_S = 27.3\%$ for glaucophane, $AV_P = 74\%$ for lawsonite, and $AV_S = 21\%$ for epidote; Schmidt and Poli, 1998; Sinogeikin et al., 2000; Mao et al., 2007; Bezacier et al., 2010). In addition, previous studies have noted variations in seismic anisotropy, possibly caused by glaucophane CPOs in combination with a diverse range of lawsonite and epidote CPOs (Bezacier et al., 2010; Fujimoto et al., 2010; Teyssier et al., 2010).

In this paper I record the results of fabric analyses of several lawsonite and epidote blueschists from the New Idria serpentinite body of the Diablo Range and Ward Creek, Cazadero, California, USA, and the Omi serpentinite mélange of the Hida Mountains in Japan. I have assessed the deformational behavior of glaucophane, lawsonite, epidote, and the blueschists on the basis of microstructures, aspect ratios, and CPOs relative to foliation, and their seismic properties have been calculated. Additionally, I discuss the tectonic implications of these three minerals with respect to seismic velocities and anisotropic patterns in a subduction zone.

3.2. Sample localities

3.2.1. The New Idria serpentinite body, Diablo Range, California

Located between the San Andreas Fault on the west and the San Joaquin Valley on the east, the New Idria serpentinite body in the Diablo Range is exposed along the crest of the Coalinga anticline, and is enclosed by high-angle normal faults that denote the exhumed trace of the Coast Range Fault (Coleman, 1980). The New Idria serpentinite is primarily chrysotile–lizardite, with minor antigorite serpentinite, and it represents the retrogression of a moderately depleted harzburgite that contained numerous tectonic blocks of greenstone and low-grade blueschists (Coleman, 1980; Tsujimori et al., 2007). A sample of highly deformed lawsonite blueschist (sample NI-01) was collected at a nearby eclogite locality where retrograde eclogite and garnet amphibolite, originating from mantle depths, are exposed along Clear Creek (Table 3.1) (Tsujimori et al., 2007; Kim et al., 2013b). The data in this paper on the rheological contrasts of glaucophane and lawsonite have already been reported (Kim et al., 2013b). I found it necessary to use these same data in this paper for my calculations of seismic anisotropies of the subducting oceanic crust, because such highly foliated lawsonite blueschists occur very rarely.

3.2.2. The Ward Creek schist, Franciscan Complex, California

The Ward Creek schist, represented by metamorphosed oceanic basalts and overlying pelagic sediments, occurs within the Franciscan Complex in the central belt of the northern Coast Ranges of California, and lies within type-III blueschists (Coleman and Lee, 1963; Maruyama and Liou, 1987, 1988). The type-III rocks are characterized by a well-developed schistosity, a fine grain size, and a banded structure

with layers composed mainly of metamorphosed basalts, cherts, shales, ironstones, and carbonates. I selected and collected a highly foliated garnet-bearing blueschist (CZ-02) close to the lawsonite eclogite locality (Table 3.1) (Tsujimori et al., 2006).

3.2.3. The Omi serpentinite mélangé, Hida Mountains, Japan

The Renge schist, an older geotectonic unit in the Sangun metamorphic belt, considered to be one of the higher-pressure schists in Japan, mainly comprises metasediments such as pelitic, psammitic and siliceous schists, and metabasites with minor metagabbro. The glaucophane schist in the Omi area, located at the northern end of the Hida Mountains, occurs in the southern chlorite zone of the Renge schist (Banno, 1958; Tsujimori et al., 2000). The glaucophane-bearing metabasites are locally intercalated with micaceous schist in a fault-bounded eclogitic unit that corresponds to the southern chlorite zone. The analyzed samples (Omi-02 and 03) were collected in areas of garnet glaucophane schist and epidote glaucophane schist (Table 3.1).

3.3. Analytical techniques

The chemical compositions of the amphiboles were determined by electron probe microanalysis (EPMA, JEOL JXA-8200) at Hiroshima University, Japan. The analytical conditions were as follows: accelerating voltage of 15 kV, beam current of 10 nA, and spot size of 3–5 μm with $K\alpha$ lines for Si, Ti, Al, Cr, Fe, Mn, Mg, Ca, Na, and K. The Fe^{3+} contents in the amphiboles were calculated as the average of the maximum and minimum estimates based on a total of 13 cations for T and C sites and 15 cations for T, C, and B sites (Leake et al., 1997).

Image analyses in sections parallel to the lineation and normal to the foliation were made in order to quantify the aspect ratios of mineral grains, and to determine the angles between the longest axes of various grains and the foliation. After tracing grain boundaries, best-fit ellipses (calculated using ImageJ 1.44) were adopted to reduce the complexity of the various shapes of grains (e.g., Mezger, 2010; Kim et al., 2013b). Grain sizes were calculated as the area of a square with the same internal area as the calculated best-fit ellipse.

Crystallographic preferred orientations of glaucophane, lawsonite, and epidote were measured by indexation of electron backscattered diffraction (EBSD) patterns (Randle, 1992; Prior et al., 1999; Randle and Engler, 2000) using an Oxford–HKL–EBSD on a Hitachi S-3400 scanning electron microscope (SEM) at Shizuoka University, Japan. The CPO measurements were conducted with an accelerating voltage of 20 kV, a working distance of 28 mm, and a beam current of ca. 10 nA. Automatic mapping of each sample (1 μm step size) was performed to examine the chemical zoning in glaucophane, lawsonite, and epidote. After I confirmed that an identical lattice orientation accompanied the chemical variations, the EBSD patterns were manually indexed by considering single individual points for each grain. The number of analysis points was standardized at 240 ± 22 to ensure the reliability of data and to allow for comparison among samples. Pole figures were plotted using the software PFch5 written by D. Mainprice, and the fabric strength was determined by the *J*-index (Bunge, 1982; Mainprice and Silver, 1993).

The seismic properties of glaucophane, lawsonite, epidote, and whole rocks made up of those minerals were calculated in order to understand their influence on the seismic properties of the subducting oceanic crust. The P-wave seismic anisotropy (AV_P) is normally described as the difference between the maximum and minimum

velocities in two dissimilar propagating paths, and expressed as a percentage. For example, the $AV_{P_{\max}}$ can be estimated by using the formula $200(V_{P_{\max}} - V_{P_{\min}})/(V_{P_{\max}} + V_{P_{\min}})$. The S-wave seismic anisotropy (AV_S) is defined as the difference between two dissimilar velocities of two orthogonally polarized S-waves individually propagating through an anisotropic medium. Hence, the percentage $AV_{S_{\max}}$ is evaluated using the formula $200(V_{S1} - V_{S2})/(V_{S1} + V_{S2})$, in which V_{S1} and V_{S2} are the fast and slow velocities, respectively. In this study, the calculations of whole rock seismic properties were made with reference to the modal abundances of each mineral (Table 3.1) (Mainprice, 1990; Mainprice et al., 2000). I employed the respective single crystal elastic constants (C_{ij}) of glaucophane (Bezacier et al., 2010), lawsonite (Sinogeikin et al., 2000), and epidote (Aleksandrov et al., 1974), and their densities with the Voigt–Reuss–Hill averaging scheme.

3.4. Description of microstructures and chemical compositions of amphibole

The sample from the New Idria serpentinite body is a fine-grained blueschist mostly composed of glaucophane, lawsonite, titanite, and phengite. It contains two distinct layers: (i) glaucophane-rich layers (GRL NI-01) and (ii) lawsonite-rich layers (LRL NI-01) (Figs. 3.1a, b, 3.2a, b; Table 3.1). Very fine-grained GRL NI-01 shows highly foliated microstructures with low contents of phengite. Anhedronal glaucophane has grain size ranging from ~1 to ~15 μm , irregular grain boundaries, and undulose extinction. Lawsonite is subhedral or euhedral and displays small grain size between ~10 and ~30 μm . Relatively fine-grained LRL NI-01 is characterized by relatively large grains of lawsonite with significant amounts of phengite around them (Figs. 3.1b and 3.2b). Interstitial glaucophane is relatively fine-grained (~5 to ~20 μm) and anhedronal to subhedral. Porphyroclastic lawsonite has angular and straight grain

boundaries, euhedral grain shape, and grain size ranging from ~10 to ~30 μm , and weakens the overall shape preferred orientation (Fig. 3.2).

The highly foliated Ward Creek lawsonite blueschist (CZ-02) is characterized by prograde-zoned garnet and relatively large grains (~30 to ~100 μm) of subhedral glaucophane (Figs. 3.1c and 3.2c). Fine-grained (~10 μm) garnet grains are mostly euhedral or subhedral and sometimes have a reaction texture with clinopyroxene and white mica. Although the sections used in this study contain only small amounts of lawsonite (<2%), the mineral assemblage garnet + lawsonite nevertheless represents the peak metamorphic conditions.

The Omi epidote blueschists (Omi-02 and 03) have a relatively weak foliation and lineation (Figs. 3.1d, e, and f). The garnet-bearing epidote blueschist (Omi-02) predominantly comprises glaucophane and epidote. Large grained (>1 mm) garnet is usually broken and the area between grains is filled by clinopyroxene. Fine-grained glaucophane (~5 to ~10 μm) and epidote (~5 to ~10 μm) generally have smooth grain boundaries, which might have been affected by grain boundary area reduction during the main deformation event (Fig. 3.2d). Most glaucophanes have a weak chemical zoning. The specimen Omi-03 from the area of epidote glaucophane schist (Tsujimori, 2002) can be divided into glaucophane-rich (GRL Omi-03) and epidote-rich (ERL Omi-03) layers (Figs. 3.1e and f) by a similar criterion with the NI-01. The GRL Omi-03 is a very fine-grained blueschist. Highly foliated glaucophane has irregular grain boundaries, undulose extinction, and very fine grains (< ~10 μm), and epidote displays anhedral to subhedral grain shape with size ranging from ~5 to ~20 μm . The ERL Omi-03 is characterized by relatively large and euhedral epidote (~10 to ~30 μm) with interstitial glaucophane (~5 to ~20 μm). Sometimes chemical zoning can be observed for glaucophane.

Glaucophane, a sodic amphibole, is defined by $(\text{Na} + \text{K})_{\text{A}} < 0.50$, $\text{Mg}/(\text{Mg} + \text{Fe}^{2+}) \geq 0.5$, and ${}^6\text{Al} \geq \text{Fe}^{3+}$ (Leake et al., 1997). Therefore, most of the spots I analyzed can be defined as glaucophane (Fig. 3.3; Table 3.2). A few spots located in the cores or rims of glaucophane plot instead as magnesioriebeckite, winchite, or actinolite (Fig. 3.3). My analyzed glaucophanes are characterized by a decrease in Al from core to rim (Table 3.2), suggesting they formed during retrogression (Maruyama et al., 1986). The mineral assemblages (and making due reference to previous studies of similar assemblages) indicate peak metamorphic conditions of $P > 1.0$ GPa and $T = 200\text{--}290$ °C for the New Idria lawsonite blueschists, $P \sim 1.8\text{--}2.2$ GPa and $T = 430\text{--}440$ °C for the Ward Creek lawsonite blueschists, and ~ 1 GPa and $400\text{--}460$ °C for the Omi epidote blueschists (Maruyama and Liou, 1988; Tsujimori, 2002; Tsujimori et al., 2006, 2007). Although an increase in Al from core to rim could be observed in GRL Omi-03 (Table 3.2), the glaucophane in the matrix would normally have formed by the retrograde metamorphism of eclogite and by the alteration of jadeite (Deer et al., 1992). In addition, Tsujimori (2002) reported that retrograde blueschist-facies overprinting is in garnet-free P-T range. I have therefore adopted the metamorphic conditions noted above for this study.

3.5. Results

3.5.1. Microscopic analyses

Most of the glaucophane has a high aspect ratio (3.0–12.8) with long axes at low angles to the foliation (Fig. 3.4; Table 3.1). In the New Idria blueschists, lawsonite has a relatively low aspect ratio (3.6–5.0) with long axes at higher angles to the foliation than glaucophane (Figs. 3.4a, b; Table 3.1). Epidote is characterized by

grains of relatively low aspect ratio (2.1–3.4), with long axes at high angles to the foliation (Figs. 3.4d–f; Table 3.1).

Figure 3.5 shows the grain size distributions in the analyzed samples. To deal with uncertainties and trivial peaks, I assume that points higher than a frequency of 5 are valid. Glaucofanite typically displays a very fine grain size (1–59 μm), with two peaks in the grain size distributions for the New Idria blueschists, and a single peak for the Ward Creek and Omi blueschists (Fig. 3.5; Table 3.1). The lawsonite is characterized by slightly larger grains (15–20 μm) and a broader range of grain size (10–30 μm) with a single peak (Fig. 3.5; Table 3.1). Epidote usually has a fine grain size (10–20 μm) with a single peak, except in the Omi-03 (Fig. 3.5; Table 3.1). The Omi-03 contains two certain peaks of grain size distributions of epidote. The grain size distribution data shows, therefore, that a single peak in the distributions is common, that two peaks could be observed for glaucophane in the New Idria blueschists and epidote in the Omi blueschists, and that glaucophane has the smallest grain size.

3.5.2. EBSD patterns

Glaucofanite, lawsonite, and epidote each have distinctive CPOs. Pole figures of glaucophane in the analyzed samples have (100) subparallel to the foliation and [001] subparallel to the lineation (Fig. 3.6), with the *J*-index intensity ranging from 9.0 (Omi-02) to 32.5 (GRL Omi-03) (Table 3.1). Lawsonite in the New Idria blueschist (NI-01) has [010] subparallel to the lineation, foliation-subnormal [001] axes, and scattered [100] (Fig. 3.7). The *J*-index intensity for lawsonite in the New Idria blueschist (NI-01) is 7.8 in the GRL and 9.6 in the LRL (Table 3.1). Epidote has (010) subnormal to the foliation and lineation, [001] subnormal to the foliation, and

(100) has a scattered distribution (Fig. 3.8). The value of the J -index intensity ranges from 7.2 (Omi-02) to 12.5 (GRL Omi-03) (Table 3.1). The (100) poles of glaucophane in the epidote blueschist (Omi-03) particularly have a higher pdf than [100] axes parallel to the lineation, suggesting the stronger development of a foliation rather than a lineation (Fig. 3.6). The J -indices of poles figures can be compared with the grain sizes of glaucophane, lawsonite, and epidote in Table 3.1 and the plots of Figs. 3.6–3.8.

3.5.3. Seismic anisotropy

The V_P , V_{S1} , V_{S2} , AV_S , and V_{S1} polarizations of average glaucophane, lawsonite, epidote, and whole rocks for the New Idria lawsonite blueschist (NI-01) and Omi epidote blueschist (Omi-03) are projected onto the lower hemisphere in Figs. 3.9 and 3.10. Since the number of analysis points for each sample is similar (240 ± 22), the average seismic properties can be calculated from the sum of data for each sample. The seismic properties of average glaucophane are estimated to be 6.87–8.42 km/s for V_P , 4.39–4.86 km/s for V_{S1} , and 4.32–4.54 km/s for V_{S2} , with a seismic anisotropy of 20.4% for AV_P and 11.48% for AV_S (Fig. 3.9a). The patterns for average glaucophane show V_{Pmax} along the lineation, AV_{Smax} and V_{S1max} polarization subparallel to the foliation, and with the directions of V_{Pmin} , AV_{Smin} , and V_{S1min} polarization normal to the foliation. The V_P value of average lawsonite is calculated to be 7.66–8.44 km/s, V_{S1} is 4.02–4.55 km/s, and V_{S2} is 3.69–4.24 km/s, with a strong seismic anisotropy ($AV_P = 10.7\%$, $AV_S = 12.3\%$) (Fig. 3.9b). The V_{Pmax} of average lawsonite is developed perpendicular to the foliation, as are the [001] axes, the AV_{Smax} and V_{S1max} polarizations are vertical, V_{Pmin} is formed subparallel to the lineation, and the AV_{Smin} and V_{S1min} polarizations are subnormal to the foliation. The evaluated V_P , V_{S1} , and V_{S2}

of average epidote are 7.09–7.75, 4.16–4.44, and 4.09–4.31 km/s, respectively (Fig. 3.9c). The seismic anisotropy of average epidote is relatively weak ($AV_P = 9.0\%$, $AV_S = 8.04\%$) compared with the other minerals. The patterns of seismic properties are similar to those of glaucophane, so that the $V_{P_{\max}}$ and $AV_{S_{\max}}$ of epidote are parallel to the lineation and foliation, respectively, and $V_{P_{\min}}$ and $AV_{S_{\min}}$ are developed normal to the foliation.

The seismic properties of whole rocks are evaluated with the assumption that the lawsonite and epidote blueschists only contain glaucophane, lawsonite, and epidote. The New Idria lawsonite blueschist (NI-01) calculated on the basis of the averages for glaucophane and lawsonite has values of 6.99–8.31 km/s for V_P , 4.36–4.74 km/s for V_{S1} , and 4.27–4.51 km/s for V_{S2} , with AV_P being 12.0%–17.2% and AV_S being 4.4%–8.2% (Figs. 3.10a and b). The anisotropic seismic patterns of lawsonite blueschist are similar to those of glaucophane, with $V_{P_{\max}}$ parallel to the lineation, $AV_{S_{\max}}$ and $V_{S1_{\max}}$ polarizations parallel to the foliation, and $V_{P_{\min}}$ and $AV_{S_{\min}}$ perpendicular to the foliation. The V_P of the Omi epidote blueschist (Omi-03), calculated from the average glaucophane and epidote, is 6.88–8.38 km/s, V_{S1} is 4.20–4.83 km/s, V_{S2} is 4.16–4.53 km/s, and the seismic anisotropy is stronger ($AV_P = 11.8\%$ –19.6% and $AV_S = 7.8\%$ –10.0%) than in the lawsonite blueschist (Figs. 3.10c and d). The $V_{P_{\max}}$ and $AV_{S_{\max}}$ of the epidote blueschist are parallel to the lineation and foliation, respectively, while $V_{P_{\min}}$ and $AV_{S_{\min}}$ are developed normal to the foliation.

3.6. Discussion

3.6.1. Deformational mechanisms of glaucophane, lawsonite, and epidote

Microstructures are affected by (i) progressive metamorphism where rock-forming minerals transform according to the progressively changing mineral stability

fields, and (ii) the deformation of minerals, the manner of which changes with the mineral and the various prevailing conditions. Natural amphiboles can be subject to different deformation mechanisms such as cataclastic deformation, rigid-body rotation, and dynamic recrystallization (Cumbest et al., 1989; Ildefonse et al., 1990; Nyman et al., 1992; Siegesmund et al., 1994). Glaucophane, on the other hand, tends to deform predominantly by crystal plastic mechanisms via the activation of different slip systems, together with the activation of dynamic recrystallization (Reynard et al., 1989; Zucali et al., 2002). Additionally, very fine grain sizes often develop by strain-induced recrystallization during or after crystal plastic deformation (e.g., Drury and Urai, 1990). In the present specimens, the glaucophanes display strong CPOs and a very fine grain size that is possibly the product of grain size reduction, suggesting that the microstructures formed as a result of dynamic recrystallization (e.g., Díaz Aspiroz et al., 2007). This interpretation is supported by the relationship between grain size and the J -index of pole figures, and by the presence of two peaks in the grain size distributions from some samples (Figs. 3.5, 3.6; Table 3.1). Therefore, the glaucophanes exhibit characteristic of dynamic recrystallization, possibly accommodated by dislocation creep. The Omi garnet-bearing blueschists (Omi-02) exhibit gently curved grain boundaries between glaucophane and epidote, suggesting the activation of grain boundary area reduction during recovery (Fig. 3.2d). Irregular or curved grain boundaries of glaucophane imply annealing and grain growth as a result of the reduction of interfacial free energy in a low stress regime (Fig. 3.2) (Evans et al., 2001). Although dissolution and precipitation creep are the dominant deformation mechanisms for calcic amphiboles at low temperatures, the weak chemical zoning and the very fine grain size of the analyzed glaucophanes demonstrate that these mechanisms were not important for the glaucophane.

On the other hand, the deformation mechanisms of lawsonite and epidote are poorly understood. Teyssier et al. (2010) interpreted lawsonite as a rigid phase based on the assumption that the associated glaucophane is weaker. Similarly, Kim et al. (2013b) reported lawsonite to be stronger than glaucophane according to fabric analyses of two distinct layers in the New Idria lawsonite blueschist. Lawsonite in the present specimens has relatively strong CPOs, even though euhedral grains are present with angular and straight boundaries (Figs. 3.2a and b). Therefore, the lawsonite microstructures that formed within the wide stability field of lawsonite possibly developed with the aid of rigid body rotations. Epidote in the present specimens also exhibits straight grain boundaries and euhedral shapes, implying rigid body rotation as the dominant deformation mechanism. In view of these straight grain boundaries, the two conspicuous grain-size-distribution peaks for epidote in the epidote-rich layer in Omi blueschist (ERL Omi-03) can probably be attributed to two stages of growth, during prograde and retrograde metamorphism, rather than to dynamic recrystallization (Figs. 3.2f and 3.5). My results suggest, consequently, that microstructures of the bulk rock and each mineral such as epidote and lawsonite were decided by deformation of glaucophane.

3.6.2. P–T conditions of deformation

Lawsonite and epidote eclogites generally form at depths greater than 45 km in subduction zones (Tsuji-mori et al., 2006), and they transform to other minerals and rocks during the relatively low P–T conditions of exhumation so that they are relatively rare at the surface, especially without some degree of alteration. The Diablo Range and Ward Creek in California, and the Omi area in central Japan, are unusual in that they expose unaltered lawsonite or epidote eclogites, implying rapid

exhumation, probably as a result of slab breakoff. Lawsonite in the New Idria blueschist, and epidote in the Omi epidote blueschists, possibly formed during prograde subduction-related metamorphism, rather than during uplift and exhumation, based on the euhedral grain shapes and straight grain boundaries. At a late stage of subduction the maximum pressure conditions attained for the New Idria serpentinite body were >1.3 GPa (Tsuji-mori et al., 2007), and the maximum P–T conditions attained in the Hida metamorphic belt were >1.8 GPa and 550–600 °C (Tsuji-mori, 2002).

On the other hand, most of the glaucophane analyzed here possibly formed along a retrograde *P–T* path, based on its typical occurrence in the matrix, and the decrease in Al from core (glaucophane) to rim (winchite or actinolite). Although glaucophane in the glaucophane-rich layer in the Omi blueschist (GRL Omi-03) is the exception, in that it shows an increase of Al from core to rim, it still occurs in the matrix, and it might therefore have formed during retrogression and been altered after uplift. This can be supported by garnet-free assemblages of the Omi-03, in the retrograde P-T path of a previous study (Tsuji-mori, 2002). The well-aligned fabrics displayed by glaucophane, lawsonite, and epidote, characterized by the relatively low angles between crystal long axes and the mean position of the foliation plane, indicate that deformation took place during or after the blueschist-facies overprinting (Fig. 3.4). The strong CPOs that define the foliation might be attributed to the flow of dynamically recrystallized grains, denoting the presence of synkinematic microstructures (e.g., Hippertt and Hongn, 1998). Consequently, the microstructures in the analyzed samples are thought to have formed at $P > 1$ GPa and $T = 200–290$ °C for the New Idria blueschist (Tsuji-mori et al., 2007), $P = \sim 1.8–2.2$ GPa and $T = 430–440$ °C for the Ward Creek blueschist (Tsuji-mori et al., 2006), and $P = \sim 1$ GPa and T

= 400–460 °C for the Omi blueschists (Tsujimori, 2002), consistent with the stability field of blueschist (Fig. 3.11).

3.6.3. Seismic properties of lawsonite and epidote blueschists in the subducting slab

The angle of subduction, which is influenced by the age of the crust and depositional materials during movement to the subduction zone, can affect the P–T increase during subduction; consequently, the geothermal gradient is high in SW Japan and low in NE Japan. Owing to the stability field of blueschist, lawsonite blueschist is the main constituent of the oceanic crust beneath NE Japan, while epidote blueschist is the main constituent beneath SW Japan. The V_P of lawsonite (6.99–8.31 km/s) and epidote blueschists (6.88–8.38 km/s), as modeled from the average seismic properties of their main rock-forming minerals, are higher than the values at ~30–50 km depth derived from recent seismological studies in NE Japan (7.1–7.4 km/s; Tsuji et al., 2008) and SW Japan (7.1–7.5 km/s; Shelly et al., 2006) (Fig. 3.10). The slightly faster seismic velocity in SW Japan, compared with NE Japan, is consistent, however, with my study. The average velocities of lawsonite blueschist are $V_P = 7.67$ km/s and $V_S = 4.44$ km/s (Figs. 3.10a and b), and these are similar values to the modeled result of $V_P = 7.71$ km/s and $V_S = 4.49$ km/s (Bezacier et al., 2010), as well as an experimental result of $V_P = 6.0$ –7.4 km/s (Fujimoto et al., 2010). Therefore, since the seismic properties calculated for my samples are similar to those previously observed and modeled, and to experimental data, it suggests that my results are valid for the purposes of my study.

To better understand the implications of the seismic anisotropy of bulk rock masses, the $AV_{P_{\max}}$ and $AV_{S_{\max}}$ of lawsonite and epidote blueschists have been computed using the assumption that a mass of rock is composed mainly of diverse

modal abundances of average glaucophane, lawsonite, and epidote (Fig. 3.12). The seismic anisotropy of lawsonite blueschist is evaluated as $AV_P = 3.9\%–20.4\%$ and $AV_S = 4.54\%–19.88\%$ with a ‘concave’ feature characterized by lower values in the center and higher values in both ends (Fig. 3.12). An offset of the different propagating directions of seismic waves between glaucophane and lawsonite may cause the specific ‘concave’ feature, which is distinct from the ‘straight’ (directly or inversely proportional) change of AV_P and AV_S that is attributed to the same propagating direction of seismic waves in glaucophane and epidote (Bezacier et al., 2010; Satsukawa et al., 2011). The AV_P and AV_S of epidote blueschist are calculated as $AV_P = 9.0–20.4$ km/s and $AV_S = 8.04–11.48$ km/s with ‘straight’ lines. Consequently, I note that the seismic anisotropy of a mass of rock, especially one composed of highly anisotropic phases, is controlled by the modes of the constituent rock-forming minerals and the anisotropic seismic patterns of each phase. This proposition is consistent with the stronger trench-parallel seismic anisotropy in the Ryukyu arc (epidote blueschist) and the weaker anisotropy in NE Japan (lawsonite blueschist). The fastest V_P and AV_S of glaucophane and bulk rocks are along the foliation, whereas V_{Pmin} and AV_{Smin} are developed normal to the foliation and lineation (Figs. 3.9a and 3.10). The results indicate that a weak seismic anisotropy develops subnormal to the shear direction, and also that the V_{Pmax} and AV_{Smax} of glaucophane and the bulk rock are subparallel to the movement direction. Deformation mainly occurs in response to the movement direction of the subducting plate, and the fast shear wave is therefore established subparallel to the trench (trench-parallel fast anisotropy) (Fig. 3.13). On the other hand, lineation-perpendicular propagations of the fast V_{S1} polarization of lawsonite are generated perpendicular to the movement direction of the subducting oceanic crust, and hence a trench-perpendicular anisotropy can occur (Fig. 3.13).

The strong anisotropic properties of minerals can also be useful for understanding the nature of the LVL (Nikulin et al., 2009; Bostock, 2012; Wirth and Long, 2012). Chantel et al. (2012) reported a reasonably low V_S of lawsonite with strong anisotropy due to the (010)[001] slip system, which is in contrast to other studies (Fujimoto et al., 2010; Tessier et al., 2010), including the present study. I therefore apply the results of my study to the LVL according to subducting angles, mainly using the preferred orientations and V_P/V_S ratios of minerals. A low seismic velocity can be produced when seismic waves propagate along the V_{Pmin} and V_{Smin} directions of minerals. For local events, slow seismic waves can be generated by changes in rock type, such as eclogite to blueschist, and the V_{Pmin} and V_{Smin} therefore need to be parallel to the lineation in the eclogite. This explains why the [010] axes of lawsonite are more appropriate rather than the (010) planes of epidote for local events. On the other hand, teleseismic waves can be generated normal to the surface of the crust, and this is suitable for a warm slab in which the (100) planes of glaucophane contain V_{Pmin} and V_{Smin} . The V_P/V_S ratios are calculated as 2.08 for lawsonite ($V_P = 7.66$ km/s and $V_S = 3.69$ km/s) and 1.59 for glaucophane ($V_P = 6.87$ km/s and $V_S = 4.32$ km/s). Although the V_P/V_S ratios estimated for glaucophane are rather low, the values for lawsonite are higher than those for the other minerals present. Therefore, lawsonite might contribute to the low velocity layer with high V_P/V_S ratios, whereas blueschists lacking lawsonite require other minerals such as serpentine or pore fluids along the grain-boundaries.

The thickness of an anisotropic layer is used to compare the seismic properties of glaucophane, lawsonite, and epidote with other well-known anisotropic minerals such as olivine and serpentine (e.g., Katayama, 2009). The thickness (D) of the

anisotropic layer is decided by the multiplication of velocity (v) and time (t), and hence the delay time (dt) is defined by the following equation:

$$dt = AV_S / \langle V_S \rangle D,$$

where AV_S is the anisotropy of a specific propagation direction and $\langle V_S \rangle$ indicates the average velocity of the fast and slow velocities. Figure 3.14 shows the relations between the delay time and the thickness of the seismically anisotropic layer that is composed of glaucophane, lawsonite, and epidote aggregates. The calculated results for olivine ($AV_S = 4.5\%$ and $\langle V_S \rangle = 4.75$ km/s; Katayama and Karato, 2006) and serpentine ($AV_S = 36.0\%$ and $\langle V_S \rangle = 4.13$ km/s; Katayama et al., 2009) are shown for comparison. With respect to the observed delay time (0.06–0.10 s) of trench-parallel AV_S beneath NE Japan (Nakajima and Hasegawa, 2004), the thickness of the anisotropic layer is calculated to be 2–4 km for average glaucophane, and 3–4 km for average epidote (Fig. 3.14). The estimates are thicker than the calculated thickness for serpentine (1 km), but noticeably thinner than for olivine (6–11 km). Using a 7 ± 1 km thickness for the oceanic crust (White et al., 1992), a 2–4 km anisotropic layer caused by glaucophane is capable of producing the trench-parallel fast anisotropy beneath NE Japan (cold subducting slab). On the other hand, the thickness of the anisotropic layer caused by lawsonite is calculated to be 2–5 km for trench-normal fast anisotropy, based on the observed delay times (0.10–0.26 sec) in NE Japan (Nakajima and Hasegawa, 2004). Given the delay time (~ 1 –2 s) beneath the Ryukyu arc (Long and van del Hilst, 2005), the thickness can be computed to be 39–79 km for average glaucophane and 42–83 km for average epidote (Fig. 3.14). The thickness of an anisotropic layer comprising serpentine (11–23 km) or olivine (105–211 km) is insufficient to explain the strong seismic anisotropy beneath the Ryukyu arc (hot subducting slab) only by a single mineral phase. My results suggest, therefore, that

beneath NE Japan, glaucophane may contribute to the trench-parallel seismic anisotropy in the forearc, and lawsonite to the trench-normal anisotropy in the back-arc. Beneath the Ryukyu arc, serpentine and olivine may also partly help to generate the seismic anisotropy.

Natural rocks, however, are composed of poly-phases, and the mineral assemblages need to be considered along with the subduction processes. The lawsonite blueschists contain 75%–91% of glaucophane and 9%–25% of lawsonite, and these main constituents show different seismic anisotropic patterns from each other (Figs. 3.10a, b; Table 3.1). On the other hand, the epidote blueschists consist mainly of glaucophane 26%–94% and epidote 6%–74%, and these minerals have similar anisotropic patterns (Figs. 3.10c, d; Table 3.1). The similar anisotropic patterns of epidote and glaucophane lead one to suggest that the seismic anisotropy of epidote blueschist is the same as the average values of the epidote and glaucophane seismic anisotropies (Figs. 3.9a, c, and 3.10). The differing patterns of seismic anisotropy for lawsonite and glaucophane, however, act against each other, so that a lawsonite blueschist has a lower seismic anisotropy than an epidote blueschist (Figs. 3.9a, b, and 3.12). The countervailing effect of lawsonite might be related to the weak trench-parallel seismic anisotropy in NE Japan, whereas the complementary patterns of the seismic anisotropies of epidote and glaucophane might be the cause of the strong trench-parallel seismic anisotropy in the Ryukyu arc (Fig. 3.15b). Beneath NE Japan, glaucophane, along with the countervailing effects of lawsonite, controls the seismic anisotropy of the subducting slab at ~30–110 km depth. At 110 km depth the glaucophane breaks down, and omphacite forms within the stability field of lawsonite during eclogitization. The seismic anisotropy of eclogite may be governed, therefore, by a strongly seismic anisotropic mineral such as lawsonite ($AV_P = 9.6\%$ and $AV_S =$

19.88% in my samples), because the seismic anisotropy of omphacite is low ($AV_{P_{\max}} = 1.9\%$, $AV_{S_{\max}} = 2.5\%$; Bascou et al., 2001). In addition, lawsonite has a V_{S1} polarization that is perpendicular to the foliation, and this can explain the trench-perpendicular seismic anisotropy observed beneath NE Japan (Fig. 3.15a). Other factors, such as physical variables or microstructural conditions (minor phases, grain boundaries, microcracks, and alteration), need to be considered for a complete understanding of seismic velocities, but the above results suggest that trench-parallel and trench-normal seismic anisotropy beneath NE Japan can be explained by glaucophane and lawsonite, respectively, and that the weak trench-parallel anisotropy beneath NE Japan can be attributed to the countervailing effects of lawsonite. In addition, the strong seismic anisotropy beneath the Ryukyu arc might be dominated in the subducting oceanic crust by combinations of minerals with similar seismic anisotropic patterns, such as glaucophane and epidote, and in the mantle wedge by minerals such as serpentine and olivine.

3.7. Conclusions

I presented important new data concerning (i) the seismic anisotropy of subducting oceanic crust and (ii) the microstructures and deformational behavior of rock-forming minerals in natural lawsonite blueschists from the Diablo Range and the Franciscan Complex in California, and in natural epidote blueschists from the Hida Mountains, Japan. I carefully compared the calculated seismic velocities and anisotropies of glaucophane, lawsonite, and epidote with observatory data for subduction zones. The principal results of my investigations into the microstructures and seismic properties are as follows.

(1) Glaucophane, as the main constituent of the matrix, is very fine grained, has a strong shape preferred orientations, high aspect ratios, and distinct CPOs (Figs. 3.1, 3.2, 3.4, and 3.6). All microstructures of the glaucophane suggest characteristic of dynamic recrystallization probably activated by dislocation creep. On the other hand, lawsonite and epidote both occur as porphyroclasts, and their euhedral grain shapes and straight grain boundaries (Figs. 3.1, 3.2, 3.4, 3.7, and 3.8) indicate that deformation took place primarily by rigid body rotation.

(2) The calculated average seismic velocities ($V_P = 6.87\text{--}8.42$ km/s, $V_S = 4.32\text{--}4.86$ km/s for glaucophane; $V_P = 7.66\text{--}8.44$ km/s, $V_S = 3.69\text{--}4.55$ km/s for lawsonite; $V_P = 7.09\text{--}7.75$ km/s, $V_S = 4.09\text{--}4.44$ km/s for epidote) are similar to previous observations (Shelly et al., 2006; Tsuji et al., 2008), modeling results (Bezacier et al., 2010), and experimental data (Fujimoto et al., 2010) (Fig. 3.9). For an average glaucophane and epidote, the propagations of V_P and V_S polarization develop along the lineation and foliation, respectively, while for an average lawsonite they are subnormal to the foliation and lineation, respectively. Foliation-subparallel V_S polarization in glaucophane and epidote can generate a trench-parallel seismic anisotropy owing to the development of a foliation parallel to the direction of the subduction, whereas the V_S polarization of lawsonite can establish a trench-normal seismic anisotropy (Fig. 3.13).

(3) Relatively strong seismic anisotropies were calculated for the main mineral phases in blueschists ($AV_P = 20.4\%$, $AV_S = 11.5\%$ for glaucophane; $AV_P = 9.6\%$, $AV_S = 19.9\%$ for lawsonite; $AV_P = 9.0\%$, $AV_S = 8.0\%$ for epidote) (Fig. 3.9). A thin anisotropic layer composed of glaucophane, epidote, and lawsonite is sufficient to explain the observed delay time of trench-parallel (0.06–0.10 sec) and trench-normal (0.10–0.26 sec) shear wave splitting beneath NE Japan (Nakajima and Hasegawa,

2004), but it is insufficient for the Ryukyu arc (1–2 sec; Long and van del Hilst, 2005) (Fig. 3.14). The calculations based on the relative abundance of the constituent minerals are consistent with the ‘concave’ changes of AV_P and AV_S that depend on mineral abundances, and also with the stronger trench-parallel anisotropy in the Ryukyu arc and the weaker seismic anisotropy in NE Japan (Fig. 3.12). All the data collected from natural blueschists indicate the seismic anisotropies of lawsonite and epidote, in combination with that of glaucophane, play important roles in producing the trench-parallel and trench-normal seismic anisotropies, and they also provide explanations for the low velocity layer in subduction zones.

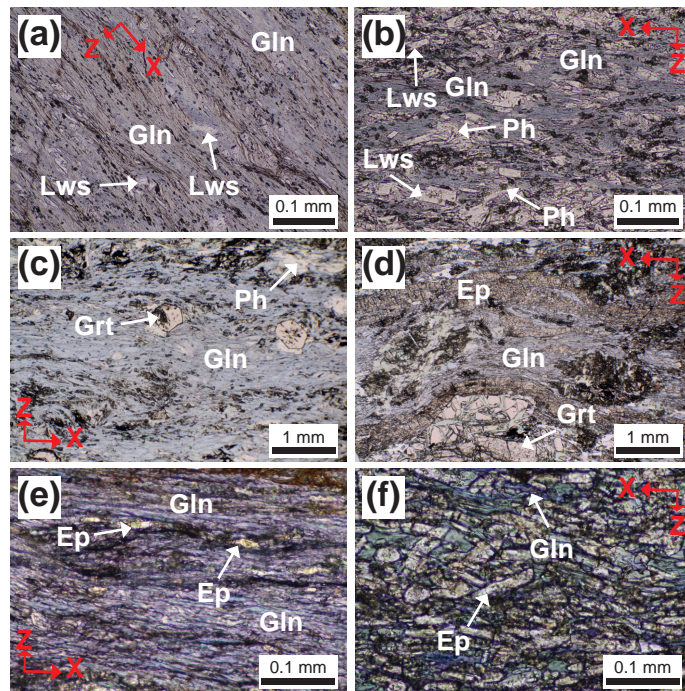


Fig. 3.1. Photomicrographs of the analyzed samples. (a) Glaucophane-rich and (b) lawsonite-rich layers in NI-01 collected from the New Idria serpentinite body, Diablo Range, California. (c) CZ-02 from Ward Creek, Franciscan Complex, California. (d) Omi-02 and (e) glaucophane-rich and (f) epidote-rich layers in Omi-03 from the Omi serpentinite mélangé, Hida Mountains, Japan. See Table 1 for sample locations. Mineral abbreviations follow those in Whitney and Evans (2010).

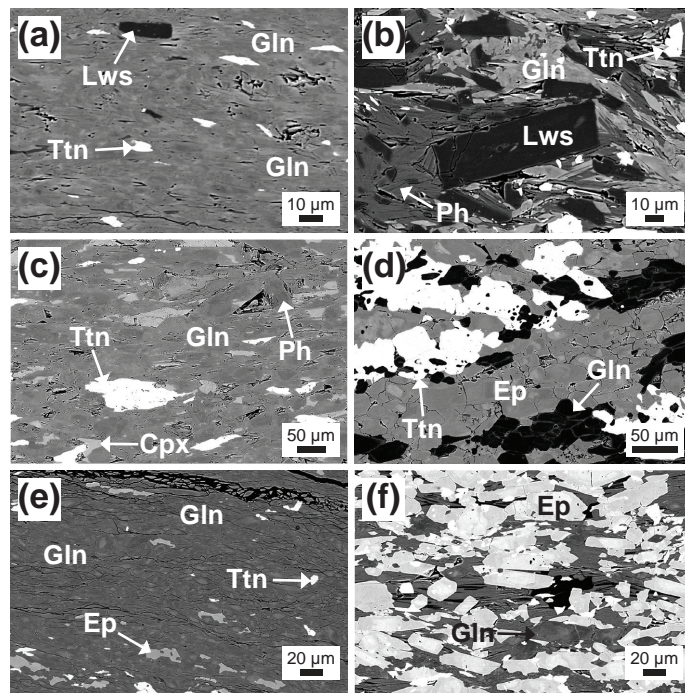


Fig. 3.2. Backscattered electron images of the analyzed samples. (a) Glaucophane-rich and (b) lawsonite-rich layers in NI-01. (c) CZ-02. (d) Omi-02. (e) Glaucophane-rich and (f) epidote-rich layers in Omi-03. Mineral abbreviations follow those in Whitney and Evans (2010).

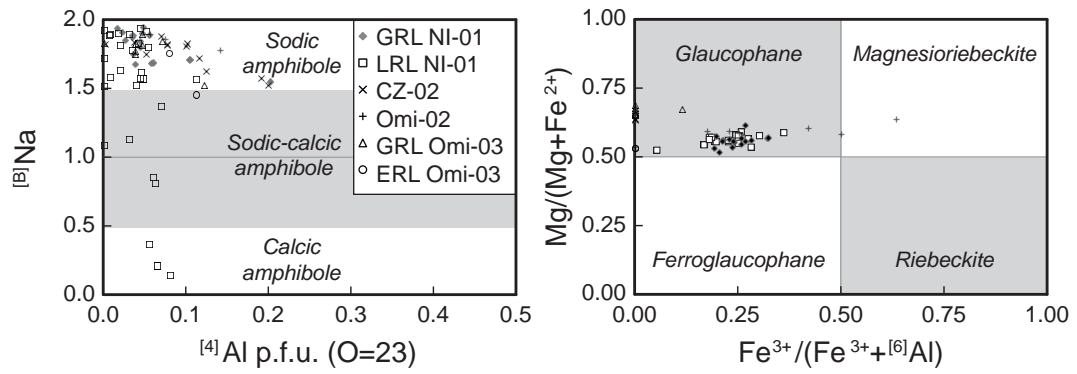


Fig. 3.3. Chemical compositions of the amphiboles. Ferric iron was calculated from the average of the maxima and minima estimated according to a total of 15 cations at T, C, and B sites, and 13 cations at T and C sites (Leake et al., 1997).

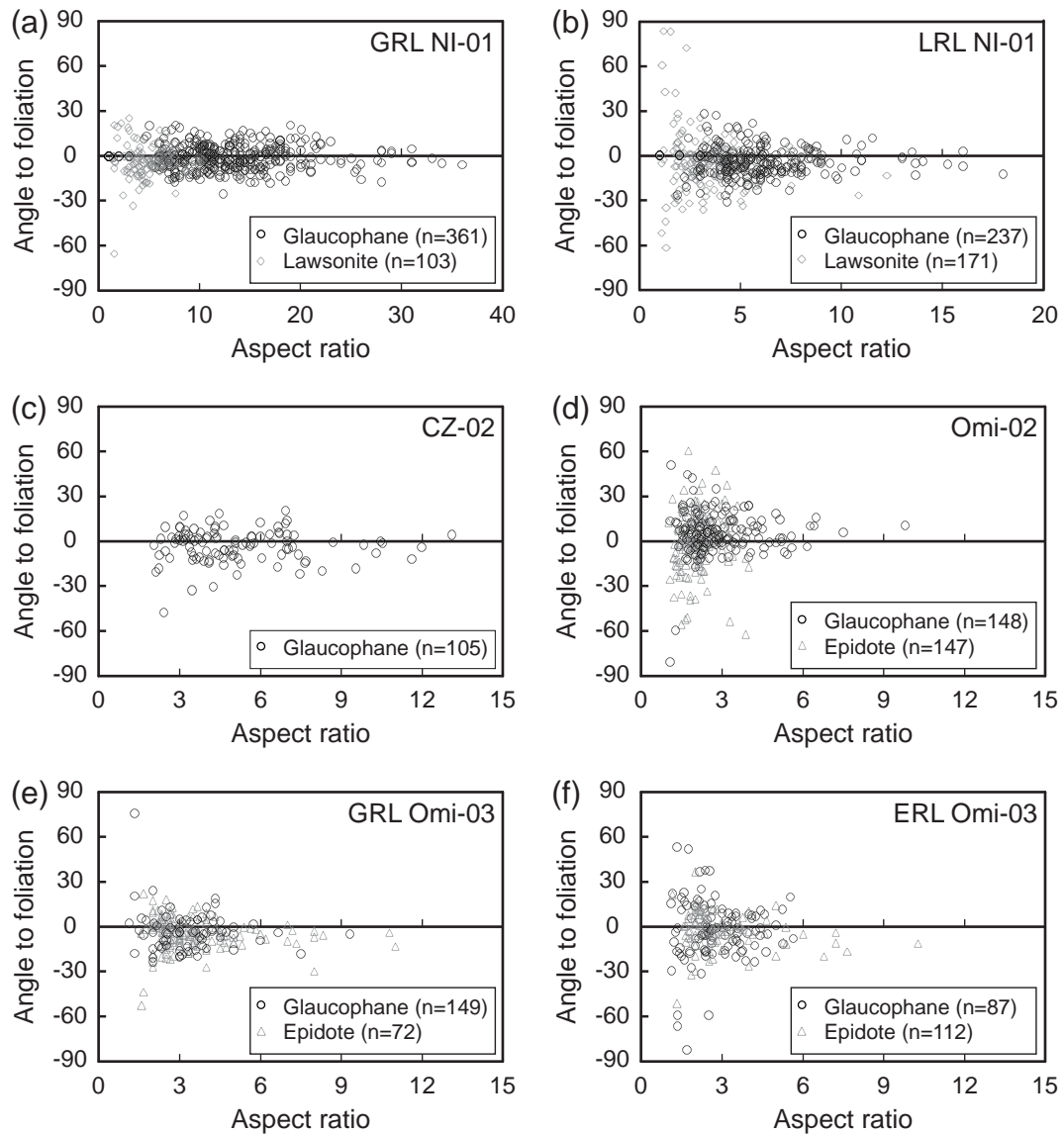


Fig. 3.4. Angles between grain long-axes and the mean foliation plane vs. aspect ratios, as calculated using the image-analysis software ImageJ 1.44 (<http://rsb.info.nih.gov/ij/>). Best-fit ellipses were used to reduce the complexity of diverse shapes.

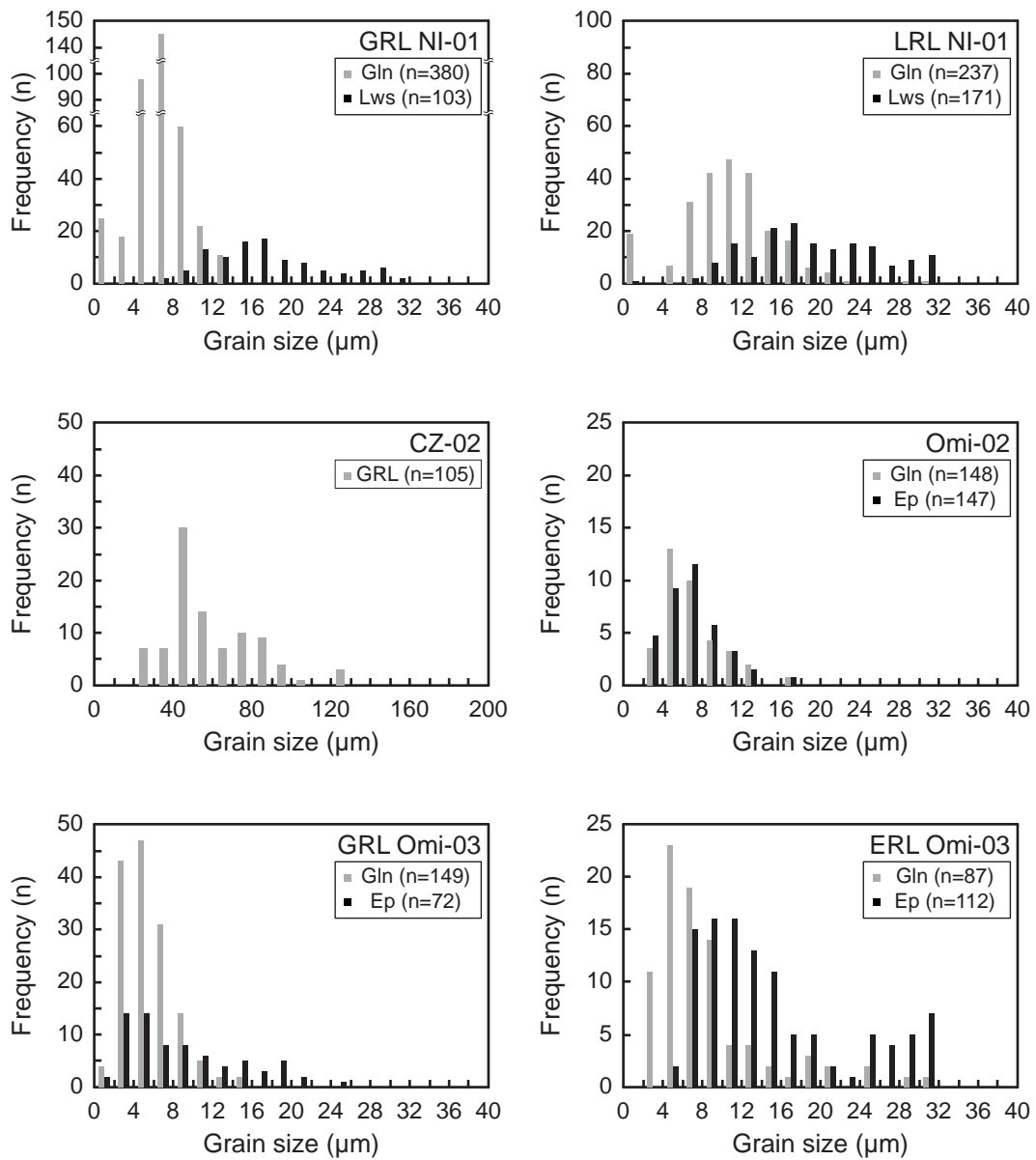


Fig. 3.5. Grain size distributions. A square grain shape was assumed for grain size calculations. See the text for details.

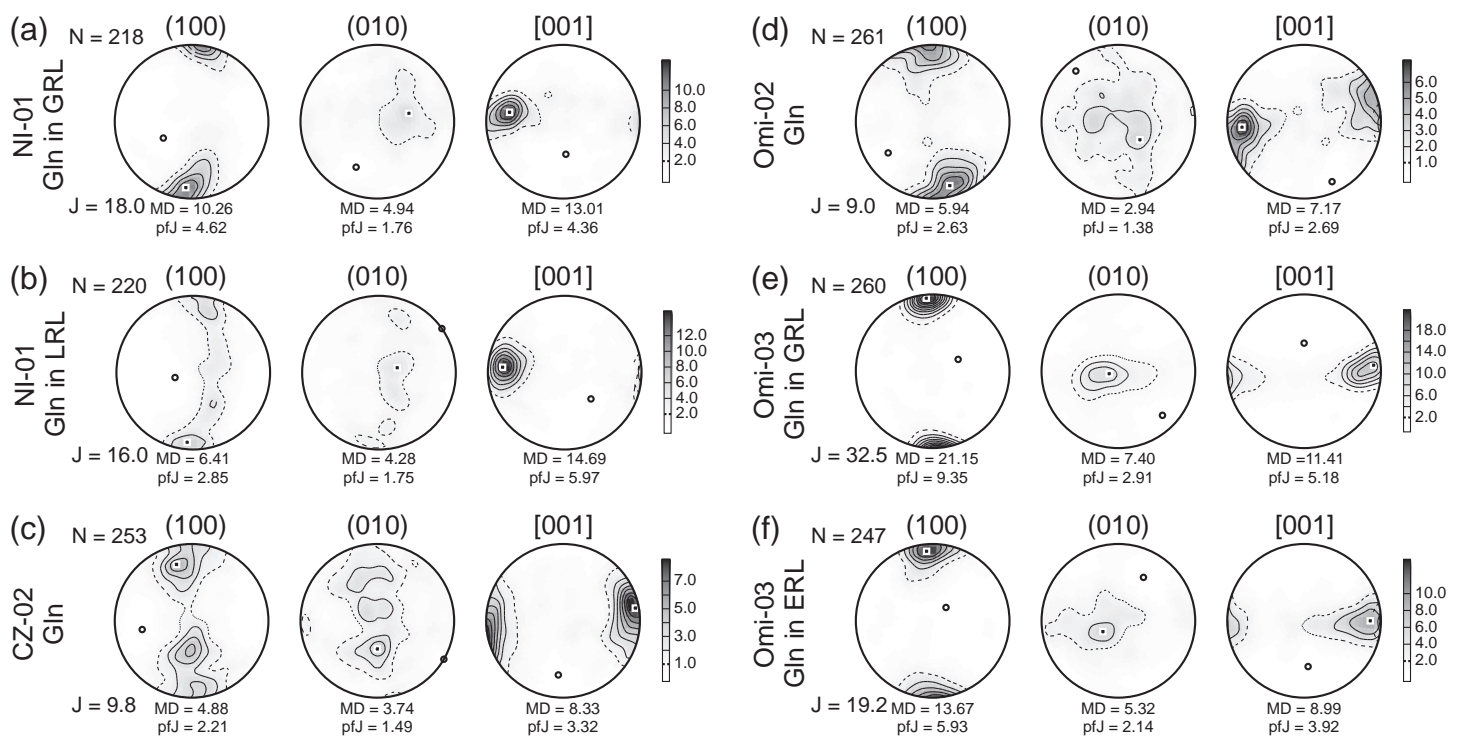


Fig. 3.6. Pole figures for glaucophane in the analyzed samples. Poles were plotted on lower hemisphere equal-area projections with contours in multiples of uniform distribution (m.u.d) for the density of poles. N: Number of measurements; J: J-index; MD: Maximum density.

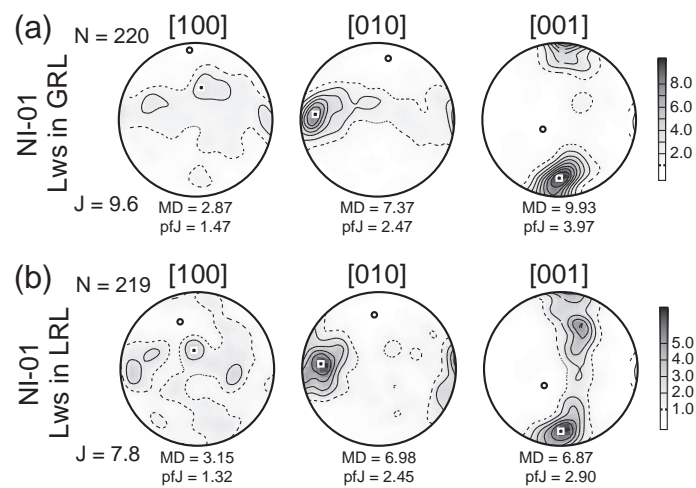


Fig. 3.7. Pole figures for lawsonite in the New Idria blueschist (NI-01).

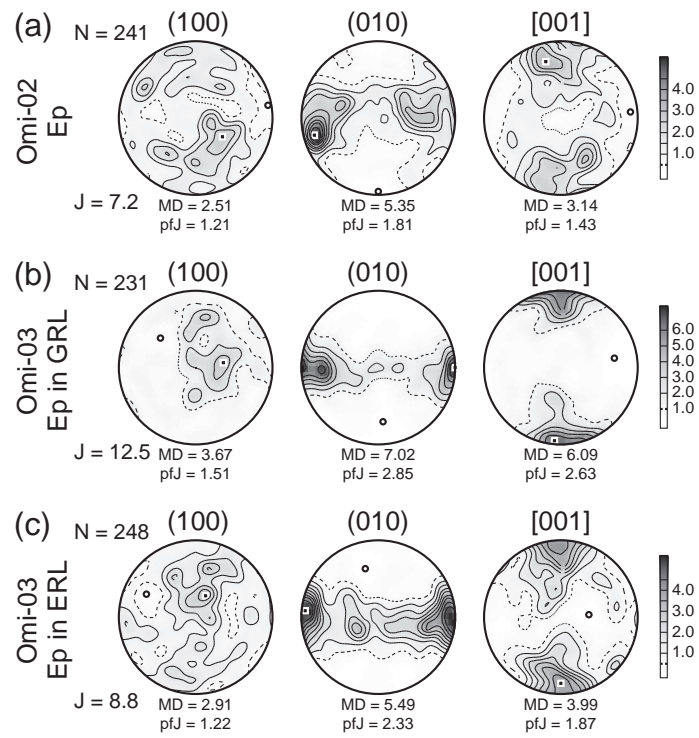


Fig. 3.8. Pole figures for epidote in the Omi blueschists (Omi-02 and 03).

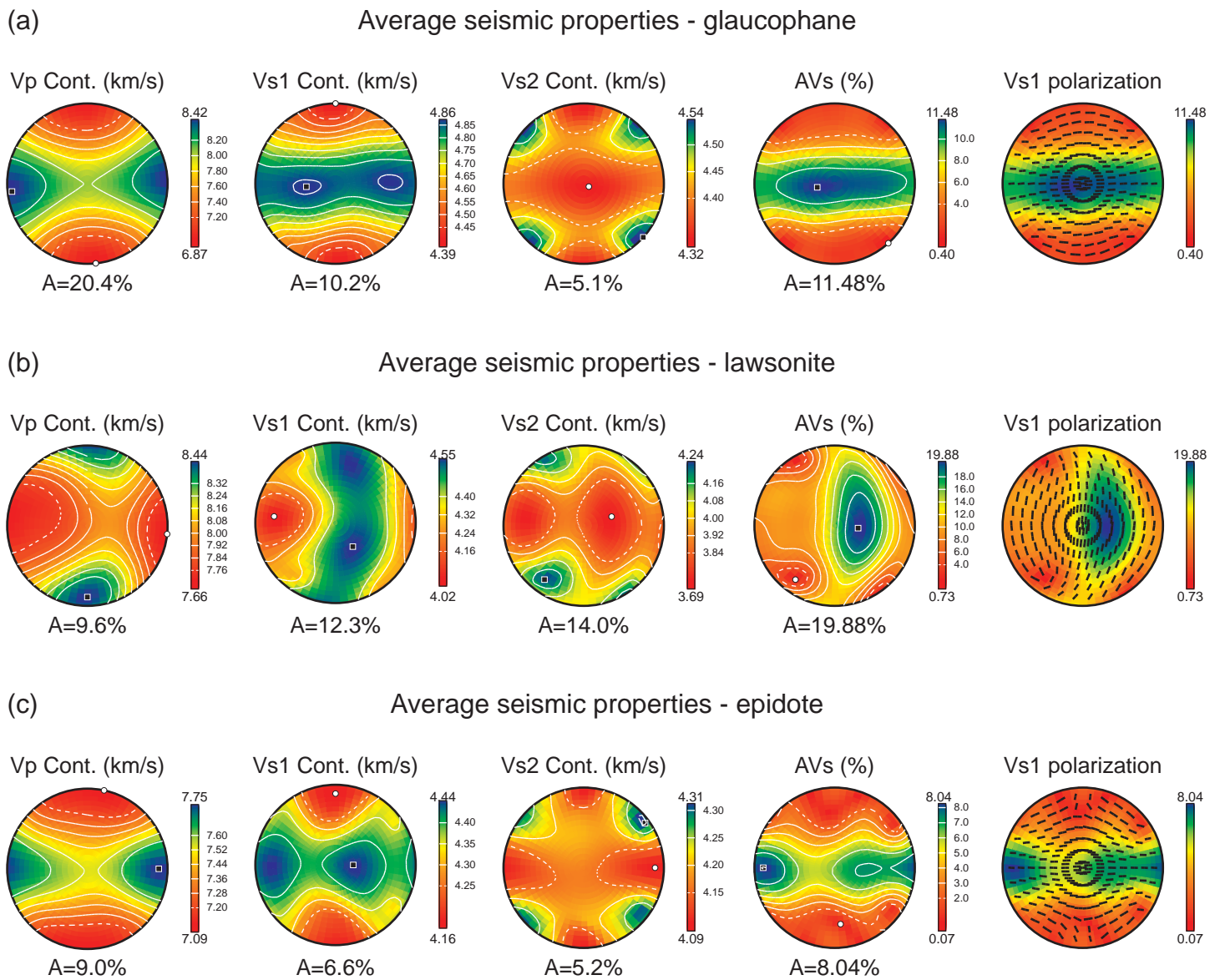
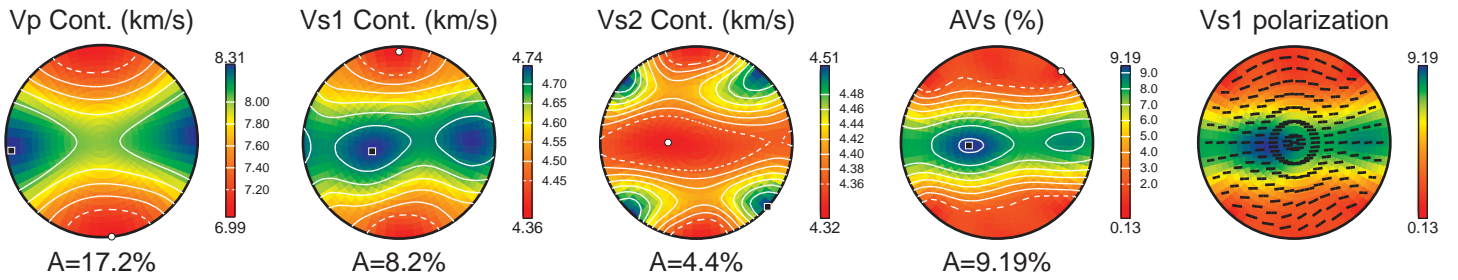
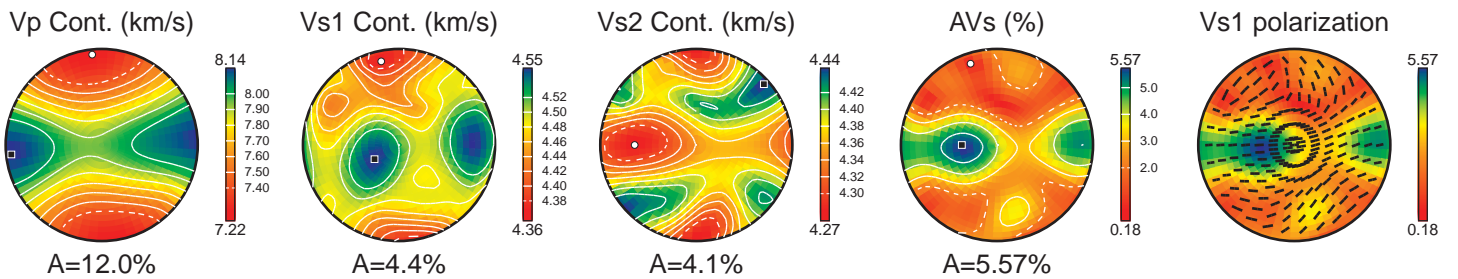


Fig. 3.9. Calculated seismic anisotropies of (a) average glaucophane, (b) lawsonite, and (c) epidote. The Voigt-Reuss-Hill averaging scheme and lower hemisphere equal area projections are used.

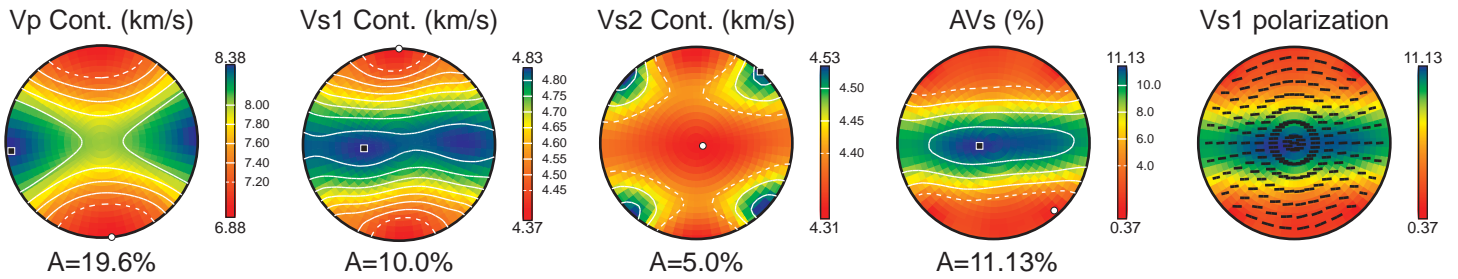
(a) Average seismic properties - a lawsonite blueschist (Gln:Lws=91:9, GRL_NI-01)



(b) Average seismic properties - a lawsonite blueschist (Gln:Lws=75:25, LRL_NI-01)



(c) Average seismic properties - an epidote blueschist (Gln:Ep=94:6, GRL_Omi-03)



(d) Average seismic properties - an epidote blueschist (Gln:Ep=26:74, ERL_Omi-03)

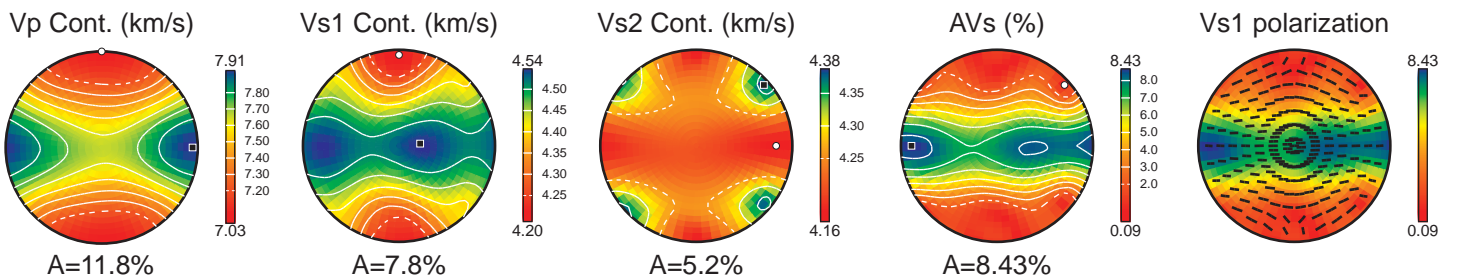


Fig. 3.10. Seismic anisotropy evaluated for lawsonite blueschists (a) GRL NI-01 and (b) LRL NI-01, and epidote blueschists (c) GRL Omi-03 and (d) LRL Omi-03.

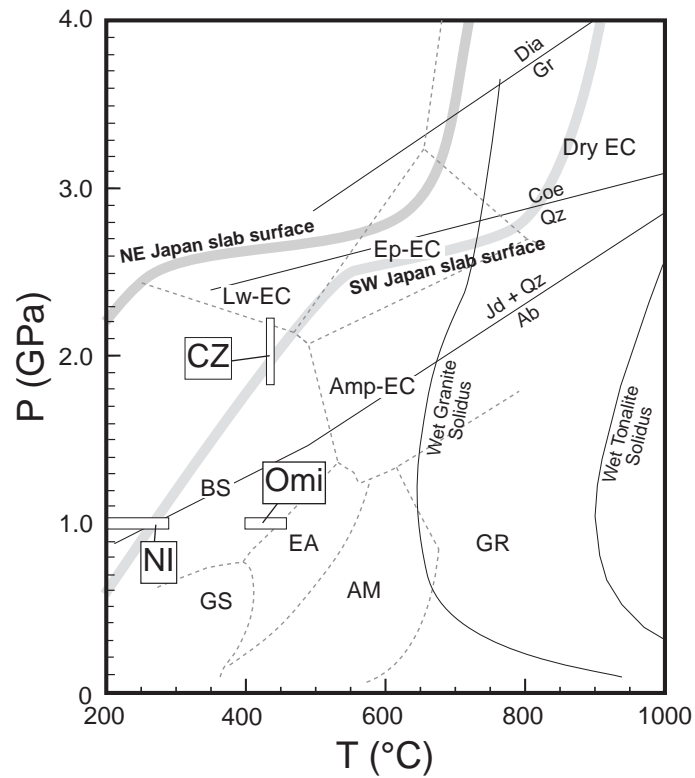


Fig. 3.11. Deformational P–T conditions for the analyzed samples. The pressure–temperature paths for NE and SW Japan are after Syracuse et al. (2010). GS: greenschist; AM: amphibolite; EA: epidote amphibolite; GR: granulite; BS: blueschist; Amp-EC: amphibole eclogite; Lw-EC: lawsonite eclogite; Ep-EC: epidote eclogite; Dry EC: dry eclogite; NI: NI-01; CZ: CZ-02; Omi: Omi-02 and 03.

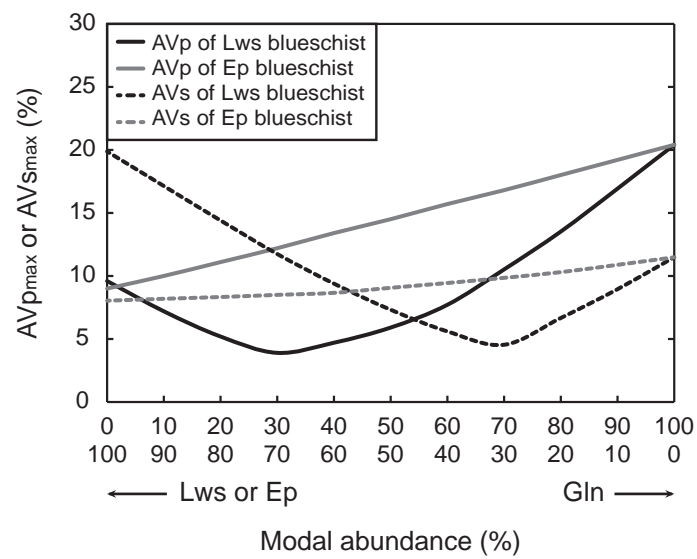


Fig. 3.12. A graph for AVPmax and AVSmax according to modal abundance. The AVPmax and AVSmax of blueschists were computed from the average of the seismic anisotropies of glaucophane and lawsonite with every 10% step.

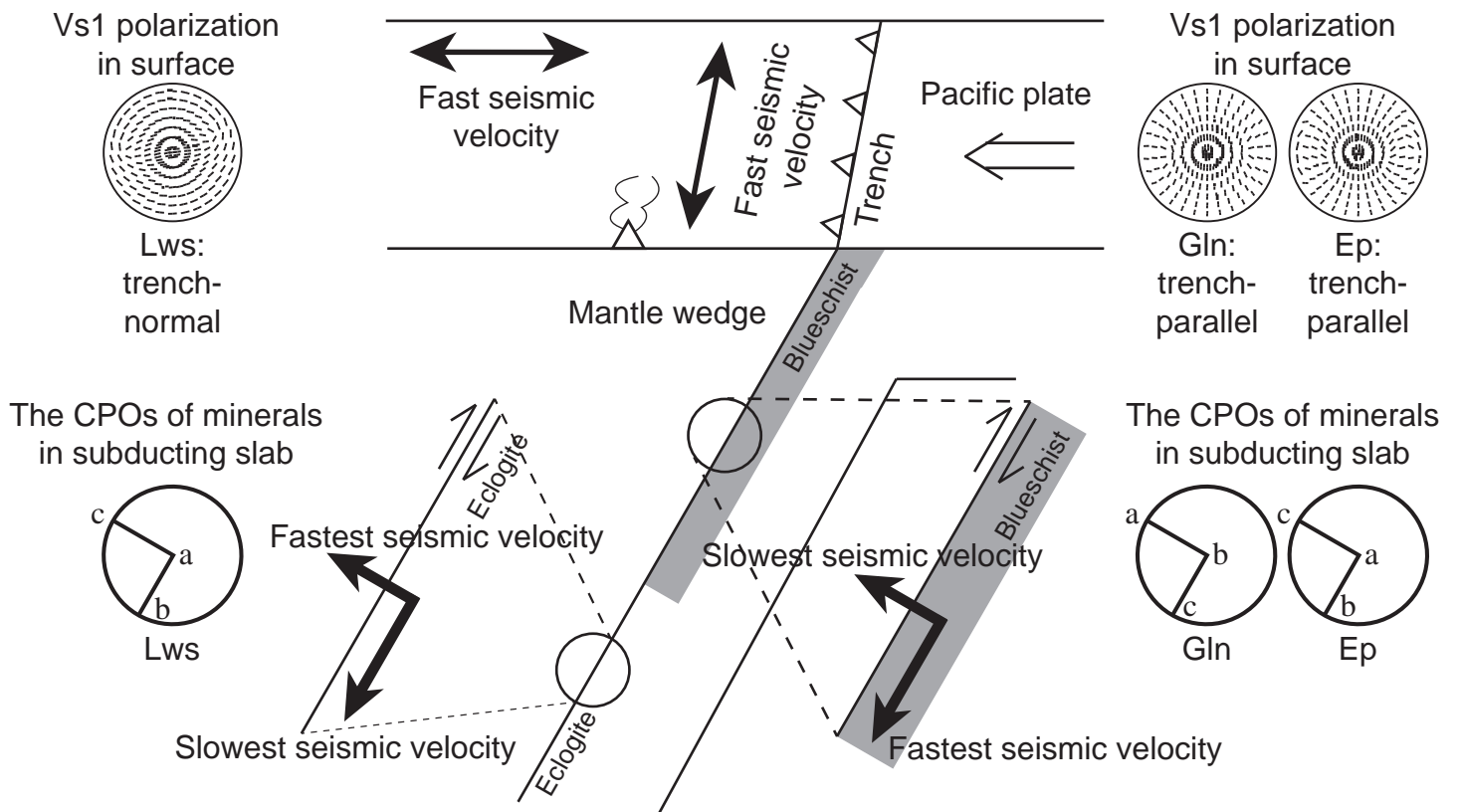


Fig. 3.13. A schematic model showing trench-parallel and trench-normal fast anisotropies. The subducting angle is assumed to be 60° , however the patterns of Vs1 polarization at the surface is based on 90° of subducting angle.

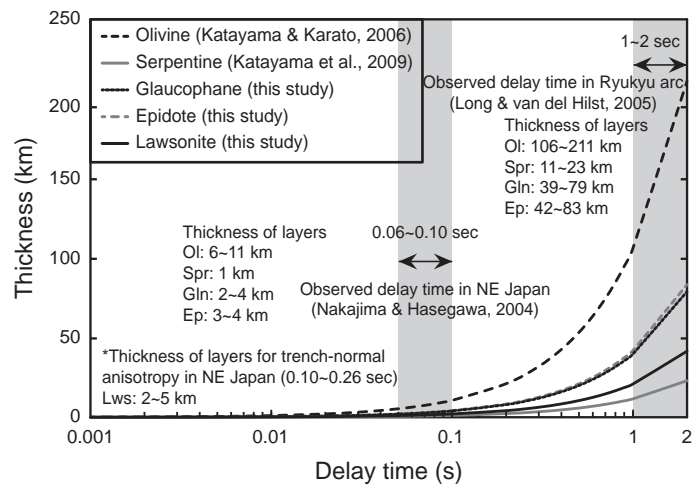
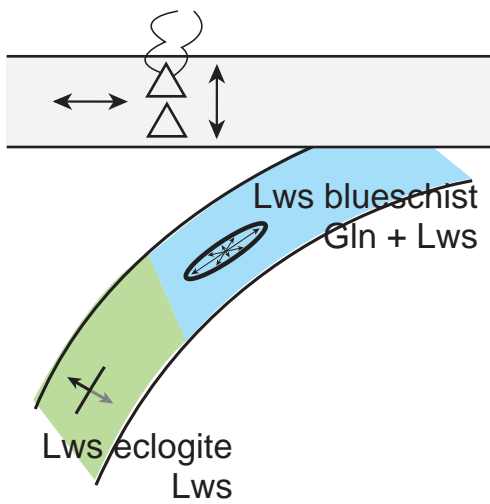


Fig. 3.14. Relationship between the calculated thickness of the anisotropic layer and the delay time. The delay time and thickness of an anisotropic layer of olivine ($AVS = 4.5\%$, $\langle VS \rangle = 4.75$ km/s; Katayama and Karato, 2006) and serpentine ($AVS = 35.9\%$, $\langle VS \rangle = 4.13$ km/s; Katayama et al., 2009) are also plotted for comparison.

a. NE Japan (old)



b. Ryukyu arc (young)

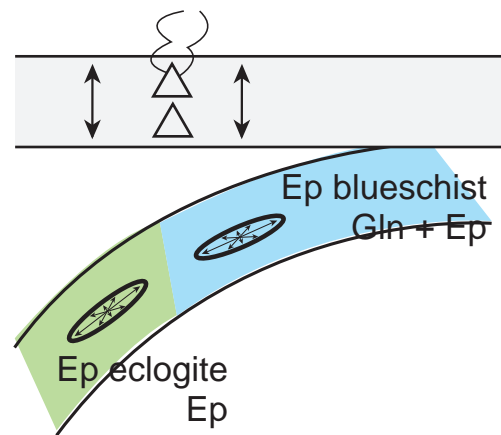


Fig. 3.15. Application of the schematic model to a geologic setting around Japan. a. Seismic anisotropy of lawsonite blueschist is governed by the combination of glaucophane and lawsonite, whereas that of lawsonite eclogite is controlled by lawsonite. b. Strong anisotropic phases are glaucophane and epidote in epidote blueschist, and epidote in epidote eclogite.

Table 3.1. Sample locations and the results of fabric analysis

Sample numbers	Location (latitude, longitude)	Lithology	Mode* (%)	Minerals	Grain size with std. dev. (μm)	Aspect ratio with std. dev.	Fabric strength (CPO)		Seismic anisotropy (%)	
							Number	J	AVp	AVs
GRL_NI-01	36° 38', -120° 71'	Lawsonite blueschist	Gln89, Lws8	Gln	7 \pm 3	12.8 \pm 6.4	218	18.0	25.3	13.9
				Lws	18 \pm 6	5.0 \pm 2.3	220	9.6	10.7	21.3
LRL_NI-01	36° 38', -120° 71'	Lawsonite blueschist	Gln64, Lws21	Gln	12 \pm 5	6.0 \pm 2.8	220	16.0	20.2	9.9
				Lws	20 \pm 8	3.6 \pm 1.5	219	7.8	8.8	19.4
CZ-02	36° 54', -123° 11'	Grt-bearing lawsonite blueschist	Gln81, Cpx8, Grt4	Gln	59 \pm 29	5.2 \pm 2.3	253	9.8	17.7	8.4
Omi-02	36° 85', 137° 74'	Grt-bearing epidote blueschist	Gln54, Ep27, Ttn10, Grt5	Gln	18 \pm 7	3.0 \pm 1.4	261	9.0	19.5	10.4
				Ep	18 \pm 7	2.1 \pm 0.6	241	7.2	7.1	5.6
GRL_Omi-03	36° 81', 137° 74'	Epidote blueschist	Gln91, Ep6	Gln	6 \pm 3	3.5 \pm 1.6	260	32.5	29.5	18.4
				Ep	10 \pm 6	3.4 \pm 1.4	231	12.5	11.1	11.9
ERL_Omi-03	36° 81', 137° 75'	Epidote blueschist	Ep57, Gln20, Ph19	Gln	9 \pm 6	3.0 \pm 1.6	247	19.2	27.5	16.6
				Ep	17 \pm 10	2.8 \pm 1.1	248	8.8	9.7	8.5

Mode* excludes phengite, titanite and apatite (abundances of each mineral are less than 5%). Gln: glaucophane; Lws: lawsonite, Cpx: clinopyroxene; Grt: garnet; Ttn: titanite; Ep: epidote; Ph: phengite; Number: number of measurements; J: *J*-index, respectively.

Table 2. Chemical compositions of representative sodic amphiboles in each sample.

Sample No.	NI-01								Omi-03				
Area	Glaucofane-rich layer		Lawsonite-rich layer		CZ-02		Omi-02		Glaucofane-rich layer		Epidote-rich layer		
Spot No.	110408-8	110408-10	110401-50C	110401-51R	120419-51C	120419-47R	120419-26	120419-21	120419-01C	120419-02R	120419-12C	120419-11R	
SiO ₂	55.39	53.53	56.33	56.35	57.41	56.84	57.46	56.84	55.44	56.21	55.87	54.33	
TiO ₂	0.04	0.02	0.1	-	0.04	0.01	-	-	0.07	-	0.06	0.05	
Al ₂ O ₃	7.11	8.73	8.62	7.84	11.52	10.33	11.22	11.19	3.6	8.43	8.36	5.82	
Cr ₂ O ₃	0.03	0.02	0.02	0.03	0.04	0.04	-	0.03	0.02	0.03	0.01	0.02	
FeO*	16.4	16.04	15.09	14.94	9.18	10.28	10.18	10.18	19.33	14.99	15.16	16.34	
MnO	0.16	0.24	0.07	0.21	0.09	0.19	0.03	0.02	0.13	0.16	0.17	0.19	
MgO	8.63	9.05	8.54	9.18	10.44	10.43	9.99	9.83	9.81	8.79	9.18	10	
CaO	1.27	1.29	0.41	2.28	1.08	1.32	0.68	0.96	0.59	0.65	1.1	3.12	
Na ₂ O	6.92	6.32	7.51	6.15	7.06	6.66	7.31	7.2	7.1	7.32	6.85	5.8	
K ₂ O	0.01	0.02	0.02	0.03	0.02	0.01	-	-	-	0.01	0.01	0.03	
Total	95.95	95.24	96.71	97	96.87	96.11	96.87	96.23	96.08	96.59	96.76	95.69	
<i>Cations</i>	<i>O=23</i>	<i>O=23</i>	<i>O=23</i>	<i>O=23</i>	<i>O=23</i>	<i>O=23</i>	<i>O=23</i>	<i>O=23</i>	<i>O=23</i>	<i>O=23</i>	<i>O=23</i>	<i>O=23</i>	
Si	7.96	7.8	7.96	7.98	7.92	7.95	7.94	7.93	8	7.95	7.92	7.89	
Ti	0	0	0.01	-	0	0	-	-	0.01	-	0.01	0.01	
Al	1.2	1.5	1.44	1.31	1.88	1.7	1.83	1.84	0.61	1.41	1.4	1	
Cr	0	0	0	0	0	0	-	0	0	0	0	0	
Fe ³⁺	0.54	0.46	0.46	0.29	0	0	0	0.17	1.04	0.46	0	0	
Fe ²⁺	1.43	1.49	1.32	1.48	1.06	1.2	1.18	1.02	1.3	1.32	1.8	1.98	
Mn	0.02	0.03	0.01	0.03	0.01	0.02	0	0	0.02	0.02	0.02	0.02	
Mg	1.85	1.97	1.8	1.94	2.15	2.18	2.06	2.04	2.11	1.85	1.94	2.17	
Ca	0.2	0.2	0.61	0.35	0.16	0.2	0.1	0.14	0.09	0.1	0.17	0.49	
Na	1.93	1.79	2.06	1.69	1.89	1.81	1.96	1.86	1.99	2.01	1.88	1.63	
K	0	0	0	0.01	0	0	-	-	0.16	0.12	0	0.01	
Total	15.13	15.24	15.67	15.07	15.08	15.06	15.07	15	15.32	15.23	15.14	15.19	
gln	0.66	0.75	0.77	0.7	0.96	0.93	0.99	0.89	0.38	0.75	0.98	0.84	
mrh	0.31	0.27	0.26	0.16	0	0	0	0.09	0.65	0.25	0	0	
act	0.38	0.32	0.12	0.68	0.3	0.37	0.19	0.28	0.17	0.19	0.31	0.89	
ts	0	0.01	0	0	0	0	0	0	0	0	0	0.01	

* C, core; R, rim; -, not detected. FeO* indicates total Fe as Fe2+. The Fe3+ calculation of glaucofane employs the average of maximum and minimum values (Leake et al., 1997)

Chapter IV

DEFORMATION MECHANISMS OF GLAUCOPHANE AND LAWSONITE: IMPLICATIONS FROM EXPERIMENTALLY DEFORMED BLUESCHISTS

Abstract

Pure and simple shear experiments at 400–500 °C and 1–2.5 GPa were conducted to better understand the pressure effects for deformation behaviors of blueschist, which contains frequent occurrence of seismicity in subducting oceanic crust beneath NE Japan. Mechanical data of pure shear experiments show a pressure-sensitive increase of shear stress at low confining pressure and a pressure-insensitive increase of stress at high pressure, implying a change of deformation mechanism of blueschist with an increase of pressure. Brittle deformation features of microstructures are dominant at 1–2 GPa experiments, in contrast to abundant strain-localized area at 2.5 GPa. *J*-index of glaucophane CPOs is systematically decreased with shear strain and confining pressure and angle of slip plane to shear direction is similar to that of strain ellipsoid at >2 GPa. Therefore those results imply the change of deformation behaviors of glaucophane from brittle failure to brittle-ductile transition probably at ~2 GPa. However evidence for the occurrence of ductile deformation in this study is relatively weak for glaucophane. On the other hand, although lawsonite has angle of slip plane to shear direction comparable to that of strain ellipsoid at 2.5 GPa, frequent occurrence of relict minerals even in specimens deformed at 2.5 GPa and feeble relation among *J*-index, shear strain, and confining pressure demonstrate no change of deformation mechanism of lawsonite during the whole experimental conditions.

Therefore the results of this study indicates that observed seismicity in subducting oceanic crust beneath NE Japan is attributed to brittle or semi-brittle behaviors of glaucophane at 1–2.5 GPa condition and additional experiments at higher pressure are needed.

4.1. Introduction

Blueschist in the subducting oceanic crust could be the most effective fluid carrier to deeper mantle owing to its distribution in depth and the largest amounts of fluid in it (5–6 wt% in lawsonite blueschist) based on mineral formulas and modal abundance of rock-forming minerals (Schmidt and Poli, 1998; Hacker et al., 2003a). Recent electron backscatter diffraction (EBSD) measurements for natural blueschists suggested that combinations of glaucophane and lawsonite in blueschist could occur trench-parallel seismic anisotropy in forearc beneath NE Japan, and trench-normal anisotropy in backarc can be caused by lawsonite in eclogite (Kim et al., 2013a). In addition, seismicity beneath NE Japan shows abundant microearthquakes within blueschist of the subducting oceanic crust and rare within eclogite-stable area (Kita et al., 2006), implying deformation behaviors or dehydration embrittlement of blueschist as possible cause of seismicity distribution. However there is no experimental data for lawsonite blueschist (representative for a cold subducting crust), therefore deformational behaviors of blueschist are fundamentally needed.

Studies on deformation behaviors of blueschist focused mostly on main rock-forming minerals in natural blueschists. Via TEM observations, Reynard et al. (1989) reported dislocation glide and recovery processes with various slip systems along (100)[001], (110)[001], (010)[100], (110) $1/2$ [110], and (001) $1/2$ [110] from an eclogitic micaschist and along (010)[001] from a blueschist-facies micaschist.

Another investigations using quantitative fabric analysis suggested that glaucophane deforms by rigid body rotation (Ildefonse et al., 1990). Recent studies employing EBSD technique described slip systems of glaucophane as $\{110\}[001]$, $(100)[001]$ (Bezacier et al., 2010; Fujimoto et al., 2010; Cao et al., in press). For deformation behaviors of lawsonite, Teyssier et al. (2010) considered lawsonite as a rigid phase and Kim et al. (2013b) suggested rigid body rotation as deformation mechanism of lawsonite. However the microstructures in natural blueschists have been formed during decompression stage, therefore it may contain limitation to directly apply these results to subducting oceanic crust.

Deformation experiments using a Griggs-type solid-medium apparatus were conducted at high pressures and temperatures within stability field of blueschist. Here I present deformational behaviors of glaucophane and lawsonite in blueschist mostly proved by microstructural observations and electron backscattered diffraction (EBSD) measurements. In addition, geological implications of deformation behaviors of hydrous phases will be discussed for delineating distribution of microearthquakes beneath NE Japan.

4.2. Experimental procedures

The starting material is a natural lawsonite blueschist from New Idria serpentinite body, California; same sample was used for estimating rheological contrast between glaucophane and lawsonite (Kim et al., 2013b). The highly deformed blueschist has strong fabrics and two distinct layers: glaucophane-rich and lawsonite-rich layers. The glaucophane-rich layer is composed of over than 90% of glaucophane and very few amounts of lawsonite and titanite, while the lawsonite-rich layer comprises ~70% of glaucophane, large amounts (~20%) of lawsonite, phengite

surrounding lawsonite, and a few titanite. Basically the glaucophane-rich layer was included for this study, however it could be heterogeneous due to the lawsonite-rich layer.

Using a modified Griggs-type solid-medium apparatus housed at Hiroshima University (see Ando et al., 2006), I conducted two kinds of deformation experiments under pure shear and simple shear regimes. By pure shear experiments, the samples were deformed to 10 % of bulk shear strain (ϵ) at a constant strain rate ($\sim 4.7 \times 10^{-4}$ to $\sim 1.1 \times 10^{-5} \text{ s}^{-1}$) (Table 1). The cylindrically cored sample of ~ 10 mm thick was surrounded by a Ni jacket (Fig. 4.1a) and put it into NaCl cylinders. The temperature, monitored by two Pt/Rh thermocouple, was initially increased to 200 °C with a rate of ~ 30 °C/min and then pressure was raised to 400 MPa. Finally temperature was increased to 400–500 °C and then pressure was raised to 0.5–2 GPa. After temperature and pressure were stabilized, the piston was activated at a constant strain rate (500 $\mu\text{m/h}$) until the maximum stress was attained and maintained.

By simple shear experiments, the sample was deformed to diverse bulk shear strain ($\gamma = \sim 0.57$ to ~ 1.79) at constant strain rates ($\sim 4.7 \times 10^{-4}$ to $\sim 1.1 \times 10^{-5} \text{ s}^{-1}$) (Table 1). The cylindrically cored sample was cut as very thin layer ($\sim 500 \mu\text{m}$) and sandwiched between alumina pistons which were cut at an angle of 45° from the direction of compression (Fig. 4.1b). A nickel jacket was used for dry condition. Grooves were made in the surface of alumina piston for preventing the occurrence of slip between the piston and sample. Shear strain was calculated from the rotation of the nickel strain marker that was initially aligned normal to the shear direction.

4.3. Results

4.3.1. Mechanical data of pure shear experiments

Although the starting material could be heterogeneous, mechanical data acquired from pure shear experiments are relatively reliable hence I used them to unravel deformational behaviors of minerals. Shear stress is directly proportional to increased pressure in brittle failure regime, whereas it is unconnected with pressure in brittle-ductile (semi-brittle) transition zone (e.g., Kohlstedt et al., 1995). Therefore the change on deformation behaviors from cataclastic faulting to semi-brittle could be recognized by comparisons of maximum stress corresponding to confining pressure. The mechanical data of pure shear experiments in a fixed temperature condition (500 °C) were plotted to figure 4.2. Experiments at 0.5 GPa show different maximum stresses and curves, possibly caused by heterogeneity of the starting material (Fig. 4.2a). Maximum stresses are estimated to 609 MPa (Hi-462) and 827 MPa (Hi-472) at 0.5 GPa, 994 MPa at 1 GPa (Hi-460), and 1171 MPa at 2 GPa (Hi-461). The graph of maximum stress as a function of confining stress displays that the stress increase from 0.5 to 1 GPa (~276 MPa) is higher than the change from 1 to 2 GPa (~177 MPa) (Fig. 4.2b).

On the other hand, mechanical data of simple shear experiments contain lots of errors possibly caused by the amounts of NaCl cylinder in the specimen, high frictions at high pressures, and the occurrence of slip between the specimen and the alumina piston and within the specimen. Therefore I report here approximate trends only using raw data (Fig. 4.3). Curves acquired at low-pressure experiments (blue color) show a narrow range of the lowest axial load of starting point (14.91–17.66 kN) and a broad range of the highest axial load (33.61–40.52 kN). Two curves at 1.5 GPa also exhibit a narrow axial load at starting point (22.45–23.89 kN) and a broad maximum axial load (36.82–51.08 kN). The 2 GPa experiments have a narrow axial load at the beginning (25.85–27.38 kN) and a wide maximum axial load (38.31–57.94 kN).

Experiments at 2.5 GPa display a narrow axial load at starting point (37.67–39.72 kN) and a wide range of the maximum axial load (44.15–60.85 kN). The trend of narrow axial load at the beginning and wide maximum axial load is probably attributed to heterogeneity of the starting material. In 1.5 and 2.0 GPa experiments, curves at higher temperature have smaller maximum axial load.

4.3.2. Microstructures of specimens deformed under simple shear regime

Microscopic observations were conducted using optical and electron microscopy (EPMA and SEM) housed at Hiroshima University. The starting material initially includes strong fabrics characterized by euhedral lawsonite and dynamically recrystallized glaucophane (Kim et al., 2013b). Deformed microstructures exhibit three common characteristics (Fig. 4.4). (a) Most samples have microcracks developed by fast strain rate ($\sim 10^{-4} \text{ S}^{-1}$), except Hi-450 deformed at relatively low strain rate ($\sim 10^{-5} \text{ S}^{-1}$) and Hi-448 deformed at the highest pressure and temperature conditions (500 °C and 2.5 GPa). (b) Microstructures of glaucophane are invisible owing to very fine grain size in the starting material ($\sim 8 \text{ }\mu\text{m}$), whereas those of lawsonite and titanite are obvious. (c) Samples deformed at low pressures (1 to 1.5 GPa) display microcracks, while specimens deformed at high pressures (2 to 2.5 GPa) exhibit flow structures of lawsonite and titanite.

Detailed microstructures are systematic according to the increase of confining pressure. The detailed microstructures of samples deformed at 1 and 1.5 GPa exhibit frequent occurrence of relict (depicted as ‘R’) glaucophane, lawsonite, and titanite (Fig. 4.5a and d). In the specimens deformed at 2 GPa, many grains are fully fractured due to localized strain (expressed as ‘SL’), but still the relict minerals are rarely occurred (Fig. 4.5b and e). Strain is more localized in the samples deformed at 2.5

GPa hence grain size of relict minerals is bigger than that in the specimens at 2 GPa (Fig. 4.5c and f). The area of localized strain is more common at 2.5 GPa.

4.3.3. EBSD measurements

Crystal preferred orientations (CPOs) of glaucophane and lawsonite were acquired using an Oxford–HKL–EBSD on a Hitachi S-3400 scanning electron microscope (SEM) housed at Shizuoka University, Japan. The electron backscattered diffraction (EBSD) patterns (Randle, 1992; Prior et al., 1999; Randle and Engler, 2000) were measured with an accelerating voltage of 20 kV, a working distance of 28 mm, and a beam current of ca. 10 nA. The Kikuchi bands were manually indexed for each grain. The number of analysis points was higher than 200 to ensure the reliability of data. Pole figures were plotted using the software PFch5 designed by D. Mainprice, and the fabric strength was determined by the J -index (Bunge, 1982; Mainprice and Silver, 1993).

Glaucophane CPOs show strong (100) planes as a slip plane and weak [010] or [001] axes as a slip direction; originally those were the (100)[001] slip systems in the starting material (Fig. 4.6). Pole figures of lawsonite also have strong a slip plane along (001) and a weak slip direction along [100] or [010]; initially these were the (001)[010] before the experiments (Fig. 4.7). These results suggest the preserved slip planes during deformation nonetheless slip axes have no relations with strains, confining pressures, and temperatures. Strength of poles (J -index) is well organized for glaucophane and relatively random for lawsonite, implying strain localization effectively into glaucophane rather than lawsonite during the deformation (Figs. 4.8 and 4.9). Also I measured and plotted the angle of slip plane to shear direction according to shear strains with angular changes of strain marker and strain ellipsoid

(Fig. 4.10). Mainly these graphs will be used in discussion for deformation mechanism of glaucophane and lawsonite.

4.4. Discussion and conclusions

Investigations on deformation mechanisms of glaucophane and lawsonite are important to understand the distributions of seismicity within oceanic crust beneath NE Japan (Kita et al., 2006). Although calcic amphibole is regarded as one of the strongest materials in the lower crust (e.g., Brodie and Rutter, 1985), it may have similar deformation behavior to glaucophane owing to its same belonging to amphibole group. Previous studies usually focused on deformation mechanisms of calcic amphibole (hornblende) for delineating mechanical properties of the lower continental crust. Experimental studies reported that clinoamphiboles under very high strain rates normally deform by (101) mechanical twinning, together with (100)[001] dislocation glide without dynamic recrystallization (Rooney et al., 1970, 1975; Dollinger and Blacic, 1975). Dislocation glide, incipient dynamic recrystallization, fracturing, and partial melting of amphibole were described at high temperature conditions (Hacker and Christie, 1990; Huang et al., 2003). Although these results took place under extreme deformation conditions, the deformation mechanisms are likely to apply for natural amphiboles.

In this study, mechanical data, microstructures, and CPOs of glaucophane and lawsonite were investigated by deformation experiments under pure and simple shear regimes. Throughout pure shear experiments, mechanical data were examined for the notable change of mechanical behaviors from pressure-sensitive brittle failure to pressure-insensitive brittle-ductile transition. The mechanical data display that the increase of maximum stress from 0.5 to 1 GPa is higher than that from 1 to 2 GPa

(Fig. 4.2b). The results imply pressure-sensitive behaviors at low pressure and pressure-insensitive behaviors at high pressure. Therefore these could suggest that 1 to 2 GPa conditions are the lowest pressures for brittle-ductile transition of the lawsonite blueschist.

From simple shear experiments, microscopic observations and EBSD measurements of highly strained samples were conducted. Although microstructures of glaucophane are difficult to observe because of very fine grain size, those of lawsonite and titanite could be obviously monitored. According to pressure increase, microstructures are systematically changed. The detailed microstructures of specimens deformed at 1 and 1.5 GPa show the relict grains of glaucophane and lawsonite with few strain localized region, probably caused by brittle failure (Fig. 4.5a and d). Samples deformed at 2 GPa show relatively rare relict phases and some strain-localized areas (Fig. 4.5b and e). Specimens deformed at 2.5 GPa show flow structures, which might be attributed to ductile flow or semi-brittle deformation. In addition, strain-localized area is frequently observed and relict phases are bigger than the minerals at 2 GPa deformed samples, possibly due to the activation of strain localization. Therefore systematic change on microstructures of experimentally deformed specimens demonstrates the start of brittle-ductile transition probably at 2–2.5 GPa.

The comparisons of glaucophane and lawsonite CPOs could give us information for deformation mechanisms (e.g., Barrie et al., 2011). The J -index expresses strength of microstructures hence its relations with shear strain and confining pressure were employed to recognize the effects of deformation to each mineral. Figure 4.8 exhibits change of J -index in a factor of shear strain and relations between J -index and confining pressure are depicted in figure 4.9. Glaucophane has a negative correlation

of *J*-index to shear strain, indicating successful response of strain to deformation degree (Fig. 4.8a). In addition, *J*-indices of specimens become similar in high-strain, suggesting strain equilibrium after 100 % of shear strain. The influence of confining pressure is for mostly samples, having 100 % of strain, deformed at 500 °C, denoting that 400 °C is too low to deform glaucophane effectively (Fig. 4.9a). *J*-index is getting decreased at low pressure but shows small increase at 2.5 GPa, possibly attributed to the characteristics of ductile deformational behaviors (Fig. 4.9a). Lawsonite displays relatively scattered patterns of correlation between *J*-index and shear strain (Fig. 4.8b), and *J*-index and confining pressure (Fig. 4.9b). The results probably suggest heterogeneity of strain to lawsonite grains, possibly indicating strong stiffness of lawsonite.

The poles of slip direction have relatively random and diverse changes hence only angular changes of slip plane were employed with some assumptions. When brittle failure occurs, the angular change of foliation could be similar to that of strain marker due to scarce change of mineral orientation for the occurrence of microcracks (e.g., Vernooij et al., 2006). At higher pressure, glaucophane and lawsonite could flow to shear direction by ductile deformational behaviors. Thus the angular change of foliation could be higher than that of strain ellipsoid when ductile deformation occurs (e.g., Zhang and Karato, 1995). If angular change is similar to that of strain ellipsoid, deformation of minerals could be still in brittle-ductile transition zone. Based on these assumptions, the angular changes of slip plane with flow direction were plotted as a function of shear strain (Fig. 4.8). The angle of (100) peaks of glaucophane deformed at 1 GPa follows that of strain marker, suggesting occurrence of brittle failure (Fig. 4.6a). The angle of samples deformed at 1.5 GPa displays one at strain marker and another at strain ellipsoid, possibly implying the start of brittle-

ductile transition. The points of angle deformed at 2–2.5 GPa show higher or similar angle than that of strain ellipsoid. However the distribution of angle is random and many of angles are still close to angle of strain ellipsoid, indicating the semi-brittle or ductile behaviors. On the other hand, the angle of (001) planes of lawsonite mostly follows that of strain marker. Only samples deformed at 2.5 GPa and few at 2 GPa have higher or similar angle with strain ellipsoid, therefore brittle-ductile transition of lawsonite starts from 2 GPa condition. However, the angle of slip planes is similar to strain ellipsoid hence the interpretation of this graph will be discussed with other results.

Above all data acquired from microstructural observations and EBSD measurements support that the brittle-ductile transition zone of glaucophane starts at ~2 GPa. However, the start of ductile deformational behaviors needs more discussion. Although *J*-index is systematically changed by shear strain and confining pressure, the angle of foliation to flow direction at 2–2.5 GPa is similar to that of strain ellipsoid (Fig. 4.10a) and detailed microstructures still have relict minerals according to strong strain localization (Figs. 4.5c and f). In addition, experimental temperatures in this study (400–500 °C) is too low to compare with the temperature for crystal plasticity of clinoamphibole higher than 650–700 °C in the presence of fluid (Berger and Stünitz, 1996). Therefore 2.5 GPa condition is close to the area of ductile deformation of glaucophane, however there is no additional evidence for ductility. Accordingly the boundary of brittle failure and brittle-ductile transition for glaucophane is at ~2 GPa, but the boundary of brittle-ductile transition and ductile flow is difficult to check in experimental conditions of this study (1–2.5 GPa). On the other hand, deformation behaviors of lawsonite have rare evidence. Although the angle of foliation to flow direction has correlations with pressure increase, the

detailed microstructures of lawsonite show abundant relicts in whole experimental pressure conditions and J -index of lawsonite is scarcely related with shear strain and confining pressure. Therefore the results of this study indicate lawsonite show brittle failure in the whole experimental conditions.

Based on mechanical information of other minerals, possible depth of ductile behaviors of glaucophane is estimated. Dry quartz was used for the representative of crust, and dry olivine was employed for the proxy of mantle materials, with Byerlee's law as brittle fracturing (Fig. 4.11). The line of brittle fracturing meets with mechanical behaviors of ductile flow of quartz at ~50 km depth (Fig. 4.11a), and those of olivine at ~120 km depth (Fig. 4.11b). With the boundary between brittle and brittle-ductile transition at 2 GPa, the graph indicates that glaucophane may have brittle deformational behavior until ~65–120 km depth (Fig. 4.12). To consider depth of rock-type transformation from blueschist to eclogite ~110 km, the findings of this study imply glaucophane can be a powerful candidate for intermediate-depth earthquake generations in subducting oceanic crust.

In summary, mechanical data of pure shear experiments, microstructures, and angular change of foliation plane of specimens deformed under simple shear suggest brittle-ductile transition of glaucophane occurred at ~2 GPa, lawsonite at >2.5 GPa, and thence lawsonite blueschist probably at >2–2.5 GPa conditions. Additional experiments and microstructural analysis at higher pressure should be followed for delineating the upper limit of brittle-ductile transition. Consequently the results of this study demonstrate that brittle-ductile transition of blueschist occur at relatively shallow depth (< ~80 km depth), therefore the occurrence of seismicity in subducted oceanic crust beneath NE Japan is possibly attributed to the semi-brittle behaviors of lawsonite blueschist.

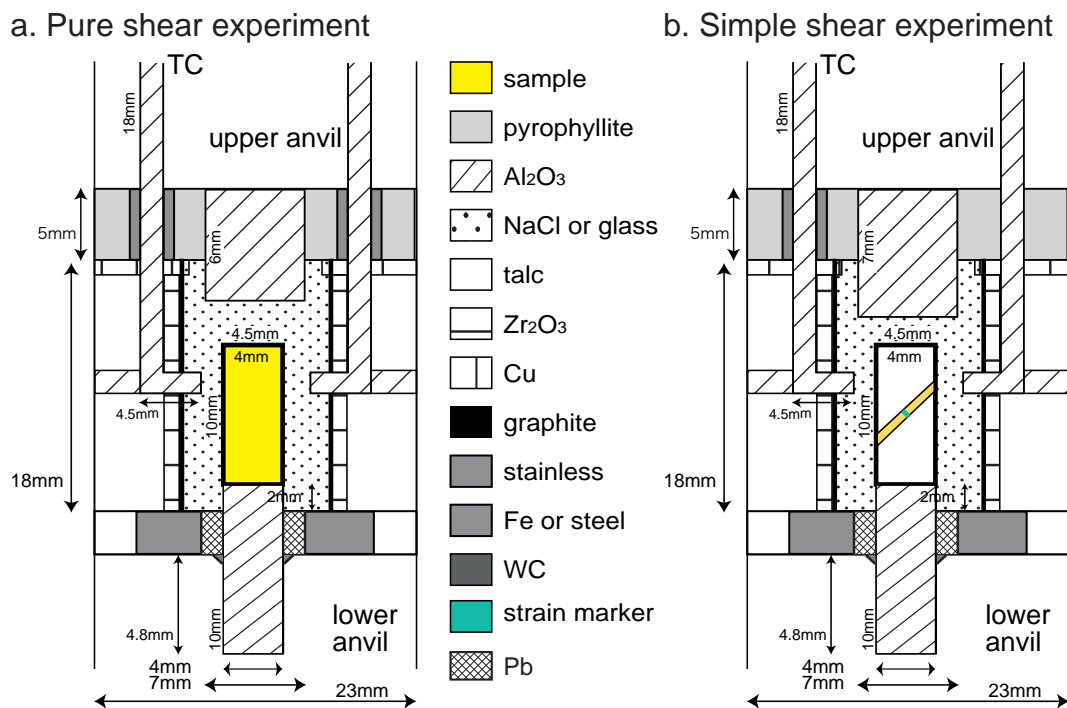
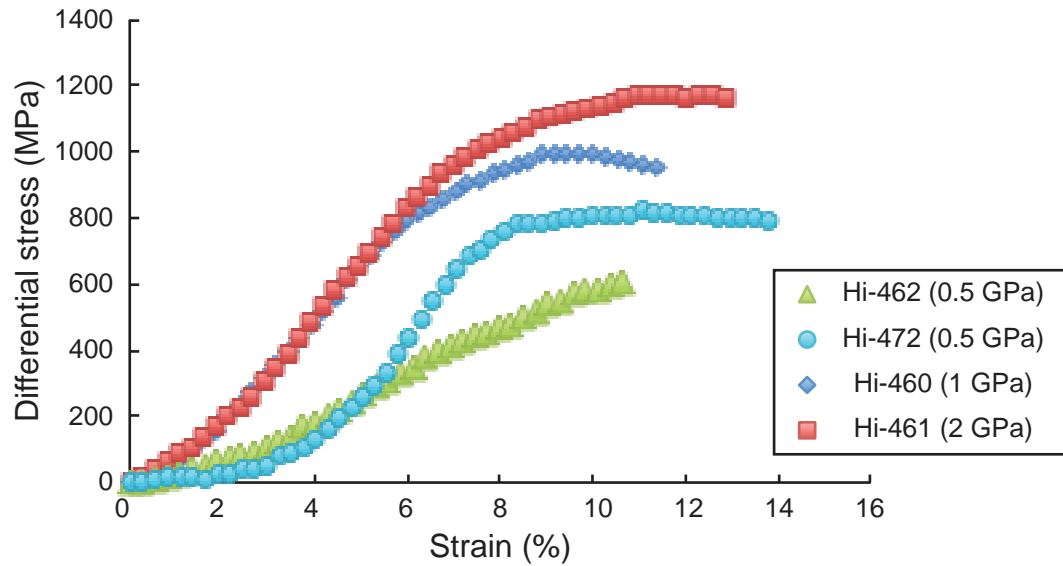


Fig. 4.1. Experimental assemblies of pure-shear (a) and simple-shear (b) experiments. Instead of 7 mm pistons (e.g., Ando et al., 2006), 4 mm pistons were employed to reduce frictions.

a. Stress-strain curve



b. Maximum stresses

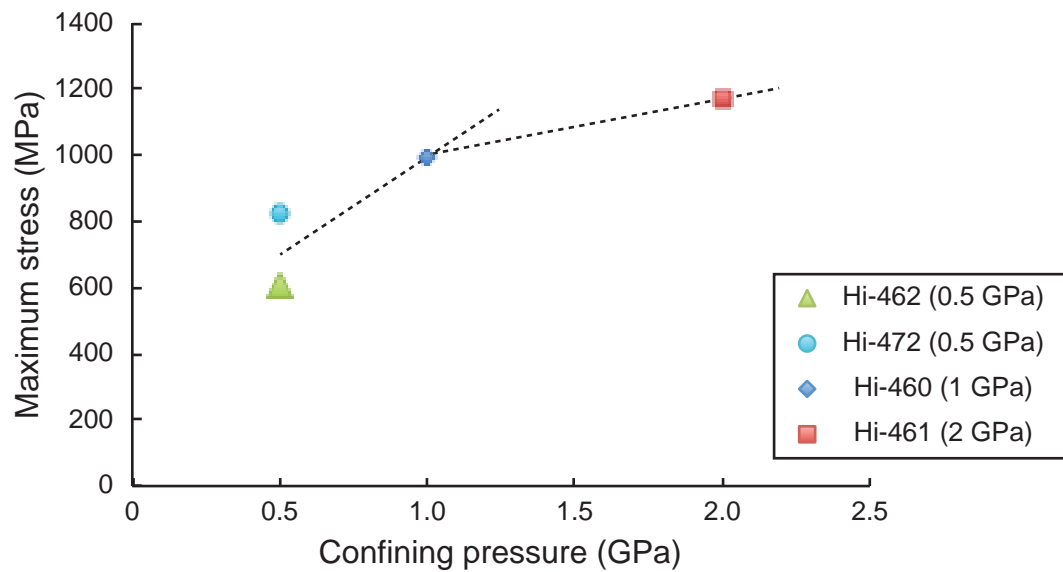


Fig. 4.2. Mechanical data of pure shear experiments conducted at 500 °C. a. Stress-strain curve shows systematic increase of differential stresses. b. Maximum stress was measured from stress-strain curve.

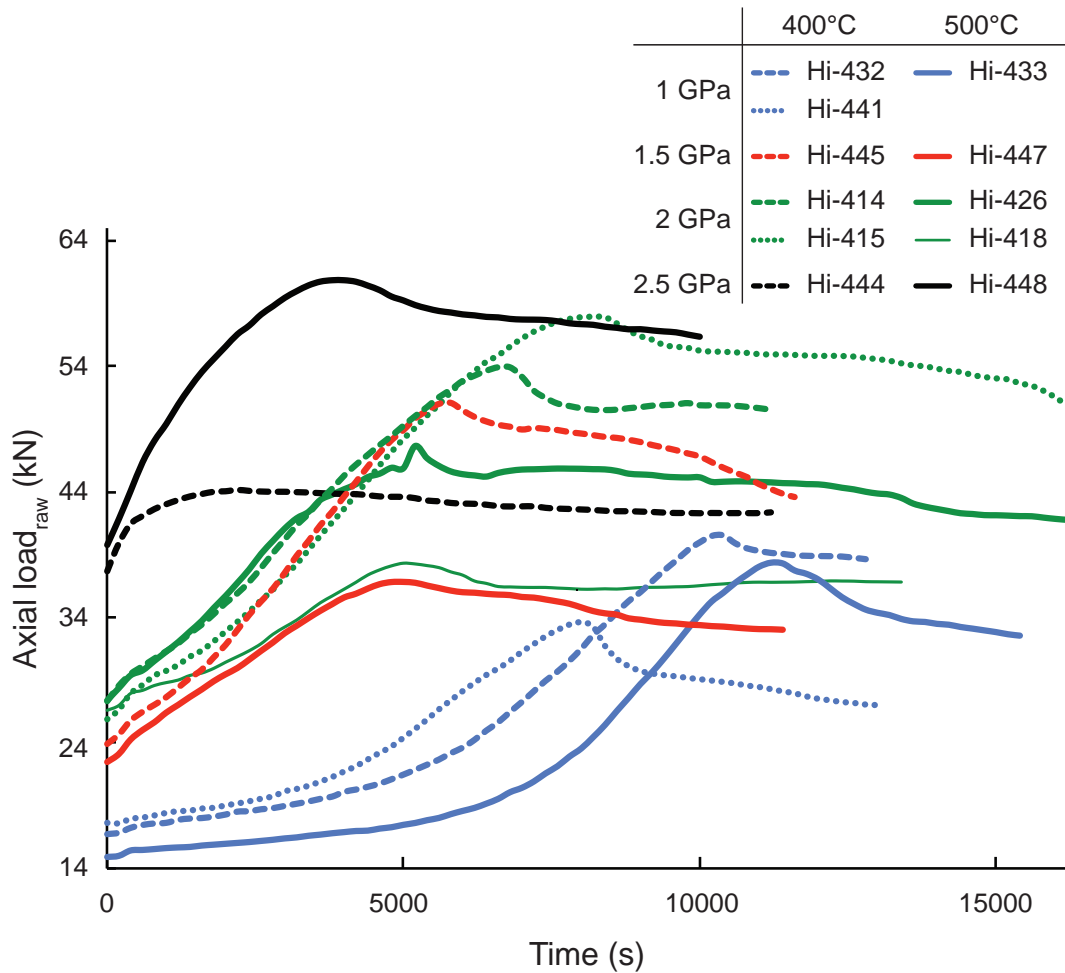


Fig. 4.3. Mechanical data of simple shear experiments. Raw data was displayed due to difficulties to pick up the point, in which the specimen attached to upper piston. These data could also contain lots of uncorrected errors owing to frictions.

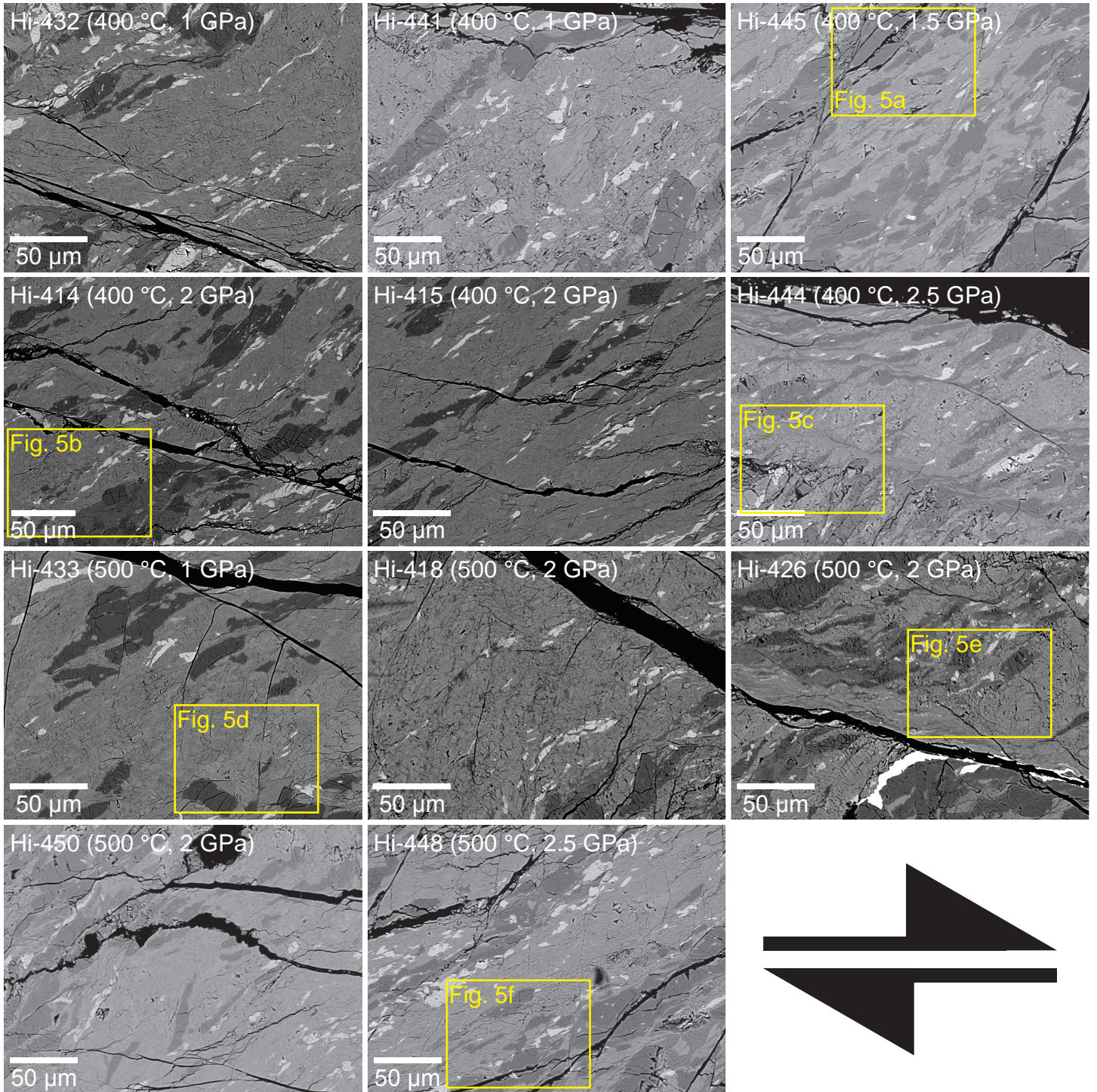


Fig. 4.4. Back-scattered electron images of all experimental specimens. Yellow rectangles are enlarged in Figure 4.5.

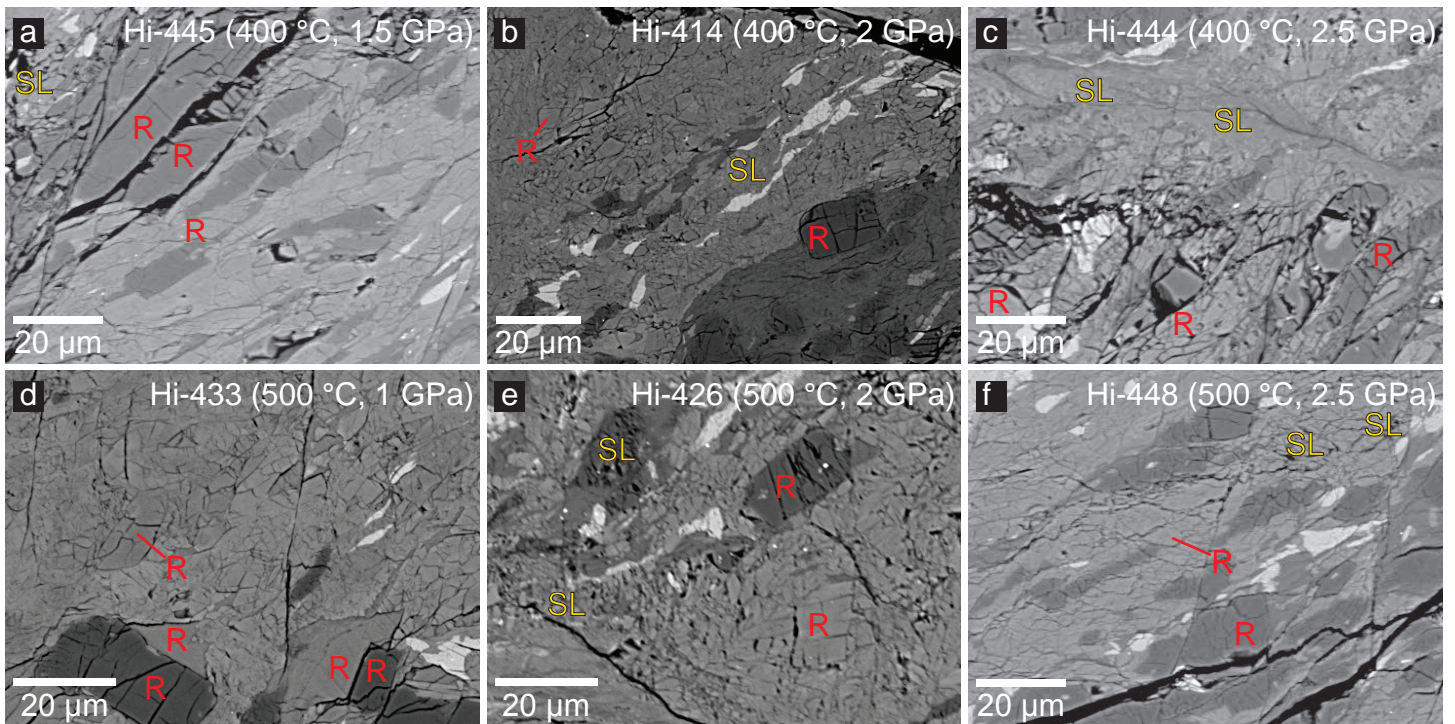


Fig. 4.5. Detailed microstructures of deformed specimens. Red R presents relict minerals from deformation and strain-localized area is expressed as yellow SL.

Glauconite (400 °C)

Glauconite (500 °C)

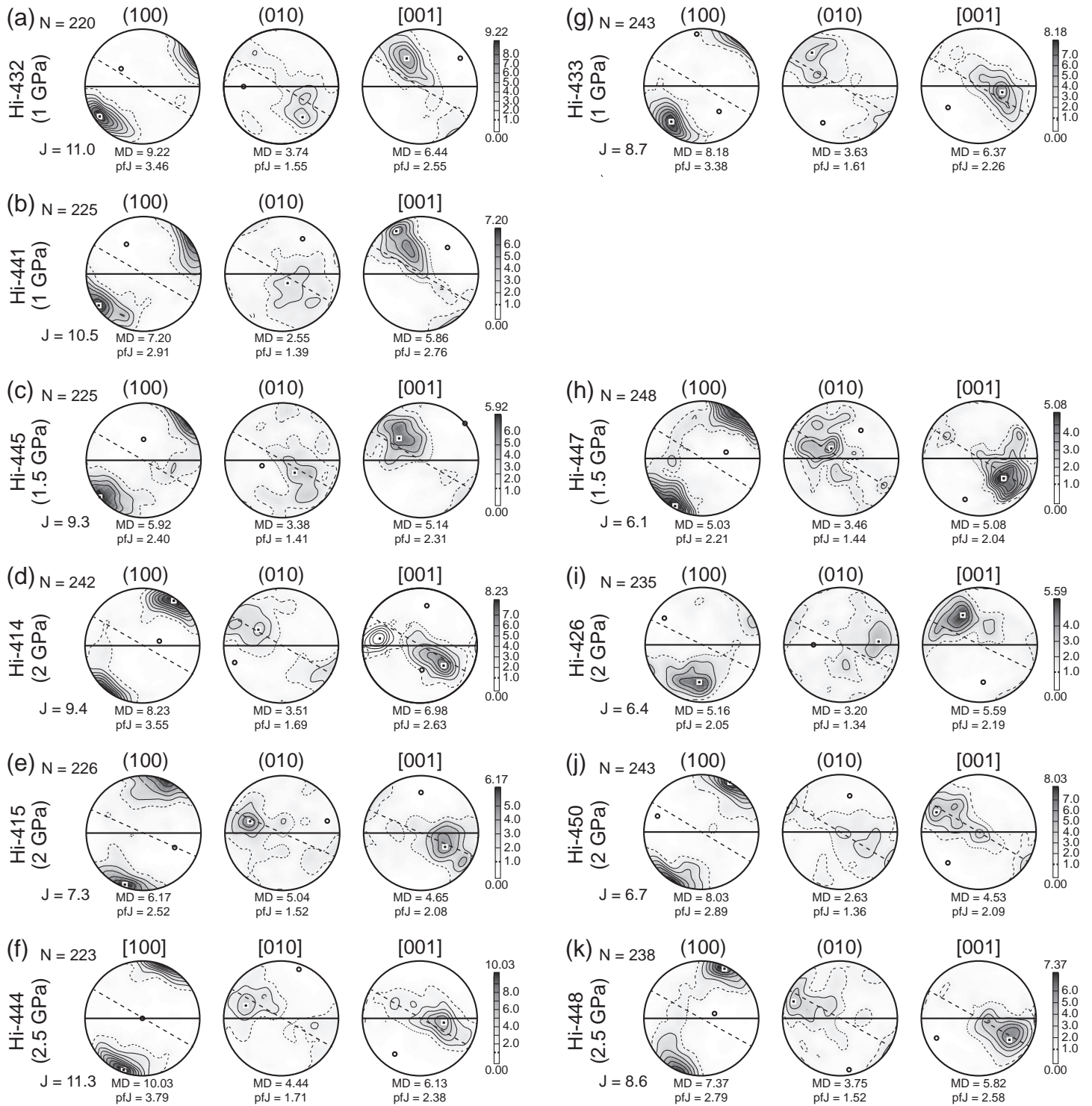


Fig. 4.6. Pole figures of glauconite in deformed samples. Every contour has 1 density difference. N: number of analysis point; J: J-index; MD: mean density; pfJ: J-index of the pole.

Lawsonite (400 °C)

Lawsonite (500 °C)

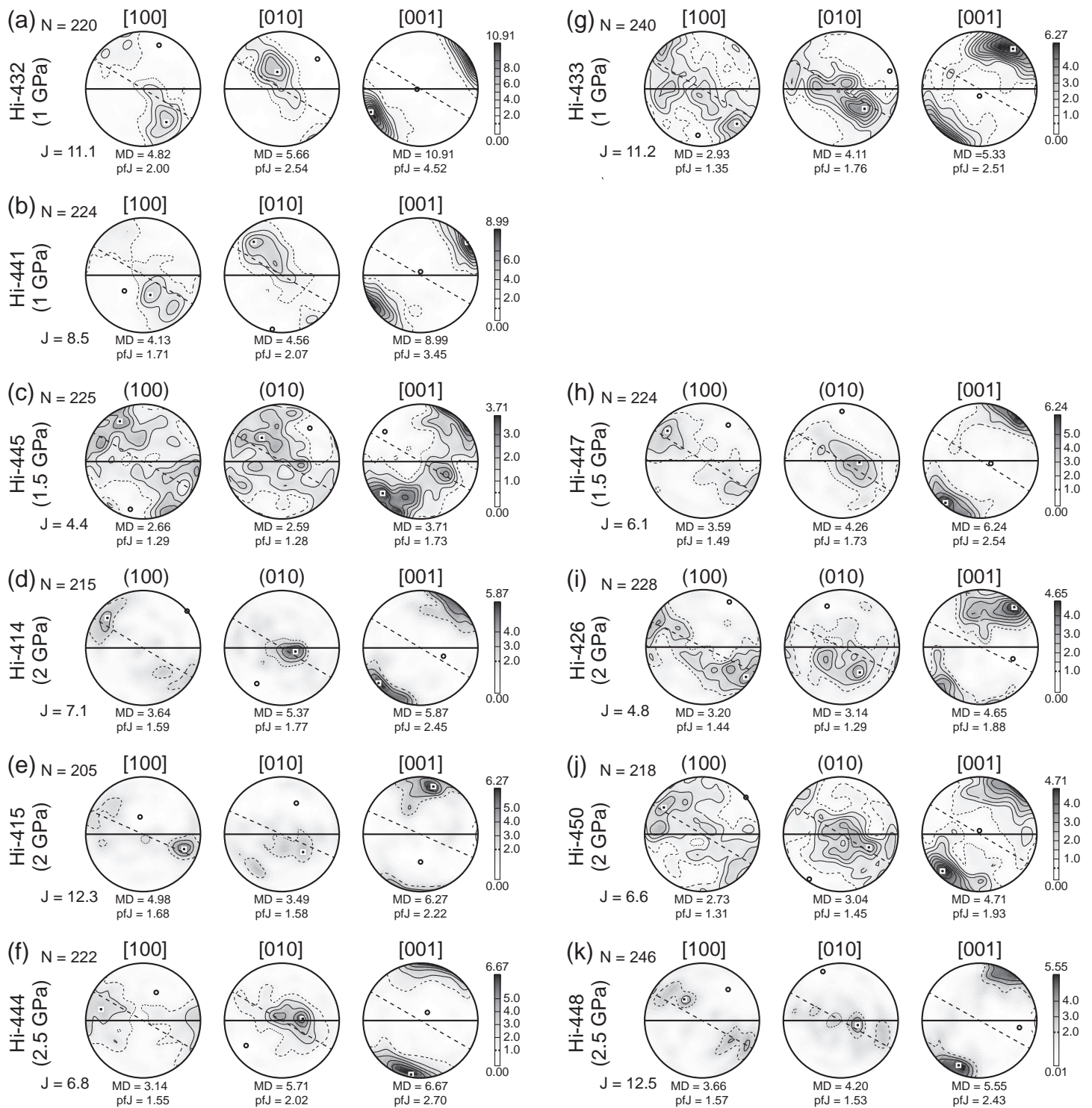
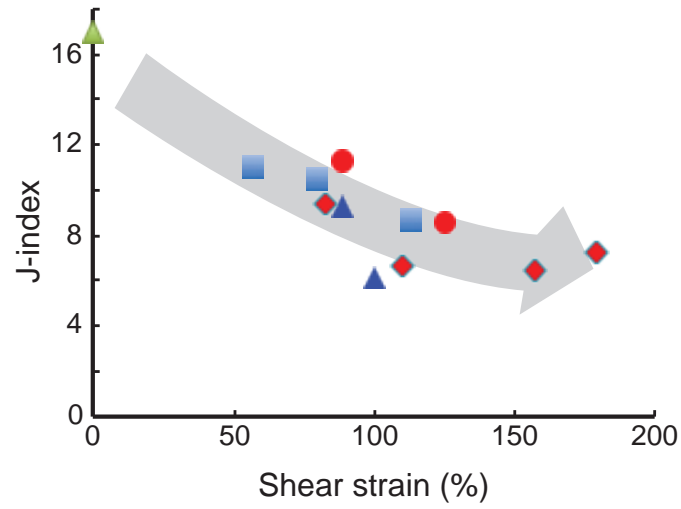


Fig. 4.7. Pole figures of lawsonite in deformed specimens. Contour is depicted for every 1 mean density. N: number of analysis point; J: J -index; MD: mean density; pfJ: J -index of the pole.

a. glaucophane



b. lawsonite

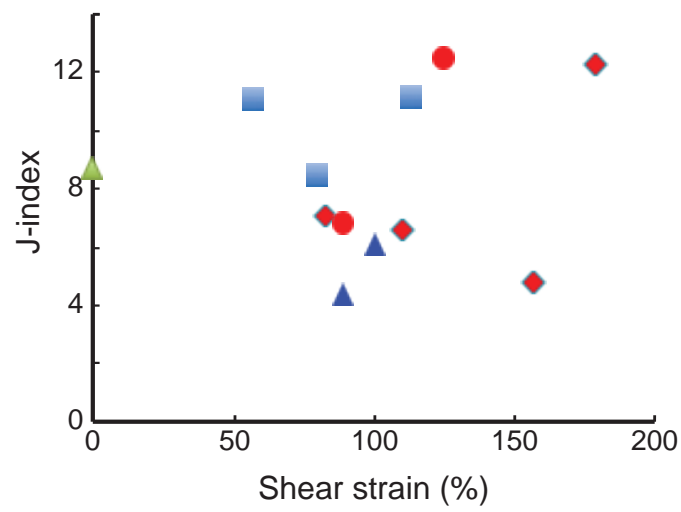
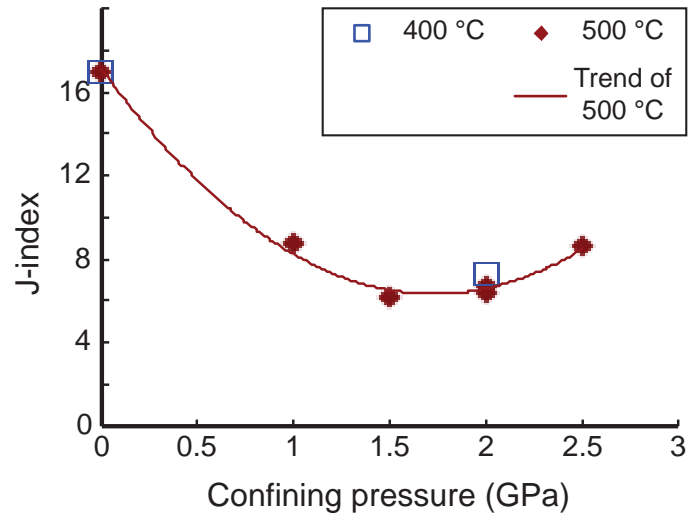


Fig. 4.8. J-index as a function of shear strain for (a) glaucophane and (b) lawsonite.

a. glaucophane



b. lawsonite

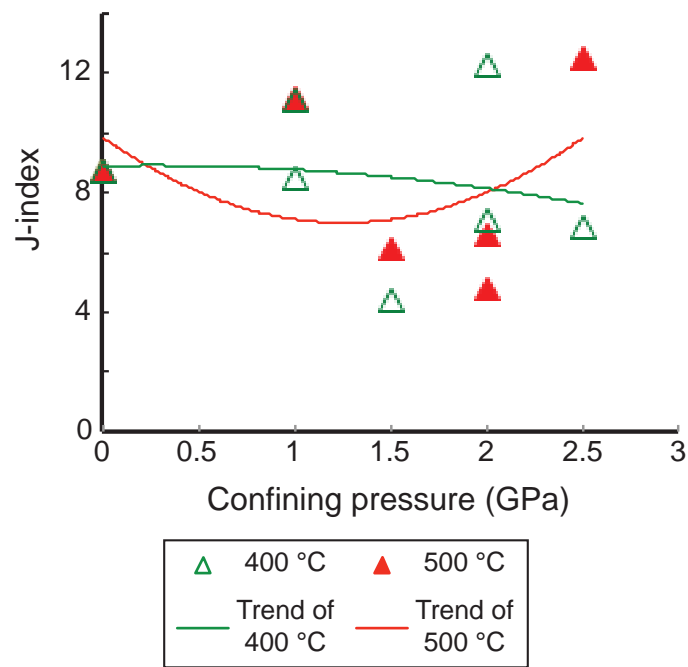


Fig. 4.9. Graphs of J-index and confining pressure for (a) glaucophane and (b) lawsonite.

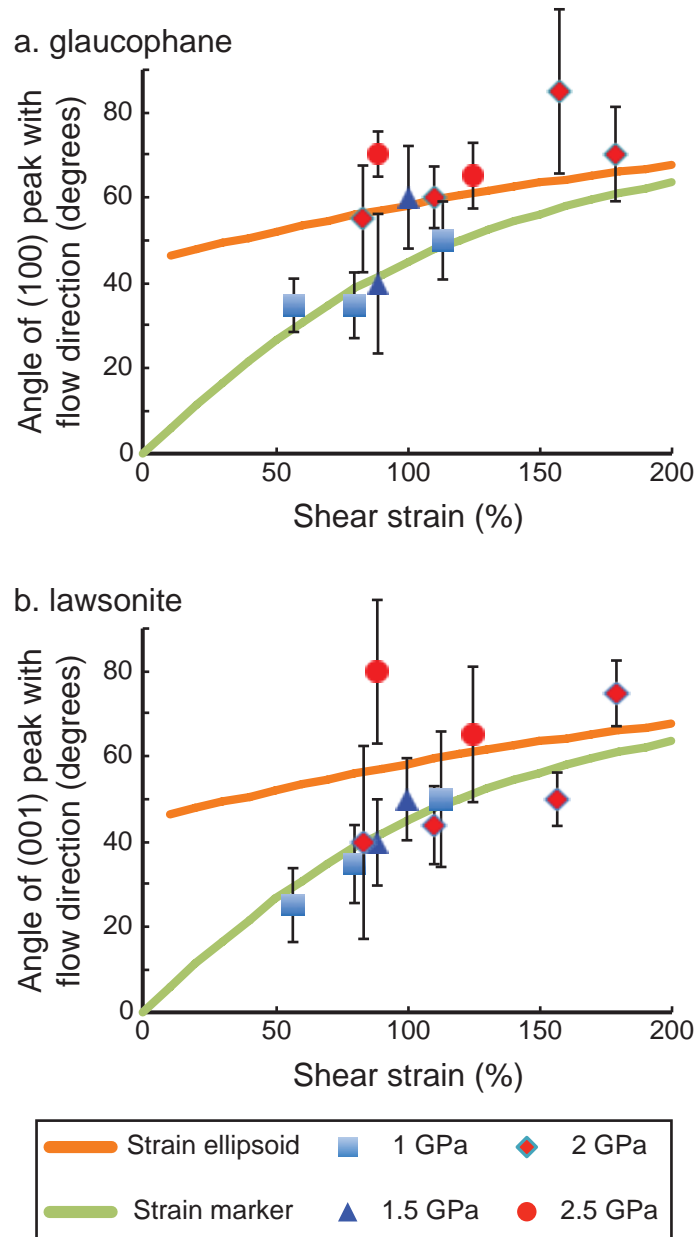
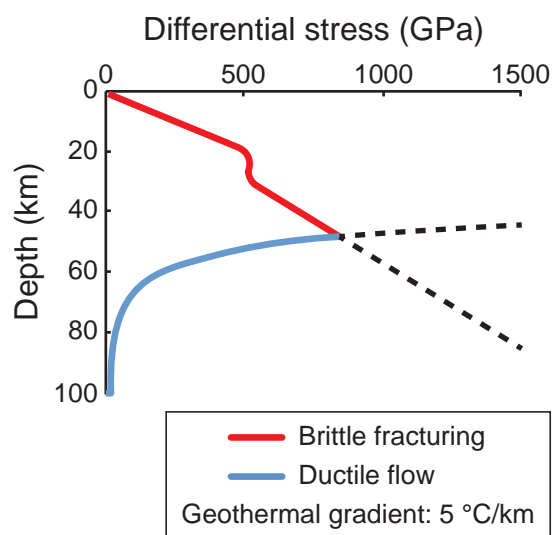


Fig. 4.10. Angle of slip plane to shear direction for (a) glaucophane and (b) lawsonite. Angular changes of strain marker and strain ellipsoid were also plotted. Error range was decided by range of the highest contour in CPO.

a. Dry quartz



b. Dry olivine

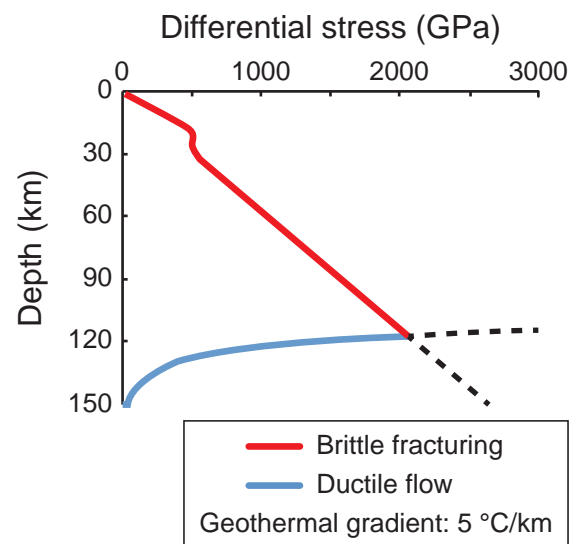


Fig. 4.11. Differential stress–depth diagrams for a. dry quartz and b. dry olivine. Physical parameters were employed from Byerlee (1978) for brittle failure, Gleason and Tullis (1995) for ductile flow of dry quartz, and Karato and Jung (2003) for ductile flow of dry olivine.

NE Japan (old): Glaucophane

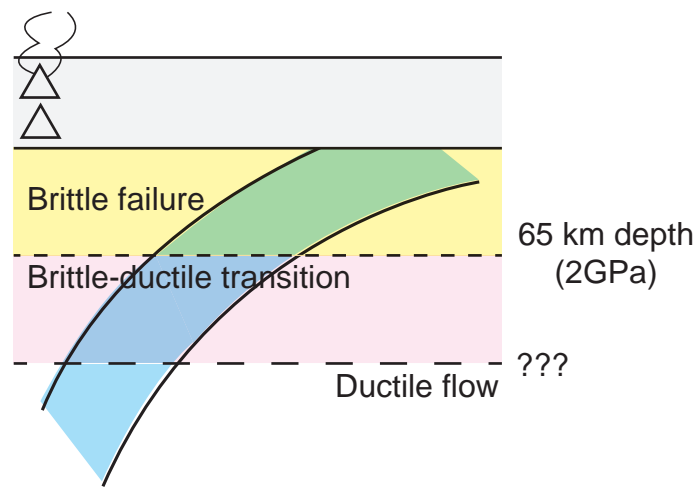


Fig. 4.12. Application of mechanical behaviors of glaucophane a tectonic setting beneath NE Japan. The boundary between brittle failure and brittle-ductile transition was delineated by this study. However, boundary between brittle-ductile transition and ductile flow needs to be investigated by following research.

Table 4.1. Summary of experimental samples

Sample #	T (°C)	P (GPa)	Shear strain	Strain rate	J-indices	
					Gln	Lws
Pure shear experiments						
Hi-462	500	0.5	0.11	1.33×10^{-5}		
Hi-472	500	0.5	0.14	1.33×10^{-5}		
Hi-460	500	1	0.11	1.31×10^{-5}		
Hi-461	500	2	0.13	1.31×10^{-5}		
Simple shear experiments						
Hi-432	400	1.0	0.57±0.04	$5.96 (\pm 0.43) \times 10^{-5}$	11.0	11.1
Hi-441	400	1.0	0.80±0.05	$8.70 (\pm 0.55) \times 10^{-5}$	10.5	8.5
Hi-445	400	1.5	0.89±0.04	$9.08 (\pm 0.41) \times 10^{-5}$	9.3	4.4
Hi-414	400	2.0	0.83±0.02	$1.80 (\pm 0.04) \times 10^{-4}$	9.4	7.1
Hi-415	400	2.0	1.79±0.36	$1.26 (\pm 0.25) \times 10^{-4}$	7.3	12.3
Hi-444	400	2.5	0.89±0.03	$7.95 (\pm 0.27) \times 10^{-5}$	11.3	6.8
Hi-433	500	1.0	1.13±0.06	$1.26 (\pm 0.07) \times 10^{-4}$	8.7	11.2
Hi-447	500	1.5	1.00±0.05	$9.62 (\pm 0.38) \times 10^{-5}$	6.1	6.1
Hi-418	500	2.0	1.36±0.78	$1.38 (\pm 0.50) \times 10^{-4}$		
Hi-426	500	2.0	1.57±0.57	$8.95 (\pm 5.13) \times 10^{-5}$	6.4	4.8
Hi-450	500	2.0	1.10±0.04	$2.70 (\pm 0.10) \times 10^{-5}$	6.7	6.6
Hi-448	500	2.5	1.25±0.03	$1.25 (\pm 0.03) \times 10^{-4}$	8.6	12.5

Table 4.2. Parameters of rheological formulations

Parameter	Symbol	Value	Unit	Source
Crust				
Frictional coefficient	(P<200MPa)	Af	0.85	Byerlee (1978)
	(P>200MPa)	Af	0.6	Byerlee (1978)
Frictional cohesive strength	Cf	50	MPa	Byerlee (1978)
Constant of dislocation creep	A dis	1.1×10^{-4}	$\text{MPa}^{-4}\text{s}^{-1}$	Gleason & Tullis (1995)
Activation energy of dislocation creep	E dis	223	kJ mol^{-1}	Gleason & Tullis (1995)
Stress exponent	n	4		Gleason & Tullis (1995)
Strain rate		10^{-15}	s^{-1}	
Mantle				
Constant of dislocation, dry	A dis, dry	$10^{6.1}$	$\text{s}^{-1}\text{MPa}^{-3}$	Karato and Jung (2003)
Activation energy of dislocation, dry	E dis, dry	510	kJ mol^{-1}	Karato and Jung (2003)
Activation volume of dislocation, dry	V dis, dry	0	$\text{cm}^3 \text{mol}^{-1}$	
Stress exponent	n	3		Karato and Jung (2003)
Strain rate		10^{-15}	s^{-1}	

Chapter V

SUMMARY

By systematic fabric analyses of naturally and experimentally deformed blueschists, deformation behaviors and seismic properties of subducting oceanic crust were delineated. Naturally deformed lawsonite and epidote blueschists show dynamically recrystallized glaucophane characterized by anhedral to subhedral grain shape, strong CPOs, very fine grain size, irregular grain boundary, and high aspect ratio. Angular or straight grain boundary suggests that lawsonite and epidote deform by rigid body rotation. Glaucophane-rich layer and glaucophane have higher aspect ratio, lower angle to foliation, stronger CPOs, and higher seismic anisotropy rather than lawsonite-rich layer and lawsonite or epidote, respectively, indicating the predominant role of glaucophane rather than lawsonite or epidote for rheological behaviors of subducting oceanic crust.

Glaucophane contains the fastest P-wave propagation along the lineation, and the S-wave polarization subparallel to the foliation ($AV_P = 20.4\%$, $AV_S = 11.48\%$), implying possible occurrence of a trench-parallel seismic anisotropy owing to the slowest V_S polarization perpendicular to the subducting slab. Epidote has similar seismic patterns with glaucophane, however strength of anisotropy is relatively weak ($AV_P = 9.0\%$, $AV_S = 8.04\%$). Seismic properties of lawsonite are characterized by the fast p-wave propagation normal to the foliation and S-wave polarization perpendicular to the lineation ($AV_P = 9.6\%$, $AV_S = 19.88\%$), denoting probable development of a trench-normal anisotropy. Combinations of glaucophane and lawsonite or glaucophane and epidote could generate weak trench-parallel seismic

anisotropy beneath NE Japan and relative strong trench-parallel anisotropy beneath Ryukyu arc. In addition, the results demonstrate abrupt change of seismic anisotropy beneath NE Japan by blueschist (glaucofane + lawsonite) in forearc (trench-parallel) and eclogite (lawsonite) in backarc (trench-normal).

Deformation of glaucofane is proceeded by brittle to semi-brittle failure at 1–2.5 GPa and 400–500 °C based on mechanical data of pure-shear experiments, microstructures of simple-shear experiments, and systematic fabric strength and angular change to shear strain and confining pressure in highly deformed specimens. Lawsonite deforms by brittle failure at whole experimental conditions demonstrated by relict minerals in the samples, and weak relation among *J*-index, shear strain, and confining pressure. Although additional experiments at higher pressure are needed to reveal the upper limit of brittle-ductile transition, these results imply brittle or semi-brittle behaviors of glaucofane as a source of observed seismicity in subducting oceanic crust beneath NE Japan.

Chapter VI

ACKNOWLEDGEMENTS

Finally my journey during the PhD course has been successfully finished. When I have met many barriers and discouragement, special friends thankfully encouraged me with high praise. Especially my advisor Dr. Ikuo Katayama always cheered me up and showed me ideal attitudes as a scientist. Without his helps, I could not get a PhD. In addition, I also appreciate Dr. Katsuyoshi Michibayashi at Shizuoka University for hearty welcomes and technical supports at Shizuoka, and Dr. Tatsuki Tsujimori at Okayama University for supplying great and special samples. Most achievements during my PhD course have received dedicate assistants from above three researchers.

I also gratefully acknowledge other faculties at Hiroshima University. Dr. Hiroshi Hidaka, Dr. Kentaro Terada, and Dr. Yasutaka Hayasaka helped me before and after my movement to Japan. Dr. Yoshio Takahashi, Dr. Kenichi Hoshino, Dr. Kaushik Das and Dr. Aya Sakaguchi always cheered me up. Dr. Masato Tanaka, Dr. Fumito Shiraishi, Dr. Tomoko Sato and Dr. Masahiro Kayama showed me good friendships. Especially Dr. Jun-ichi Ando and Dr. Ken-ichi Hirauchi (Now at Shizuoka University) provide their techniques and passions to my works.

Former and present students contributed to my life and study in Japan. I appreciate particularly to Dr. Aya Katsube for a long time and great friendship, Dr. Keishi Okazaki and Shintaro Azuma as office mates for the longest time. Also I would like to be thankful to Dr. Tetsuhiro Togo, Dr. Qiaohui Fan, Dr. Yuka Yokoyama, Kosuke Kimura, Ryoichi Nakada, Michiyo Sawai, Liang Yi, Makiko Kikuchi and Manami Kitamura for their friendships.

In addition, I am appreciative to some researchers in other places. Dr. Luiz F.G. Morales at Helmholtz-Zentrum Potsdam firstly showed me his technique to use PFctf and ANISctf. I would like to express my heartfelt gratitude to Dr. Moon-sup Cho and Dr. Haemyeong Jung at Seoul National University (SNU) for their cheers. Also I specially thank to Dr. Chul Lim (SNU), Dr. Hyeoncheol Kim (KIGAM), Dr. Seung Ryeol Lee (KIGAM), Dr. Jeongmin Kim (KBSI), Dr. Keewook Yi (KBSI), Dr. Jinho, Ahn (SNU), Dr. Taehoon, Kim (KOPRI), Dr. Eun-Seo Choi (Univ. Memphis), Dr. Yoonsup Kim (Chungbuk Nat'l Univ.), Dr. Wonseok Cheong (SNU), Dr. Jung Hun Seo (Inha Univ.), Dr. Heejin Jeon (ANU), Mr. Yuyoung Lee (SNU), Soh-young Yang (SNU), Jun Seok Na (SNU), and Kim TaeHwan (SNU).

Finally I am indebted to my family. My parents always believe me and cheer me up. Two elder sisters and two brothers-in-law helped me in various ways. Especially I like my three nephews (Jongwook, Jongmin, and Takuma) who are always very cute and grown well. I really love my all family.

My living and researches were supported mostly by the Monbu-kagaku-sho scholarship to D. Kim and by the Japan Society for the Promotion of Science (JSPS) to Dr. Ikuo Katayama, respectively.

Chapter VII

REFERENCES

- Aleksandrov, K.S., Alchikov, U.V., Belikov, B.P., Zaslavskii, B.I. and Krupnyi, A.I., 1974. Velocities of elastic waves in minerals at atmospheric pressure and increasing precision of elastic constants by mean of EVM (in Russian). *Bulletin of the Academy of Sciences of the USSR, Geophys. Ser.*, **10**, 15–24.
- Ando, J., Takeshita, T., Matsubara, K., Hayasaka, Y., 2006. Evaluation of fundamental performance of a modified Griggs type apparatus installed at Hiroshima University. *Japanese Journal of Structural Geology*, **49**, 27–39 (in Japanese with English abstract).
- Banno, S., 1958. Glaucophane schists and associated rocks in the Omi district, Niigata Prefecture, Japan. *Japanese Journal of Geology and Geography*, **29**, 29–44.
- Barrie, C.D., Pearce, M.A. and Boyle, A.P., 2011. Reconstructing the pyrite deformation mechanism map. *Ore Geology Reviews*, **39**, 265–276, doi:10.1016/j.oregeorev.2011.03.006.
- Bascou, J., Barruola, G., Vaucheza, A., Mainprice, D. and Egydio-Silva, M., 2001. EBSD-measured lattice-preferred orientations and seismic properties of eclogites. *Tectonophysics*, **342**, 61–80, doi:10.1016/S0040-1951(01)00156-1.
- Berger, A. and Stünitz, H., 1996. Deformation mechanisms and reaction of amphibole: examples from the Bergell tonalite (Centrl Alps). *Tectonophysics*, **257**, 149–174, doi:10.1016/0040-1951(95)00125-5.
- Bezacier, L., Reynard, B., Bass, J.D., Wang, J. and Mainprice, D., 2010. Elasticity of glaucophane, seismic velocities and anisotropy of the subducted oceanic crust.

- Tectonophysics*, **494**, 201–210, doi:10.1016/j.tecto.2010.09.011.
- Bostock, M.G., 2012. The Moho in subduction zones. *Tectonophysics*, in press, doi:10.1016/j.tecto.2012.07.007.
- Brodie, K.H., Rutter, E.H., 1985. On the relationship between deformation and metamorphism, with special reference to the behavior of basic rocks. *Advances in Physical Geochemistry*, **4**, 138–179.
- Bunge, H.J., 1982. Texture Analysis in Materials Science. *Butterworth, London*, pp. 559.
- Byerlee, J., 1978. Friction of rocks. *Pure and Applied Geophysics*, **116**, 615–626, doi:10.1007/BF00876528.
- Cao, Y., Jung, H., Song, S., 2013. Petro-fabrics and seismic properties of blueschist and eclogite in the North Qilian suture zone, NW China: Implications for the low-velocity upper layer in subducting slab, trench-parallel seismic anisotropy and eclogite detectability in the subduction zone. *Journal of Geophysical Research*, **in press**, doi:10.1002/jgrb.50212.
- Carter, N.L. and Avé Lallemant, H.G., 1970. High temperature deformation of dunite and peridotites. *Geological Society of America Bulletin*, **81**, 2181–2202, doi:10.1130/0016-7606(1970)81[2181:HTFODA]2.0.CO;2.
- Chantel, J., Mookherjee, M. and Frost, D.J., 2012. The elasticity of lawsonite at high pressure and the origin of low velocity layers in subduction zones. *Earth and Planetary Science Letters*, **349–350**, 116–125, doi:10.1016/j.epsl.2012.06.034.
- Coleman, R.G., 1980. Tectonic inclusions in serpentinite. *Archives des Sciences, Société de Physique et d'Histoire Naturelle de Genève* **33**, 89–102.
- Coleman, R.G. and Lee D.E., 1963. Ultrahigh-Pressure Metamorphism. *Cambridge*

University Press, New York, pp. 528.

Cumbest, R.J., Drury, M.R., Van Roermund, H.L.M. and Simpson, C., 1989.

Dynamic recrystallization and chemical evolution of clinoamphibole from Senja Norway. *Contributions to Mineralogy and Petrology*, **101**, 339–349, doi:10.1007/BF00375318.

Deer, W.A., Howie, R.A. and Zussman, J., 1992. The rock-forming minerals. *2nd edition, Longmans, London*, pp. 266.

Díaz Aspiroz, M., Lloyd, G.E. and Fernández, C., 2007. Development of lattice preferred orientation in clinoamphiboles deformed under low-pressure metamorphic conditions. A SEM/EBSD study of metabasites from the Aracena metamorphic belt (SW Spain). *Journal of Structural Geology*, **29**, 629–645, doi:10.1016/j.jsg.2006.10.010.

Dollinger, G. and Blacic, J.D., 1975. Deformation mechanisms in experimentally and naturally deformed amphiboles. *Earth and Planetary Science Letters*, **26**, 409–416, doi:10.1016/0012-821X(75)90016-3.

Drury, M.R. and Urai, J.L., 1990. Deformation-related recrystallization processes. *Tectonophysics*, **172**, 235–253, doi:10.1016/0040-1951(90)90033-5.

Ebert, A., Herwegh, M. and Pfiffner, A., 2007. Cooling induced strain localization in carbonate mylonites within a large-scale shear zone (Glarus thrust, Switzerland). *Journal of Structural Geology*, **29**, 1164–1184, doi:10.1016/j.jsg.2007.03.007.

Evans, B., Renner, J. and Hirth, G., 2001. A few remarks on the kinetics of static grain growth in rocks. *International Journal of Earth Sciences*, **90**, 88–103, doi:10.1007/s005310000150.

Fujimoto, Y., Kono, Y., Hirajima, T., Kanagawa, K., Ishikawa, M. and Arima, M.,

2010. P-wave velocity and anisotropy of lawsonite and epidote blueschists: Constraints on water transportation along subducting oceanic crust. *Physics of the Earth and Planetary Interiors*, **183**, 219–228, doi:10.1016/j.pepi.2010.09.003.
- Gleason, G.C. and Tullis, J., 1995. A flow law for dislocation creep of quartz aggregates determined with the molten salt cell. *Tectonophysics*, **247**, 1–25, doi:10.1016/0040-1952(95)00011-B.
- Hacker, B.R. and Christie, J.M., 1990. Brittle/ductile and plastic/cataclastic transitions in experimentally deformed and metamorphosed amphibolite. *Geophysical Monograph*, **56**, 127–147.
- Hacker, B.R., Aber, G.A. and Peacock, S.M., 2003. Subduction factory 1. Theoretical mineralogy, densities, seismic wave speeds, and H₂O contents. *Journal of Geophysical Research*, **108(B1)**, doi:10.1029/2001JB001127.
- Herwegh, M., Berger, A., Ebert, A. and Brodhag, S., 2008. Discrimination of annealed and dynamic fabrics: Consequences for strain localization and deformation episodes of large-scale shear zones. *Earth and Planetary Science Letters*, **276**, 52–61, doi:10.1016/j.epsl/2008.09.007.
- Hippertt, J.F. and Hongn, F.D., 1998. Deformation mechanisms in the mylonite/ultramylonite transition. *Journal of Structural Geology*, **20**, 1435–1448, doi:10.1016/S0191-8141(98)00047-9.
- Huang, X., Bai, W. and Hu, J., 2003. Experimental studies on elastic and rheological properties of amphibolites at high pressure and high temperature. *Science in China*, **46**, 1212–1222, doi:10.1360/02yd0437.
- Ildfonse, B., Lardeauz, J.-M. and Caron, J.-M., 1990. The behavior of shape preferred orientations in metamorphic rocks: amphiboles and jadeites from the

- Monte Mucrone area (Sesia–Lanzo zone, Italian Western Alps). *Journal of Structural Geology*, **12**, 1005–1011, doi:10.1016/0191-8141(90)90096-H.
- Imon, R., Okudaira, T. and Kanagawa, K., 2004. Development of shape- and lattice-preferred orientations of amphibole grains during initial cataclastic deformation and subsequent deformation by dissolution–precipitation creep in amphibolites from the Ryoke metamorphic belt, SW Japan. *Journal of Structural Geology*, **26**, 793–805, doi:10.1016/j.jsg.2003.09.004.
- Ismail, W.B. and Mainprice, D., 1998. An olivine fabric database: an overview of upper mantle fabrics and seismic anisotropy. *Tectonophysics*, **296**, 145–157, doi:10.1016/S0040-1951(98)00141-3.
- Jung, H. and Karato, S.-I., 2001. Water-induced fabric transitions in olivine. *Science*, **293**, 1460–1463, doi:10.1126/science.1062235.
- Jung, H., Katayama, I., Jiang, Z., Hiraga, T. and Karato, S., 2006. Effect of water and stress on the lattice-preferred orientation of olivine. *Tectonophysics*, **421**, 1–22, doi:10.1016/j.tecto.2006.02.011.
- Karato, S.-I. and Jung, H., 2003. Effects of pressure on high-temperature dislocation creep in olivine. *Philosophical Magazine*, **83**, 401–414, doi:10.1080/0141861021000025829.
- Katayama, I., 2009. Thin anisotropic layer in the mantle wedge beneath northeast Japan. *Geology*, **37**, 211–214, doi: 10.1130/G25413A.1.
- Katayama, I. and Karato, S.-I., 2006. Effect of temperature on the B- to C-type olivine fabric transition and implication for flow pattern in the subduction zone. *Physics of the Earth and Planetary Interiors*, **157**, 33–45, doi:10.1016/j.pepi.2006.03.005.

- Katayama, I., Hirauchi, K., Michibayashi, K. and Ando, J., 2009. Trench-parallel anisotropy produced by serpentine deformation in the hydrated mantle wedge. *Nature*, **461**, 1114–1117, doi:10.1038/nature08513.
- Kim, D., Katayama, I., Michibayashi, K., Tsujimori, T. 2013a. Deformation fabrics of natural blueschists and implications for seismic anisotropy in subducting oceanic crust. *Physics of the Earth and Planetary Interiors*, **444**, 8–21, doi:10.1016/j.pepi.2013.06.011.
- Kim, D., Katayama, I., Michibayashi, K., Tsujimori, T. 2013b. Rheological contrast between glaucophane and lawsonite in naturally deformed blueschist from Diablo Range, California. *Island Arc*, **22**, 63–73, doi:10.1111/iar.12003.
- Kita, S., Okada, T., Nakajima, J., Matsuzawa, T. and Hasegawa, A., 2006. Existence of a seismic belt in the upper plane of the double seismic zone extending in the along-arc direction at depths of 70–100 km beneath NE Japan. *Geophysical Research Letters*, **33**, L24310, doi:10.1029/2006GL028239.
- Kohlstedt, D.L., Evans, B. and Mackwell, S.J., 1995. Strength of the lithosphere: Constraints imposed by laboratory experiments. *Journal of Geophysical Research*, **100**, 17587–17602, doi: 10.1029/95JB01460.
- Leake, B.E., Woolley, A.R., Arps, C.E.S., Birch, W.D., Gilbert, M.C., Grice, J.D., Hawthorne, F.D., Kato, A., Kisch, H.J., Krivovichev, V.G., Linthout, K., Laird, J., Mandarino, J.A., Maresch, W.V., Nickel, E.H., Rock, N.M.S., Schumacher, J.C., Smith, D.C., Stephenson, N.C.N., Ungaretti, L., Whittaker, E.J.W. and Youzhi, G., 1997. Nomenclature of amphiboles; Report of the Subcommittee on Amphiboles of the International Mineralogical Association, Commission on New Minerals and Mineral Names. *Canadian Mineralogist*, **35**, 219–246, doi:10.2113/gscanmin.41.6.1355.

- Long, D.L. and van der Hilst, R.D., 2005. Upper mantle anisotropy beneath Japan from shear wave splitting. *Physics of the Earth and Planetary Interiors*, **151**, 206–222, doi:10.1016/j.pepi.2005.03.003.
- Long, M.D. and Silver, P.G., 2008. The subduction zone flow field from seismic anisotropy: A global view, *Science*, **319**, 315–318, doi:10.1126/science.1150809.
- Mainprice, D., 1990. An efficient Fortran program to calculate seismic anisotropy from the lattice preferred orientation of minerals. *Computers & Geosciences*, **16**, 385–393, doi:10.1016/0098-3004(90)90072-2.
- Mainprice, D. and Silver, P.G., 1993. Interpretation of SKS-waves using samples from the subcontinental lithosphere, *Physics of the Earth and Planetary Interiors*, **78**, 257–280, doi:10.1016/0031-9201(93)90160-B.
- Mainprice, D., Barruol, G. and Ben Ismaïl, W., 2000. The anisotropy of the Earth's mantle: From single crystal to polycrystal. In Karato S., Forte A.M., Liebermann R.C., Masters G., Stixrude, L. (eds.), *Mineral Physics and Seismic Tomography: From Atomic to Global*, *AGU Geophysical Monograph*, **117**, 237–264, doi:10.1029/GM117p0237.
- Mao, Z., Jiang, F. and Duffy, T.S., 2007. Single-crystal elasticity of zoisite $\text{Ca}_2\text{Al}_3\text{Si}_3\text{O}_{12}(\text{OH})$ by Brillouin scattering. *American Mineralogist*, **92**, 570–576, doi: 10.2138/am.2007.2329.
- Maruyama, S., Cho, M. and Liou, J.G., 1986. Experimental investigations of blueschist–greenschist transition equilibria: Pressure dependence of Al_2O_3 contents in sodic amphiboles — A new barometer. In Evans B.W., Brown E.H. (eds.), *Blueschist and Eclogite*, *Geological Society of America Memoir*, **164**, 1–16.

- Maruyama, S. and Liou, J.G., 1987. Clinopyroxene a mineral telescoped through the processes of blueschist facies metamorphism. *Journal of Metamorphic Geology*, **5**, 529–552, DOI: 10.1111/j.1525-1314.1987.tb00400.x.
- Maruyama, S. and Liou, J.G., 1988. Petrology of Franciscan metabasites along the jadeite–glaucofane type facies series, Cazadero, California. *Journal of Petrology*, **29**, 1–37, doi:10.1093/petrology/29.1.1.
- Mezger, J.E., 2010. Rotation of irregular staurolite porphyroblasts in a simple shear dominated shear zone controlled by initial growth orientation and aspect ratio. *Journal of Structural Geology*, **32**, 1147–1157, doi:10.1016/j.jsg.2010.07.002.
- Mookherjee, M. and Bezacier, L., 2012. The low velocity layer in subduction zone: Structure and elasticity of glaucofane at high pressures. *Physics of the Earth and Planetary Interiors*, **208–209**, 50–58, doi:10.1016/j.pepi.2012.07.007.
- Nakajima, J. and Hasegawa, A., 2004. Shear-wave polarization anisotropy and subduction induced flow in the mantle wedge of northeastern Japan. *Earth and Planetary Science Letters*, **225**, 365–377. doi:10.1016/j.epsl.2004.06.011.
- Nikulin, A., Levin, V. and Park, J., 2009. Receiver function study of the Cascadia megathrust: Evidence for localized serpentinization. *Geochemistry Geophysics Geosystems*, **10**, Q07004, doi:10.1029/2009GC002376.
- Nyman, M.W., Law, R.D. and Smelik, E., 1992. Cataclastic deformation for the development of core mantle structures in amphibole. *Geology*, **20**, 455–458, doi:10.1130/0091-7613(1992)020<0455:CDMFTD>2.3.CO;2.
- Peacock, S.M., 1993. The importance of blueschist → eclogite dehydration reactions in subducting oceanic crust. *Geological Society of America Bulletin*, **105**, 684–694, doi:10.1130/0016-7606(1993)105<0684:TIOBED>2.3.CO;2.

- Peacock, S.M. and Wang, K., 1999. Seismic consequences of warm versus cool subduction metamorphism: Examples from Southwest and Northeast Japan. *Science*, **286**, 937–939, doi:10.1126/science.286.5441.937.
- Prior, D.J., Boyle, A.P., Brenker, F., Cheadle, M.C., Day, A., Lopez, G., Peruzzo, L., Potts, G.J., Reddy, S., Spiess, R., Timms, N.E., Trimby, P., Wheeler, J. and Zetterstrom, L., 1999. The application of electron backscatter diffraction and orientation contrast imaging in the SEM to textural problems in rocks. *American Mineralogist*, **84**, 1741–1759.
- Randle, V., 1992. Microtexture Determination and its Applications. *The Institute of Materials, Minerals and Mining, London*, pp. 174.
- Randle, V. and Engler, O., 2000. Introduction to Texture Analysis: Macrotexture, Microtexture and Orientation Mapping. *CRC Press, London*, pp. 408.
- Reynard, B., Gillet, P. and Willaime, C., 1989. Deformation mechanisms in naturally deformed glaucophanes: A TEM and HREM study. *European Journal of Mineralogy*, **1**, 611–624.
- Rooney, T.P., Riecker, R.E. and Ross, M., 1970. Deformation twins in hornblende. *Science*, **169**, 173–175, doi:10.1126/science.169.3941.173.
- Rooney, T.P., Riecker, R.E. and Gavasci, A.T., 1975. Hornblende deformation features. *Geology*, **3**, 364–366, doi:10.1130/0091-7613(1975)3<364:HDF>2.0.CO;2.
- Satsukawa, T., Michibayashi, K., Anthony, E.Y., Stern, R.J., Gao, S.S. and Liu, K.H., 2011. Seismic anisotropy of the uppermost mantle beneath the Rio Grande rift: Evidence from Kilbourne Hole peridotite xenoliths, New Mexico. *Earth and Planetary Science Letters*, **311**, 172–181. doi:10.1016/j.epsl.2011.09.013.
- Schmidt, M.W. and Poli, S., 1998. Experimentally based water budgets for

- dehydrating slab and consequences for arc magma generation. *Earth and Planetary Science Letters*, **163**, 361–379, doi:10.1016/S0012-821X(98)00142-3.
- Shelly, D.R., Beroza, G.C., Ide, S. and Nakamura, S., 2006. Low-frequency earthquake in Shikoku, Japan, and their relationship to episodic tremor and slip. *Nature*, **422**, 188–191, doi:10.1038/nature04931.
- Siegesmund, S., Helming, K. and Kruse, R., 1994. Complete texture analysis of a deformed amphibolite: comparison between neutron, diffraction and U-stage data. *Journal of Structural Geology*, **16**, 131–142, doi:10.1016/0191-8141(94)90024-8.
- Sinogeikin, S.V. and Bass, J.D., 2000. Single-crystal elasticity of pyrope and MgO to 20 GPa by Brillouin scattering in the diamond cell. *Physics of the Earth and Planetary Interiors*, **120**, 43–62, doi:10.1016/S0031-9201(00)00143-6.
- Sinogeikin, S.V., Schilling, F.R. and Bass, J.D., 2000. Single crystal elasticity of lawsonite. *American Mineralogist*, **85**, 1834–1837, doi:10.1016/S0031-9201(00)00143-6.
- Skemer, P., Katayama, I., Jiang, Z. and Karato, S., 2005. The misorientation index: Development of a new method for calculating the strength of lattice-preferred orientation. *Tectonophysics*, **411**, 157–167, doi:10.1016/j.tecto.2005.08.023.
- Syracuse, E.M., van Keken, P.E. and Abers, G.A., 2010. The global range of subduction zone thermal models. *Physics of the Earth and Planetary Interiors*, **183**, 73–90, doi.org/10.1016/j.pepi.2010.02.004.
- Teyssier, C., Whitney, D.L., Toraman, E. and Seaton, N.C.A., 2010. Lawsonite vorticity and subduction kinematics. *Geology*, **38**, 1123–1126, doi:10.1130/G31409.1.
- Tsuji, Y., Nakajima, J. and Hasegawa, A., 2008. Tomographic evidence for hydrated

- oceanic crust of the Pacific slab beneath northeastern Japan: implications for water transportation in subduction zones. *Geophysical Research Letters*, **35**, L14308, DOI: 10.1029/2008GL034461.
- Tsujimori, T., 2002. Prograde and retrograde P–T paths of the Late Paleozoic glaucophane eclogite from the Renge Metamorphic Belt, Hida Mountains, Southwestern Japan. *International Geology Review*, **44**, 797–818, doi:10.2747/0020-6814.44.9.797.
- Tsujimori, T., Ishiwatari, A. and Banno, S., 2000. Eclogitic glaucophane schist from the Yunotani valley in Omi Town, the Renge metamorphic belt, the Inner Zone of southwestern Japan. *Journal of Geological Society of Japan*, **106**, 353–362 (in Japanese with English abstract).
- Tsujimori, T., Sisson, V.B., Liou, J.G., Harlow, G.E. and Sorensen, S.S., 2006. Very-low-temperature record in subduction process: A review of worldwide lawsonite eclogites. *Lithos*, **92**, 609–624, doi:10.1016/j.lithos.2006.03.054.
- Tsujimori, T., Liou, G.J. and Coleman, R.G., 2007. Finding of high-grade tectonic blocks from the New Idria serpentinite body, Diablo Range, California: Petrologic constraints on the tectonic evolution of an active serpentinite diapir. In Cloos, M., Carlson, W.D., Gilbert, M.C., Liou, J.G., Sorensen, S.S. (Eds.), *Convergent margin terranes and associated regions: A tribute to Ernst, W.G.*, *Geological Society of America Special Papers*, **419**, 67–80, doi:10.1130/2007.2419(03).
- Vernooij, M.G.C., Kunze, K., den Brok, B., 2006. ‘Brittle’ shear zones in experimentally deformed quartz single crystals. *Journal of Structural Geology*, **28**, 1292–1306, doi:10.1016/j.jsg.2006.03018.
- White, R.S., McKenzie, D. and O’Nions, R.K., 1992. Oceanic crustal thickness from

- seismic measurements and rare earth element inversions. *Journal of Geophysical Research*, **97**, 19683–19715, doi:10.1029/92JB01749.
- Whitney, D.L. and Evans, B.W., 2010. Abbreviations for names of rock-forming minerals. *American Mineralogist*, **95**, 185–187, doi:10.2138/am.2010.3371.
- Wines, D.A., Conder, J.A. and Faul, U.J., 2008. The seismic structure and dynamics of the mantle wedge. *Annual Review of Earth and Planetary Sciences*, **36**, 421–455, DOI: 10.1146/annurev.earth.33.092203.122633.
- Wirth, E.A. and Long, M.D., 2012. Multiple layers of seismic anisotropy and a low-velocity region in the mantle wedge beneath Japan: Evidence from teleseismic receiver functions. *Geochemistry Geophysics Geosystems*, in press, doi:10.1029/2012GC004180.
- Zhang, S., Karato, S.-I., 1995. Lattice preferred orientation of olivine aggregates deformed in simple shear. *Nature*, **375**, 774–777, doi:10.1038/375774a0.
- Zucali, M., Chateigner, D., Dugnani, M., Lutterotti, L. and Ouladdiaf, B., 2002. Quantitative texture analysis of glaucophanite deformed under eclogite facies conditions (Sesia–Lanzo Zone, Western Alps): Comparison between X-ray and neutron diffraction analysis. *Geological Society, London Special Publication*, **200**, 239–253, doi:10.1144/GSL.SP.2001.01.14.

Published papers

- (1) Kim, D., Katayama, I., Michibayashi, K., Tsujimori, T. 2013a. Deformation fabrics of natural blueschists and implications for seismic anisotropy in subducting oceanic crust. *Physics of the Earth and Planetary Interiors*, **444**, 8–21, doi:10.1016/j.pepi.2013.06.011.
- (2) Kim, D., Katayama, I., Michibayashi, K., Tsujimori, T. 2013b. Rheological contrast between glaucophane and lawsonite in naturally deformed blueschist from Diablo Range, California. *Island Arc*, **22**, 63–73, doi:10.1111/iar.12003.



Deformation fabrics of natural blueschists and implications for seismic anisotropy in subducting oceanic crust



Daeyeong Kim ^{a,*}, Ikuo Katayama ^a, Katsuyoshi Michibayashi ^b, Tatsuki Tsujimori ^c

^a Department of Earth and Planetary Systems Science, Graduate School of Science, Hiroshima University, Higashi-Hiroshima 739-8526, Japan

^b Institute of Geosciences, Shizuoka University, Shizuoka 422-8529, Japan

^c Pheasant Memorial Laboratory, Institute for Study of the Earth's Interior, Okayama University, Misasa, Tottori 682-0193, Japan

ARTICLE INFO

Article history:

Received 25 December 2012

Received in revised form 17 June 2013

Accepted 25 June 2013

Available online 9 July 2013

Edited by K. Hirose

Keywords:

Fabric analyses

Crystal preferred orientations

Seismic anisotropies

Subducting oceanic crust

Blueschist

ABSTRACT

Investigations of microstructures are crucial if we are to understand the seismic anisotropy of subducting oceanic crust, and here we report on our systematic fabric analyses of glaucophane, lawsonite, and epidote in naturally deformed blueschists from the Diablo Range and Franciscan Complex in California, and the Hida Mountains in Japan. Glaucophanes in the analyzed samples consist of very fine grains that are well aligned along the foliation and have high aspect ratios and strong crystal preferred orientations (CPOs) characterized by a (100)[001] pattern. These characteristics, together with a bimodal distribution of grain sizes from some samples, possibly indicate the occurrence of dynamic recrystallization for glaucophane. Although lawsonite and epidote display high aspect ratios and a strong CPO of (001)[010], the occurrence of straight grain boundaries and euhedral crystals indicates that rigid body rotation was the dominant deformation mechanism. The P-wave (AV_P) and S-wave (AV_S) seismic anisotropies of glaucophane ($AV_P = 20.4\%$, $AV_S = 11.5\%$) and epidote ($AV_P = 9.0\%$, $AV_S = 8.0\%$) are typical of the crust; consequently, the fastest propagation of P-waves is parallel to the [001] maxima, and the polarization of S-waves parallel to the foliation can form a trench-parallel seismic anisotropy owing to the slowest V_S polarization being normal to the subducting slab. The seismic anisotropy of lawsonite ($AV_P = 9.6\%$, $AV_S = 19.9\%$) is characterized by the fast propagation of P-waves subnormal to the lawsonite [001] maxima and polarization of S-waves perpendicular to the foliation and lineation, which can generate a trench-normal anisotropy. The AV_S of lawsonite blueschist (5.6–9.2%) is weak compared with that of epidote blueschist (8.4–11.1%). Calculations of the thickness of the anisotropic layer indicate that glaucophane and lawsonite contribute to the trench-parallel and trench-normal seismic anisotropy beneath NE Japan, but not to that beneath the Ryukyu arc. Our results demonstrate, therefore, that lawsonite has a strong influence on seismic velocities in the oceanic crust, and that lawsonite might be the cause of complex anisotropic patterns in subduction zones.

© 2013 Elsevier B.V. All rights reserved.

1. Introduction

The propagation of seismic waves is a powerful tool for understanding the rheological behavior of the Earth at depth. In subduction zones, seismic properties can provide information about the origin of the slab, the nature of the mantle wedge, slab rollback, and help us to understand back-arc spreading and to detect the presence of melts (e.g., Wines et al., 2008). In particular, trench-parallel and trench-perpendicular shear-waves are observed in subduction zones from the polarization directions of fast propagations and the delay time between the arrivals of fast and slow shear-waves. These shear waves have been explained by theories that involve the flow of the mantle (Long and Silver, 2008) or the

crystal preferred orientations (CPOs) of minerals such as olivine (Jung and Karato, 2001) and serpentine (Katayama et al., 2009). The precise source of the seismic anisotropy in subduction zones, however, is not well defined by the shear-wave splitting method, and further studies of the mantle wedge and the subducting slab are therefore essential. In addition, recent studies have emphasized the importance of minerals such as glaucophane and lawsonite in blueschists for explaining the low velocity layer (LVL) (Chantel et al., 2012; Mookherjee and Bezacier, 2012).

The decrease of seismicity in the upper seismic zone of subducting oceanic crust might be related to a change in rock type from blueschist to eclogite (Kita et al., 2006), signifying the importance of rock-forming minerals in explaining the seismic properties. Glaucophane, lawsonite, and epidote are characterized by high water contents (~2.0–2.5 wt% for glaucophane, 1.0–11.5 wt% for lawsonite, and 1.95 wt% for epidote) and strong P-wave (AV_P) and

* Corresponding author. Tel.: +81 80 1635 5435.

E-mail address: daeyeongkim@hiroshima-u.ac.jp (D. Kim).

S-wave (AV_S) seismic anisotropies in single crystals ($AV_P = 38.1\%$ and $AV_S = 27.3\%$ for glaucophane, $AV_P = 74\%$ for lawsonite, and $AV_S = 21\%$ for epidote; Schmidt and Poli, 1998; Sinogeikin et al., 2000; Mao et al., 2007; Bezacier et al., 2010). In addition, previous studies have noted variations in seismic anisotropy, possibly caused by glaucophane CPOs in combination with a diverse range of lawsonite and epidote CPOs (Bezacier et al., 2010; Fujimoto et al., 2010; Teyssier et al., 2010).

In this paper we record the results of fabric analyses of several lawsonite and epidote blueschists from the New Idria serpentinite body of the Diablo Range and Ward Creek, Cazadero, California, USA, and the Omi serpentinite mélange of the Hida Mountains in Japan. We have assessed the deformational behavior of glaucophane, lawsonite, epidote, and the blueschists on the basis of microstructures, aspect ratios, and CPOs relative to foliation, and their seismic properties have been calculated. Additionally, we discuss the tectonic implications of these three minerals with respect to seismic velocities and anisotropic patterns in a subduction zone.

2. Sample localities

2.1. The New Idria serpentinite body, Diablo Range, California

Located between the San Andreas Fault on the west and the San Joaquin Valley on the east, the New Idria serpentinite body in the Diablo Range is exposed along the crest of the Coalanga anticline, and is enclosed by high-angle normal faults that denote the exhumed trace of the Coast Range Fault (Coleman, 1980). The New Idria serpentinite is primarily chrysotile–lizardite, with minor antigorite serpentinite, and it represents the retrogression of a moderately depleted harzburgite that contained numerous tectonic blocks of greenstone and low-grade blueschists (Coleman, 1980; Tsujimori et al., 2007). A sample of highly deformed lawsonite blueschist (sample NI-01) was collected at a nearby eclogite locality where retrograde eclogite and garnet amphibolite, originating from mantle depths, are exposed along Clear Creek (Table 1) (Tsujimori et al., 2007; Kim et al., 2013). The data in this paper on the rheological contrasts of glaucophane and lawsonite have already been reported (Kim et al., 2013). We found it necessary to use these same data in this paper for our calculations of seismic anisotropies of the subducting oceanic crust, because such highly foliated lawsonite blueschists occur very rarely.

2.2. The Ward Creek schist, Franciscan Complex, California

The Ward Creek schist, represented by metamorphosed oceanic basalts and overlying pelagic sediments, occurs within the Franciscan Complex in the central belt of the northern Coast Ranges of California, and lies within type-III blueschists (Coleman and Lee, 1963; Maruyama and Liou, 1987, 1988). The type-III rocks are characterized by a well-developed schistosity, a fine grain size, and a banded structure with layers composed mainly of metamorphosed basalts, cherts, shales, ironstones, and carbonates. We selected and collected a highly foliated garnet-bearing blueschist (CZ-02) close to the lawsonite eclogite locality (Table 1) (Tsujimori et al., 2006).

2.3. The Omi serpentinite mélange, Hida Mountains, Japan

The Renge schist, an older geotectonic unit in the Sangun metamorphic belt, considered to be one of the higher-pressure schists in Japan, mainly comprises metasediments such as pelitic, psammitic and siliceous schists, and metabasites with minor metagabbro. The glaucophane schist in the Omi area, located at the northern end of the Hida Mountains, occurs in the southern chlorite zone of the Renge schist (Banno, 1958; Tsujimori et al., 2000). The glaucophane-bearing metabasites are locally intercalated with micaceous schist in a fault-bounded eclogitic unit that corresponds to the southern chlorite zone. The analyzed samples (Omi-02 and 03) were collected in areas of garnet glaucophane schist and epidote glaucophane schist (Table 1).

3. Analytical techniques

The chemical compositions of the amphiboles were determined by electron probe microanalysis (EPMA, JEOL JXA-8200) at Hiroshima University, Japan. The analytical conditions were as follows: accelerating voltage of 15 kV, beam current of 10 nA, and spot size of 3–5 μm with $K\alpha$ lines for Si, Ti, Al, Cr, Fe, Mn, Mg, Ca, Na, and K. The Fe^{3+} contents in the amphiboles were calculated as the average of the maximum and minimum estimates based on a total of 13 cations for T and C sites and 15 cations for T, C, and B sites (Leake et al., 1997).

Image analyses in sections parallel to the lineation and normal to the foliation were made in order to quantify the aspect ratios of mineral grains, and to determine the angles between the longest

Table 1
Sample locations and the results of fabric analysis.

Sample numbers	Location (latitude, longitude)	Lithology	Mode* (%)	Minerals	Grain size with std. dev. (μm)	Aspect ratio with std. dev.	Fabric strength (CPO)		Seismic anisotropy (%)	
							Number	J	AV_P	AV_S
GRL_NI-01	36°38', –120°71'	Lawsonite blueschist	Gln89, Lws8	Gln	7 ± 3	12.8 ± 6.4	218	18.0	25.3	13.9
					Lws	18 ± 6	5.0 ± 2.3	220	9.6	10.7
LRL_NI-01	36°38', –120°71'	Lawsonite blueschist	Gln64, Lws21	Gln	12 ± 5	6.0 ± 2.8	220	16.0	20.2	9.9
					Lws	20 ± 8	3.6 ± 1.5	219	7.8	8.8
CZ-02	36°54', –123°11'	Grt-bearing lawsonite blueschist	Gln81, Cpx8, Grt4	Gln	59 ± 29	5.2 ± 2.3	253	9.8	17.7	8.4
Omi-02	36°85', 137°74'	Grt-bearing epidote blueschist	Gln54, Ep27, Ttn10, Grt5	Gln	18 ± 7	3.0 ± 1.4	261	9.0	19.5	10.4
					Ep	18 ± 7	2.1 ± 0.6	241	7.2	7.1
GRL_Omi-03	36°81', 137°74'	Epidote blueschist	Gln91, Ep6	Gln	6 ± 3	3.5 ± 1.6	260	32.5	29.5	18.4
					Ep	10 ± 6	3.4 ± 1.4	231	12.5	11.1
ERL_Omi-03	36°81', 137°75'	Epidote blueschist	Ep57, Gln20, Ph19	Gln	9 ± 6	3.0 ± 1.6	247	19.2	27.5	16.6
					Ep	17 ± 10	2.8 ± 1.1	248	8.8	9.7

Mode* excludes phengite, titanite and apatite (abundances of each mineral are less than 5%). Gln: glaucophane; Lws: lawsonite, Cpx: clinopyroxene; Grt: garnet; Ttn: titanite; Ep: epidote; Ph: phengite; Number: number of measurements; J: J-index, respectively.

axes of various grains and the foliation. After tracing grain boundaries, best-fit ellipses (calculated using ImageJ 1.44) were adopted to reduce the complexity of the various shapes of grains (e.g., Mezer, 2010; Kim et al., 2013). Grain sizes were calculated as the area of a square with the same internal area as the calculated best-fit ellipse.

Crystallographic preferred orientations of glaucophane, lawsonite, and epidote were measured by indexation of electron back-scattered diffraction (EBSD) patterns (Randle, 1992; Prior et al., 1999; Randle and Engler, 2000) using an Oxford–HKL–EBSD on a Hitachi S-3400 scanning electron microscope (SEM) at Shizuoka University, Japan. The CPO measurements were conducted with an accelerating voltage of 20 kV, a working distance of 28 mm, and a beam current of ca. 10 nA. Automatic mapping of each sample (1 μm step size) was performed to examine the chemical zoning in glaucophane, lawsonite, and epidote. After we confirmed that an identical lattice orientation accompanied the chemical variations, the EBSD patterns were manually indexed by considering single individual points for each grain. The number of analysis points was standardized at 240 ± 22 to ensure the reliability of data and to allow for comparison among samples. Pole figures were plotted using the software PFch5 written by D. Mainprice, and the fabric strength was determined by the *J*-index (Bunge, 1982; Mainprice and Silver, 1993).

The seismic properties of glaucophane, lawsonite, epidote, and whole rocks made up of those minerals were calculated in order to understand their influence on the seismic properties of the subducting oceanic crust. The P-wave seismic anisotropy (AV_p) is normally described as the difference between the maximum and minimum velocities in two dissimilar propagating paths, and ex-

pressed as a percentage. For example, the $AV_{p_{\text{max}}}$ can be estimated by using the formula $200 (V_{p_{\text{max}}} - V_{p_{\text{min}}}) / (V_{p_{\text{max}}} + V_{p_{\text{min}}})$. The S-wave seismic anisotropy (AV_s) is defined as the difference between two dissimilar velocities of two orthogonally polarized S-waves individually propagating through an anisotropic medium. Hence, the percentage $AV_{s_{\text{max}}}$ is evaluated using the formula $200 (V_{s1} - V_{s2}) / (V_{s1} + V_{s2})$, in which V_{s1} and V_{s2} are the fast and slow velocities, respectively. In this study, the calculations of whole rock seismic properties were made with reference to the modal abundances of each mineral (Table 1) (Mainprice, 1990; Mainprice et al., 2000). We employed the respective single crystal elastic constants (C_{ij}) of glaucophane (Bezacier et al., 2010), lawsonite (Sino-geikin et al., 2000), and epidote (Aleksandrov et al., 1974), and their densities with the Voigt–Reuss–Hill averaging scheme.

4. Description of microstructures and chemical compositions of amphibole

The sample from the New Idria serpentinite body is a fine-grained blueschist mostly composed of glaucophane, lawsonite, titanite, and phengite. It contains two distinct layers: (i) glaucophane-rich layers (GRL NI-01) and (ii) lawsonite-rich layers (LRL NI-01) (Figs. 1a, b and 2a, b; Table 1). Very fine-grained GRL NI-01 shows highly foliated microstructures with low contents of phengite. Anhedral glaucophane has grain size ranging from ~ 1 to $\sim 15 \mu\text{m}$, irregular grain boundaries, and undulose extinction. Lawsonite is subhedral or euhedral and displays small grain size between ~ 10 and $\sim 30 \mu\text{m}$. Relatively fine-grained LRL NI-01 is characterized by relatively large grains of lawsonite with significant amounts of phengite around them (Figs. 1b and 2b). Intersti-

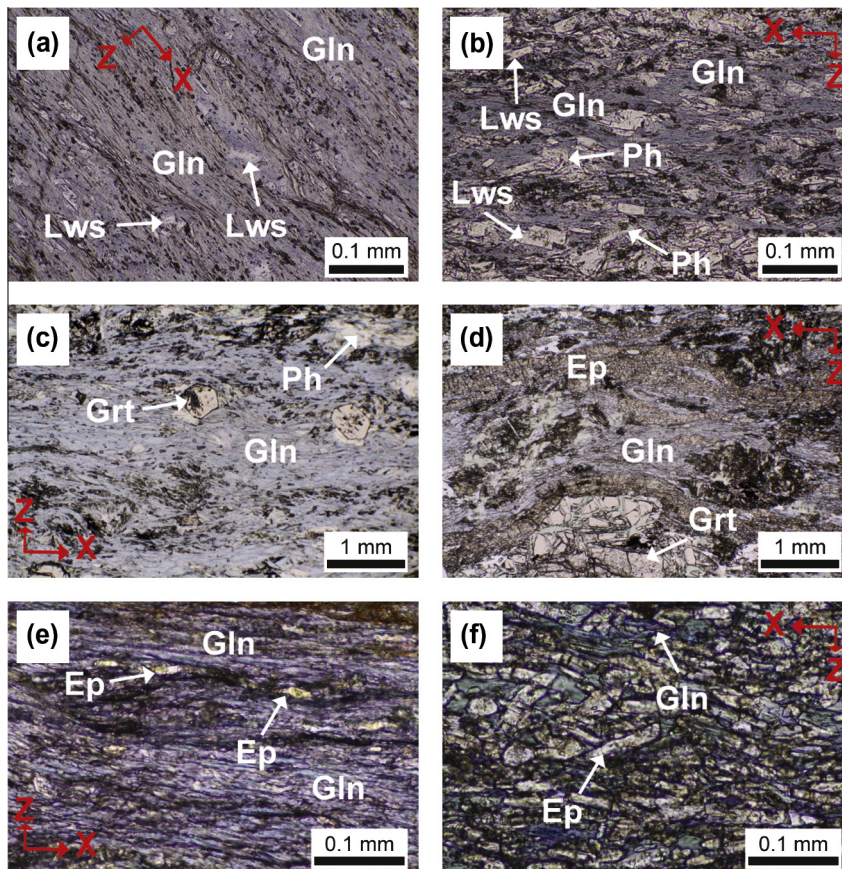


Fig. 1. Photomicrographs of the analyzed samples (XZ sections). (a) Glaucophane-rich and (b) lawsonite-rich layers in NI-01 collected from the New Idria serpentinite body, Diablo Range, California. (c) CZ-02 from Ward Creek, Franciscan Complex, California. (d) Omi-02 and (e) glaucophane-rich and (f) epidote-rich layers in Omi-03 from the Omi serpentinite mélange, Hida Mountains, Japan. See Table 1 for sample locations. Mineral abbreviations follow those in Whitely and Evans (2010).

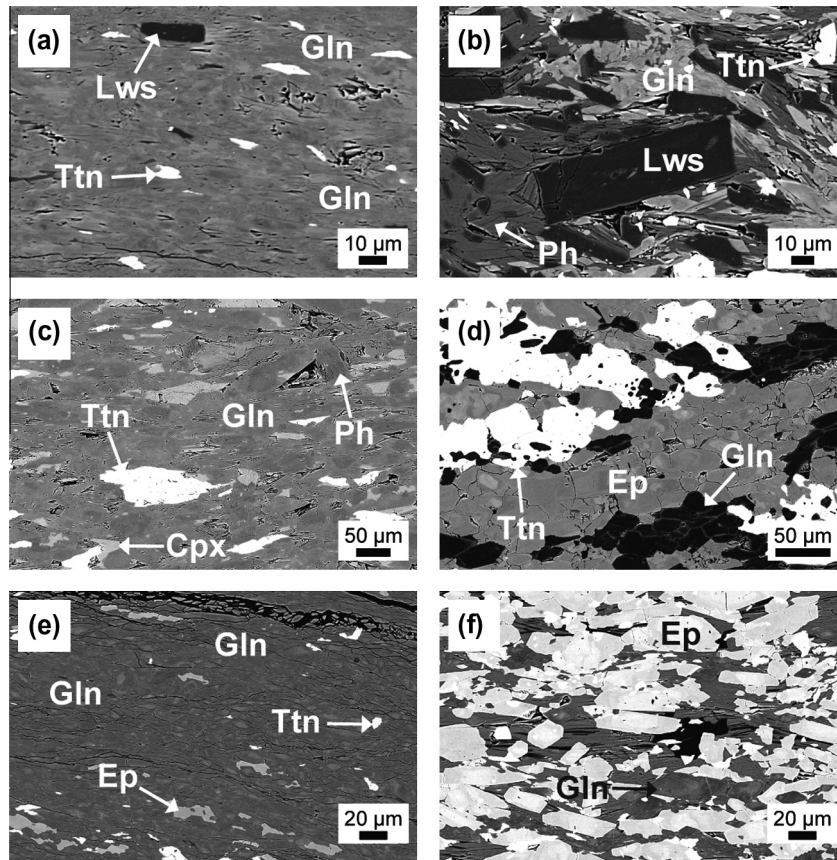


Fig. 2. Backscattered electron images of the analyzed samples (XZ sections: X, horizontal; Z, vertical). (a) Glaucophane-rich and (b) lawsonite-rich layers in NI-01. (c) CZ-02. (d) Omi-02. (e) Glaucophane-rich and (f) epidote-rich layers in Omi-03. Mineral abbreviations follow those in Whitney and Evans (2010).

tial glaucophane is relatively fine-grained (~ 5 to ~ 20 μm) and anhedral to subhedral. Porphyroclastic lawsonite has angular and straight grain boundaries, euhedral grain shape, and grain size ranging from ~ 10 to ~ 30 μm , and weakens the overall shape preferred orientation (Fig. 2).

The highly foliated Ward Creek lawsonite blueschist (CZ-02) is characterized by prograde-zoned garnet and relatively large grains (~ 30 to ~ 100 μm) of subhedral glaucophane (Figs. 1c and 2c). Fine-grained (~ 10 μm) garnet grains are mostly euhedral or subhedral and sometimes have a reaction texture with clinopyroxene and white mica. Although the sections used in this study contain only small amounts of lawsonite ($< 2\%$), the mineral assemblage garnet + lawsonite nevertheless represents the peak metamorphic conditions.

The Omi epidote blueschists (Omi-02 and 03) have a relatively weak foliation and lineation (Fig. 1d, e, and f). The garnet-bearing epidote blueschist (Omi-02) predominantly comprises glaucophane and epidote. Large grained (> 1 mm) garnet is usually broken and the area between grains is filled by clinopyroxene. Fine-grained glaucophane (~ 5 to ~ 10 μm) and epidote (~ 5 to ~ 10 μm) generally have smooth grain boundaries, which might have been affected by grain boundary area reduction during the main deformation event (Fig. 2d). Most glaucophanes have a weak chemical zoning. The specimen Omi-03 from the area of epidote glaucophane schist (Tsujimori, 2002) can be divided into glaucophane-rich (GRL Omi-03) and epidote-rich (ERL Omi-03) layers (Fig. 1e and f) by a similar criterion with the NI-01. The GRL Omi-03 is a very fine-grained blueschist. Highly foliated glaucophane has irregular grain boundaries, undulose extinction, and very fine grains ($< \sim 10$ μm), and epidote displays anhedral to subhedral grain shape with size ranging from ~ 5 to ~ 20 μm . The ERL

Omi-03 is characterized by relatively large and euhedral epidote (~ 10 to ~ 30 μm) with interstitial glaucophane (~ 5 to ~ 20 μm). Sometimes chemical zoning can be observed for glaucophane.

Glaucophane, a sodic amphibole, is defined by $(\text{Na} + \text{K})_{\text{A}} < 0.50$, $\text{Mg}/(\text{Mg} + \text{Fe}^{2+}) \geq 0.5$, and ${}^6\text{Al} \geq \text{Fe}^{3+}$ (Leake et al., 1997). Therefore, most of the spots we analyzed can be defined as glaucophane (Fig. 3; Table 2). A few spots located in the cores or rims of glaucophane plot instead as magnesioriebeckite, winchite, or actinolite (Fig. 3). Our analyzed glaucophanes are characterized by a decrease in Al from core to rim (Table 2), suggesting they formed during retrogression (Maruyama et al., 1986). The mineral assemblages (and making due reference to previous studies of similar assemblages) indicate peak metamorphic conditions of $P > 1.0$ GPa and $T = 200$ – 290 $^{\circ}\text{C}$ for the New Idria lawsonite blueschists, $P \sim 1.8$ – 2.2 GPa and $T = 430$ – 440 $^{\circ}\text{C}$ for the Ward Creek lawsonite blueschists, and ~ 1 GPa and 400 – 460 $^{\circ}\text{C}$ for the Omi epidote blueschists (Maruyama and Liou, 1988; Tsujimori, 2002; Tsujimori et al., 2006, 2007). Although an increase in Al from core to rim could be observed in GRL Omi-03 (Table 2), the glaucophane in the matrix would normally have formed by the retrograde metamorphism of eclogite and by the alteration of jadeite (Deer et al., 1992). In addition, Tsujimori (2002) reported that retrograde blueschist-facies overprinting is in garnet-free P – T range. We have therefore adopted the metamorphic conditions noted above for this study.

5. Results

5.1. Microscopic analyses

Most of the glaucophane has a high aspect ratio (3.0–12.8) with long axes at low angles to the foliation (Fig. 4; Table 1). In the New

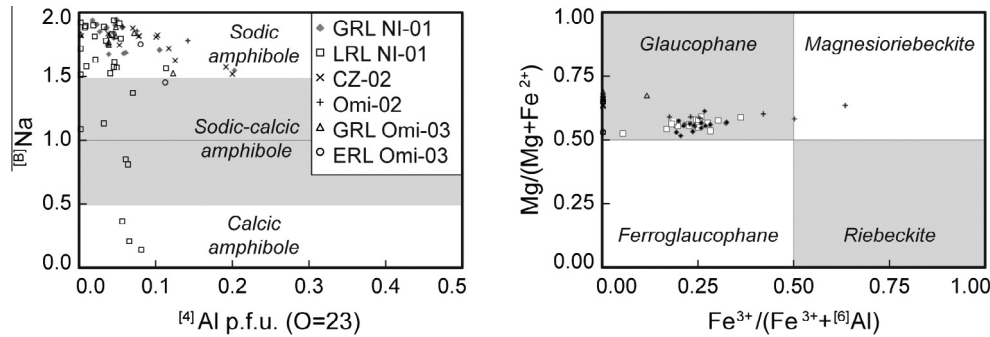


Fig. 3. Chemical compositions of the amphiboles. Ferric iron was calculated from the average of the maxima and minima estimated according to a total of 15 cations at T, C, and B sites, and 13 cations at T and C sites (Leake et al., 1997).

Table 2

Chemical compositions of representative sodic amphiboles in each sample.

Sample No.	NI-01		CZ-02		Omi-02		Omi-03					
	Glaucophane-rich layer		Lawsonite-rich layer				Glaucophane-rich layer		Epidote-rich layer			
Spot No.	110408-8	110408-10	110401-50C	110401-51R	120419-51C	120419-47R	120419-26	120419-21	120419-01C	120419-02R	120419-12C	120419-11R
SiO ₂	55.39	53.53	56.33	56.35	57.41	56.84	57.46	56.84	55.44	56.21	55.87	54.33
TiO ₂	0.04	0.02	0.10	–	0.04	0.01	–	–	0.07	–	0.06	0.05
Al ₂ O ₃	7.11	8.73	8.62	7.84	11.52	10.33	11.22	11.19	3.60	8.43	8.36	5.82
Cr ₂ O ₃	0.03	0.02	0.02	0.03	0.04	0.04	–	0.03	0.02	0.03	0.01	0.02
FeO*	16.40	16.04	15.09	14.94	9.18	10.28	10.18	10.18	19.33	14.99	15.16	16.34
MnO	0.16	0.24	0.07	0.21	0.09	0.19	0.03	0.02	0.13	0.16	0.17	0.19
MgO	8.63	9.05	8.54	9.18	10.44	10.43	9.99	9.83	9.81	8.79	9.18	10.00
CaO	1.27	1.29	0.41	2.28	1.08	1.32	0.68	0.96	0.59	0.65	1.10	3.12
Na ₂ O	6.92	6.32	7.51	6.15	7.06	6.66	7.31	7.20	7.10	7.32	6.85	5.80
K ₂ O	0.01	0.02	0.02	0.03	0.02	0.01	–	–	–	0.01	0.01	0.03
Total	95.95	95.24	96.71	97.00	96.87	96.11	96.87	96.23	96.08	96.59	96.76	95.69
Cations	O = 23	O = 23	O = 23	O = 23	O = 23	O = 23	O = 23	O = 23	O = 23	O = 23	O = 23	O = 23
Si	7.96	7.80	7.96	7.98	7.92	7.95	7.94	7.93	8.00	7.95	7.92	7.89
Ti	0.00	0.00	0.01	–	0.00	0.00	–	–	0.01	–	0.01	0.01
Al	1.20	1.50	1.44	1.31	1.88	1.70	1.83	1.84	0.61	1.41	1.40	1.00
Cr	0.00	0.00	0.00	0.00	0.00	0.00	–	0.00	0.00	0.00	0.00	0.00
Fe ³⁺	0.54	0.46	0.46	0.29	0.00	0.00	0.00	0.17	1.04	0.46	0.00	0.00
Fe ²⁺	1.43	1.49	1.32	1.48	1.06	1.20	1.18	1.02	1.30	1.32	1.80	1.98
Mn	0.02	0.03	0.01	0.03	0.01	0.02	0.00	0.00	0.02	0.02	0.02	0.02
Mg	1.85	1.97	1.80	1.94	2.15	2.18	2.06	2.04	2.11	1.85	1.94	2.17
Ca	0.20	0.20	0.61	0.35	0.16	0.20	0.10	0.14	0.09	0.10	0.17	0.49
Na	1.93	1.79	2.06	1.69	1.89	1.81	1.96	1.86	1.99	2.01	1.88	1.63
K	0.00	0.00	0.00	0.01	0.00	0.00	–	–	0.16	0.12	0.00	0.01
Total	15.13	15.24	15.67	15.07	15.08	15.06	15.07	15.00	15.32	15.23	15.14	15.19
gIn	0.66	0.75	0.77	0.70	0.96	0.93	0.99	0.89	0.38	0.75	0.98	0.84
mrB	0.31	0.27	0.26	0.16	0.00	0.00	0.00	0.09	0.65	0.25	0.00	0.00
act	0.38	0.32	0.12	0.68	0.30	0.37	0.19	0.28	0.17	0.19	0.31	0.89
ts	0.00	0.01	0.00	0.00	0.00	0.00	0.00	0.00	0.00	0.00	0.00	0.01

C, core; R, rim; –, not detected. FeO* indicates total Fe as Fe²⁺. The Fe³⁺ calculation of glaucophane employs the average of maximum and minimum values (Leake et al., 1997).

Idria blueschists, lawsonite has a relatively low aspect ratio (3.6–5.0) with long axes at higher angles to the foliation than glaucophane (Fig. 4a, b; Table 1). Epidote is characterized by grains of relatively low aspect ratio (2.1–3.4), with long axes at high angles to the foliation (Fig. 4d–f; Table 1).

Fig. 5 shows the grain size distributions in the analyzed samples. To deal with uncertainties and trivial peaks, we assume that points higher than a frequency of 5 are valid. Glaucophane typically displays a very fine grain size (1–59 μm), with two peaks in the grain size distributions for the New Idria blueschists, and a single peak for the Ward Creek and Omi blueschists (Fig. 5; Table 1). The lawsonite is characterized by slightly larger grains (15–20 μm) and a broader range of grain size (10–30 μm) with a single peak (Fig. 5; Table 1). Epidote usually has a fine grain size (10–20 μm)

with a single peak, except in the Omi-03 (Fig. 5; Table 1). The Omi-03 contains two certain peaks of grain size distributions of epidote. The grain size distribution data shows, therefore, that a single peak in the distributions is common, that two peaks could be observed for glaucophane in the New Idria blueschists and epidote in the Omi blueschists, and that glaucophane has the smallest grain size.

5.2. EBSD patterns

Glaucophane, lawsonite, and epidote each have distinctive CPOs. Pole figures of glaucophane in the analyzed samples have (100) subparallel to the foliation and [001] subparallel to the lineation (Fig. 6), with the *J*-index intensity ranging from 9.0 (Omi-02)

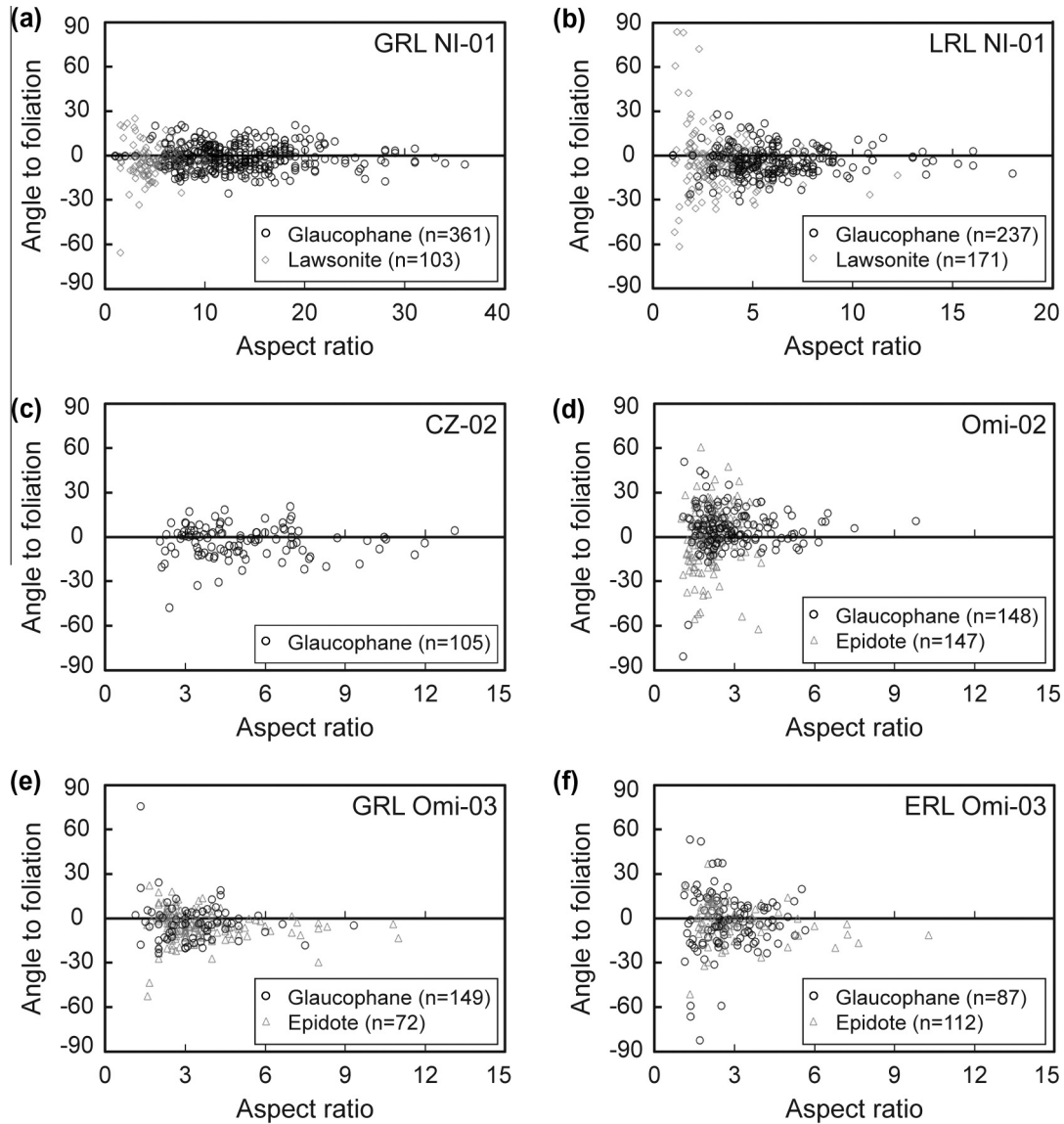


Fig. 4. Angles between grain long-axes and the mean foliation plane vs. aspect ratios, as calculated using the image-analysis software ImageJ 1.44 (<http://rsb.info.nih.gov/ij/>). Best-fit ellipses were used to reduce the complexity of diverse shapes.

to 32.5 (GRL Omi-03) (Table 1). Lawsonite in the New Idria blueschist (NI-01) has [010] subparallel to the lineation, foliation-subnormal [001] axes, and scattered [100] (Fig. 7). The J -index intensity for lawsonite in the New Idria blueschist (NI-01) is 7.8 in the GRL and 9.6 in the LRL (Table 1). Epidote has (010) subparallel to the lineation, [001] subnormal to the foliation, and (100) has a scattered distribution (Fig. 8). The value of the J -index intensity ranges from 7.2 (Omi-02) to 12.5 (GRL Omi-03) (Table 1). The (100) poles of glaucophane in the epidote blueschist (Omi-03) particularly have a higher pdf than [100] axes parallel to the lineation, suggesting the stronger development of a foliation rather than a lineation (Fig. 6). The J -indices of poles figures can be compared with the grain sizes of glaucophane, lawsonite, and epidote in Table 1 and the plots of Figs. 6–8.

5.3. Seismic anisotropy

The V_p , V_{S1} , V_{S2} , AV_S , and V_{S1} polarizations of average glaucophane, lawsonite, epidote, and whole rocks for the New Idria lawsonite blueschist (NI-01) and Omi epidote blueschist (Omi-03) are projected onto the lower hemisphere in Figs. 9 and 10. Since the

number of analysis points for each sample is similar (240 ± 22), the average seismic properties can be calculated from the sum of data for each sample. The seismic properties of average glaucophane are estimated to be 6.87–8.42 km/s for V_p , 4.39–4.86 km/s for V_{S1} , and 4.32–4.54 km/s for V_{S2} , with a seismic anisotropy of 20.4% for AV_p and 11.48% for AV_S (Fig. 9a). The patterns for average glaucophane show V_{pmax} along the lineation, AV_{Smax} and V_{S1max} polarization subparallel to the foliation, and with the directions of V_{pmin} , AV_{Smin} , and V_{S1min} polarization normal to the foliation. The V_p value of average lawsonite is calculated to be 7.66–8.44 km/s, V_{S1} is 4.02–4.55 km/s, and V_{S2} is 3.69–4.24 km/s, with a strong seismic anisotropy ($AV_p = 9.6\%$, $AV_S = 19.88\%$) (Fig. 9b). The V_{pmax} of average lawsonite is developed perpendicular to the foliation, as are the [001] axes, the AV_{Smax} and V_{S1max} polarizations are vertical, V_{pmin} is formed subparallel to the lineation, and the AV_{Smin} and V_{S1min} polarizations are subparallel to the lineation. The evaluated V_p , V_{S1} , and V_{S2} of average epidote are 7.09–7.75, 4.16–4.44, and 4.09–4.31 km/s, respectively (Fig. 9c). The seismic anisotropy of average epidote is relatively weak ($AV_p = 9.0\%$, $AV_S = 8.04\%$) compared with the other minerals. The patterns of seismic properties are similar to those of glaucophane, so that

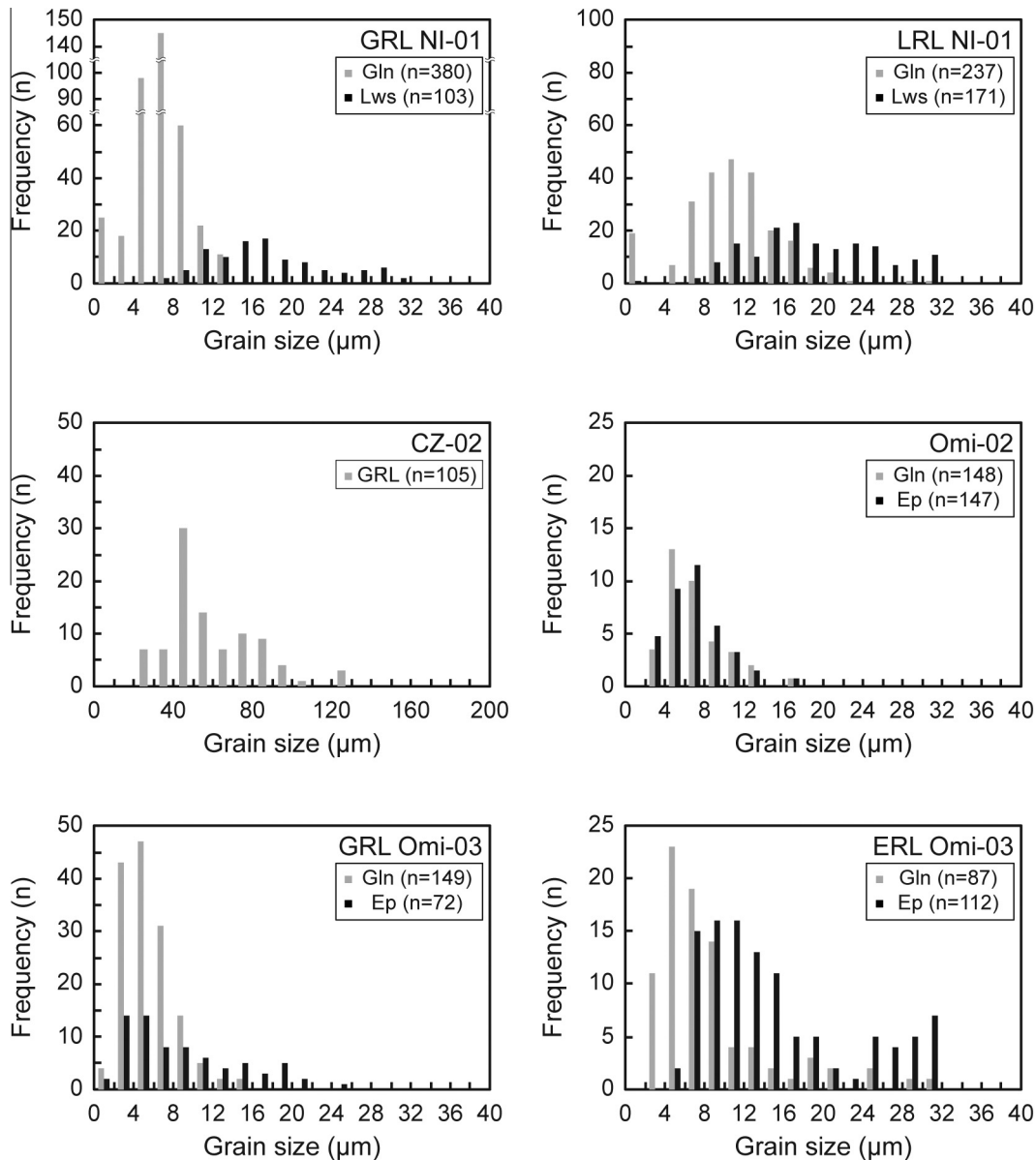


Fig. 5. Grain size distributions. A square grain shape was assumed for grain size calculations. See the text for details.

the V_{Pmax} and AV_{Smax} of epidote are parallel to the lineation and foliation, respectively, and V_{Pmin} and AV_{Smin} are developed normal to the foliation.

The seismic properties of whole rocks are evaluated with the assumption that the lawsonite and epidote blueschists only contain glaucophane, lawsonite, and epidote. The New Idria lawsonite blueschist (NI-01) calculated on the basis of the averages for glaucophane and lawsonite has values of 6.99–8.31 km/s for V_p , 4.36–4.74 km/s for V_{S1} , and 4.27–4.51 km/s for V_{S2} , with AV_p being 12.0–17.2% and AV_s being 5.6–9.2% (Fig. 10a and b). The anisotropic seismic patterns of lawsonite blueschist are similar to those of glaucophane, with V_{Pmax} parallel to the lineation, AV_{Smax} and V_{S1max} polarizations parallel to the foliation, and V_{Pmin} and AV_{Smin} perpendicular to the foliation. The V_p of the Omi epidote blueschist (Omi-03), calculated from the average glaucophane and epidote, is 6.88–8.38 km/s, V_{S1} is 4.20–4.83 km/s, V_{S2} is 4.16–4.53 km/s, and the seismic anisotropy is stronger ($AV_p = 11.8$ –19.6% and $AV_s = 8.4$ –11.1%) than in the lawsonite blueschist (Fig. 10c and d). The V_{Pmax} and AV_{Smax} of the epidote blueschist are parallel to the lineation

and foliation, respectively, while V_{Pmin} and AV_{Smin} are developed normal to the foliation.

6. Discussion

6.1. Deformational mechanisms of glaucophane, lawsonite, and epidote

Microstructures are affected by (i) progressive metamorphism where rock-forming minerals transform according to the progressively changing mineral stability fields, and (ii) the deformation of minerals, the manner of which changes with the mineral and the various prevailing conditions. Natural amphiboles can be subject to different deformation mechanisms such as cataclastic deformation, rigid-body rotation, and dynamic recrystallization (Cumbest et al., 1989; Ildefonse et al., 1990; Nyman et al., 1992; Siegesmund et al., 1994). Glaucophane, on the other hand, tends to deform predominantly by crystal plastic mechanisms via the

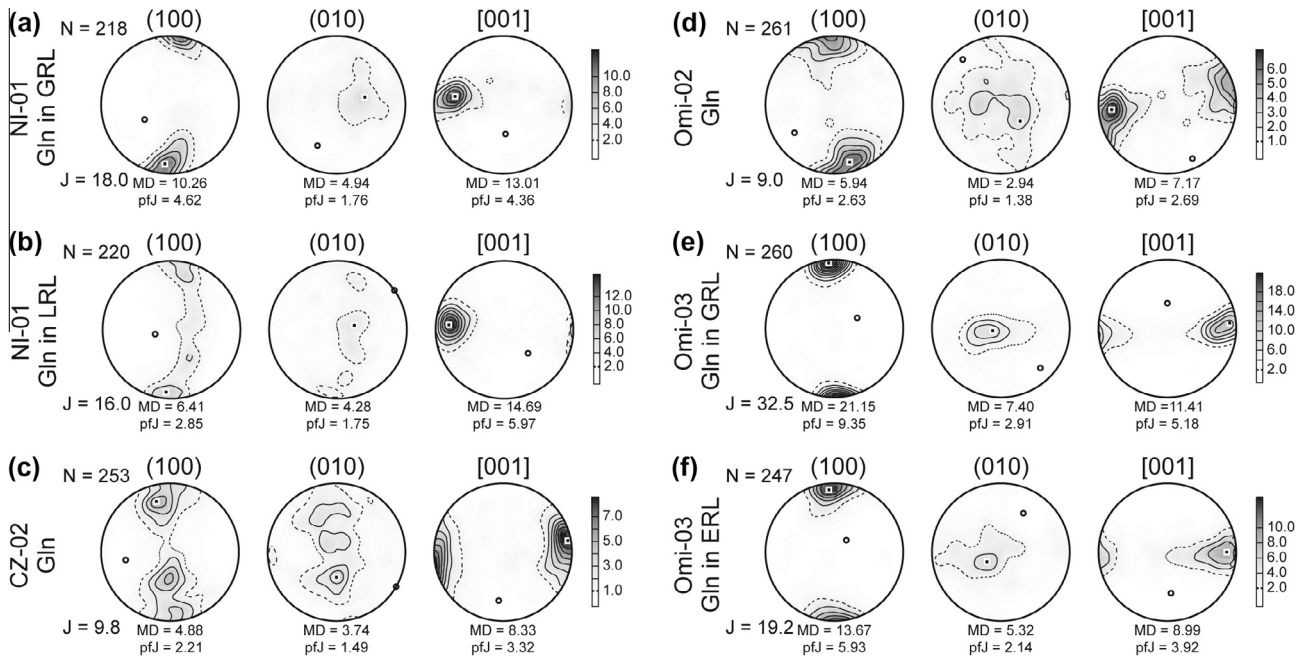


Fig. 6. Pole figures for glaucophane in the analyzed samples. Poles were plotted on lower hemisphere equal-area projections with contours in multiples of uniform distribution (m.u.d) for the density of poles. N: Number of measurements; J: J-index; MD: Maximum density.

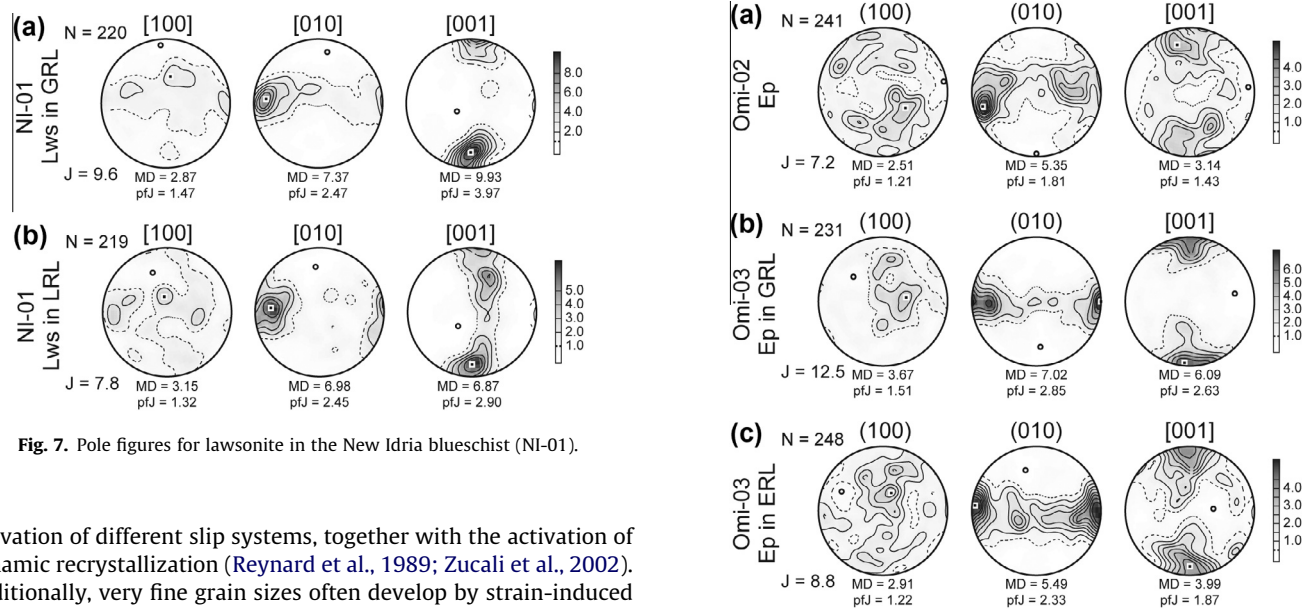


Fig. 7. Pole figures for lawsonite in the New Idria blueschist (NI-01).

activation of different slip systems, together with the activation of dynamic recrystallization (Reynard et al., 1989; Zucali et al., 2002). Additionally, very fine grain sizes often develop by strain-induced recrystallization during or after crystal plastic deformation (e.g., Drury and Urai, 1990). In the present specimens, the glaucophanes display strong CPOs and a very fine grain size that is possibly the product of grain size reduction, suggesting that the microstructures formed as a result of dynamic recrystallization (e.g., Díaz Aspiroz et al., 2007). This interpretation is supported by the relationship between grain size and the J-index of pole figures, and by the presence of two peaks in the grain size distributions from some samples (Figs. 5 and 6; Table 1). Therefore, the glaucophanes exhibit characteristic of dynamic recrystallization, possibly accommodated by dislocation creep. The Omi garnet-bearing blueschists (Omi-02) exhibit gently curved grain boundaries between glaucophane and epidote, suggesting the activation of grain boundary area reduction during recovery (Fig. 2d). Irregular or curved grain boundaries of glaucophane imply annealing and grain growth as a result of the reduction of interfacial free energy in a low stress re-

gime (Fig. 2) (Evans et al., 2001). Although dissolution and precipitation creep are the dominant deformation mechanisms for calcic amphiboles at low temperatures, the weak chemical zoning and the very fine grain size of the analyzed glaucophanes demonstrate that these mechanisms were not important for the glaucophane.

On the other hand, the deformation mechanisms of lawsonite and epidote are poorly understood. Teyssier et al. (2010) interpreted lawsonite as a rigid phase based on the assumption that the associated glaucophane is weaker. Similarly, Kim et al. (2013) reported lawsonite to be stronger than glaucophane according to fabric analyses of two distinct layers in the New Idria lawsonite blueschist. Lawsonite in the present specimens has relatively

Fig. 8. Pole figures for epidote in the Omi blueschists (Omi-02 and 03).

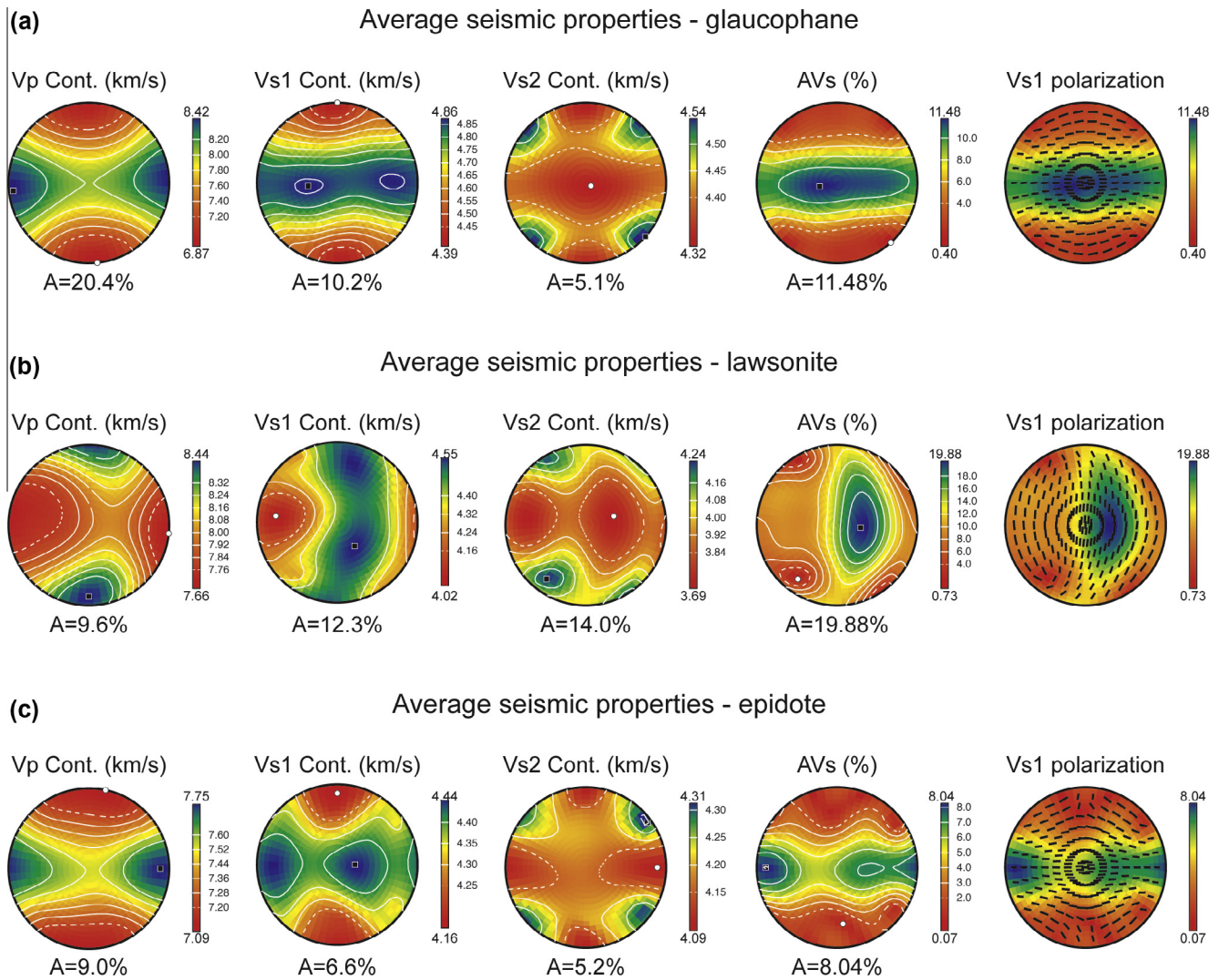


Fig. 9. Calculated seismic anisotropies of (a) average glaucophane, (b) lawsonite, and (c) epidote. The Voigt–Reuss–Hill averaging scheme and lower hemisphere equal area projections are used.

strong CPOs, even though euhedral grains are present with angular and straight boundaries (Fig. 2a and b). Therefore, the lawsonite microstructures that formed within the wide stability field of lawsonite possibly developed with the aid of rigid body rotations. Epidote in the present specimens also exhibits straight grain boundaries and euhedral shapes, implying rigid body rotation as the dominant deformation mechanism. In view of these straight grain boundaries, the two conspicuous grain-size-distribution peaks for epidote in the epidote-rich layer in Omi blueschist (ERL Omi-03) can probably be attributed to two stages of growth, during prograde and retrograde metamorphism, rather than to dynamic recrystallization (Figs. 2f and 5). Our results suggest, consequently, that microstructures of the bulk rock and each mineral such as epidote and lawsonite were decided by deformation of glaucophane.

6.2. *P–T* conditions of deformation

Lawsonite and epidote eclogites generally form at depths greater than 45 km in subduction zones (Tsujimori et al., 2006), and they transform to other minerals and rocks during the relatively low *P–T* conditions of exhumation so that they are relatively rare at the surface, especially without some degree of alteration. The Diablo Range and Ward Creek in California, and the Omi area in

central Japan, are unusual in that they expose unaltered lawsonite or epidote eclogites, implying rapid exhumation, probably as a result of slab breakoff. Lawsonite in the New Idria blueschist, and epidote in the Omi epidote blueschists, possibly formed during prograde subduction-related metamorphism, rather than during uplift and exhumation, based on the euhedral grain shapes and straight grain boundaries. At a late stage of subduction the maximum pressure conditions attained for the New Idria serpentinite body were >1.3 GPa (Tsujimori et al., 2007), and the maximum *P–T* conditions attained in the Hida metamorphic belt were >1.8 GPa and 550–600 °C (Tsujimori, 2002).

On the other hand, most of the glaucophane analyzed here possibly formed along a retrograde *P–T* path, based on its typical occurrence in the matrix, and the decrease in Al from core (glaucophane) to rim (winchite or actinolite). Although glaucophane in the glaucophane-rich layer in the Omi blueschist (GRL Omi-03) is the exception, in that it shows an increase of Al from core to rim, it still occurs in the matrix, and it might therefore have formed during retrogression and been altered after uplift. This can be supported by garnet-free assemblages of the Omi-03, in the retrograde *P–T* path of a previous study (Tsujimori, 2002). The well-aligned fabrics displayed by glaucophane, lawsonite, and epidote, characterized by the relatively low angles between crystal long axes and the mean

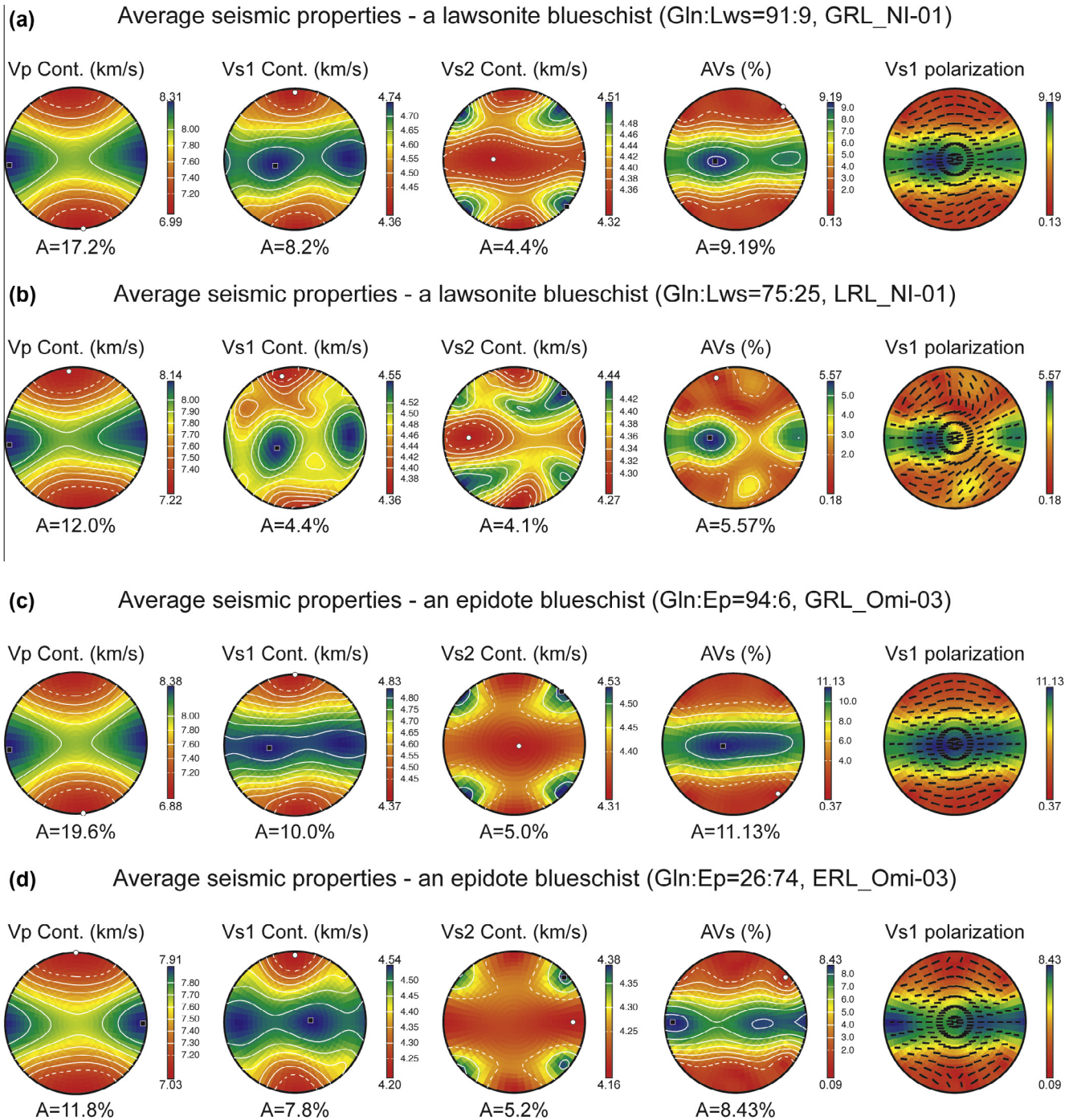


Fig. 10. Seismic anisotropy evaluated for lawsonite blueschists (a) GRL NI-01 and (b) LRL NI-01, and epidote blueschists (c) GRL Omi-03 and (d) LRL Omi-03.

position of the foliation plane, indicate that deformation took place during or after the blueschist-facies overprinting (Fig. 4). The strong CPOs that define the foliation might be attributed to the flow of dynamically recrystallized grains, denoting the presence of synkinematic microstructures (e.g., Hippertt and Hongn, 1998). Consequently, the microstructures in the analyzed samples are thought to have formed at $P > 1$ GPa and $T = 200\text{--}290$ °C for the New Idria blueschist (Tsuji-mori et al., 2007), $P = \sim 1.8\text{--}2.2$ GPa and $T = 430\text{--}440$ °C for the Ward Creek blueschist (Tsuji-mori et al., 2006), and $P = \sim 1$ GPa and $T = 400\text{--}460$ °C for the Omi blueschists (Tsuji-mori, 2002), consistent with the stability field of blueschist (Fig. 11).

6.3. Seismic properties of lawsonite and epidote blueschists in the subducting slab

The angle of subduction, which is influenced by the age of the crust and depositional materials during movement to the subduction zone, can affect the P – T increase during subduction; consequently, the geothermal gradient is high in SW Japan and low in NE Japan. Owing to the stability field of blueschist, lawsonite blueschist is the main constituent of the oceanic crust beneath NE Japan, while epidote blueschist is the main constituent beneath SW Japan. The V_p of lawsonite (6.99–8.31 km/s) and epidote blueschists (6.88–8.38 km/s), as modeled from the average seismic

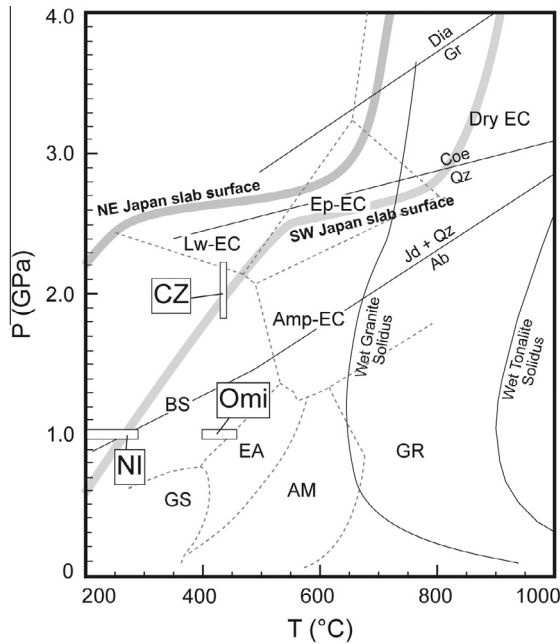


Fig. 11. Deformational P - T conditions for the analyzed samples. The pressure-temperature paths for NE and SW Japan are after Syracuse et al. (2010). GS: greenschist; AM: amphibolite; EA: epidote amphibolite; GR: granulite; BS: blueschist; Amp-EC: amphibole eclogite; Lw-EC: lawsonite eclogite; Ep-EC: epidote eclogite; Dry EC: dry eclogite; NI: NI-01; CZ: CZ-02; Omi: Omi-02 and 03.

properties of their main rock-forming minerals, are higher than the values at ~ 30 – 50 km depth derived from recent seismological studies in NE Japan (7.1–7.4 km/s; Tsuji et al., 2008) and SW Japan (7.1–7.5 km/s; Shelly et al., 2006) (Fig. 10). The slightly faster seismic velocity in SW Japan, compared with NE Japan, is consistent, however, with our study. The average velocities of lawsonite blueschist are $V_p = 7.67$ km/s and $V_s = 4.44$ km/s (Fig. 10a and b), and these are similar values to the modeled result of $V_p = 7.71$ km/s and $V_s = 4.49$ km/s (Bezacier et al., 2010), as well as an experimental result of $V_p = 6.0$ – 7.4 km/s (Fujimoto et al., 2010). Therefore, since the seismic properties calculated for our samples are similar to those previously observed and modeled, and to experimental data, it suggests that our results are valid for the purposes of our study.

To better understand the implications of the seismic anisotropy of bulk rock masses, the AV_{Pmax} and AV_{Smax} of lawsonite and epidote blueschists have been computed using the assumption that a mass of rock is composed mainly of diverse modal abundances of average glaucophane, lawsonite, and epidote (Fig. 12). The seismic anisotropy of lawsonite blueschist is evaluated as $AV_p = 3.9$ – 20.4% and $AV_s = 4.54$ – 19.88% with a ‘concave’ feature characterized by lower values in the center and higher values in both ends (Fig. 12). An offset of the different propagating directions of seismic waves between glaucophane and lawsonite may cause the specific ‘concave’ feature, which is distinct from the ‘straight’ (directly or inversely proportional) change of AV_p and AV_s that is attributed to the same propagating direction of seismic waves in glaucophane and epidote (Bezacier et al., 2010; Satsukawa et al., 2011). The AV_p and AV_s of epidote blueschist are calculated as $AV_p = 9.0$ – 20.4 km/s and $AV_p = 8.04$ – 11.48 km/s with ‘straight’ lines. Consequently, we note that the seismic anisotropy of a mass of rock, especially one composed of highly anisotropic phases, is controlled by the modes of the constituent rock-forming minerals and the anisotropic seismic patterns of each phase. This proposition is consistent with the stronger trench-parallel seismic anisotropy in the Ryukyu arc (epidote blueschist) and the weaker anisotropy in NE Japan (lawsonite

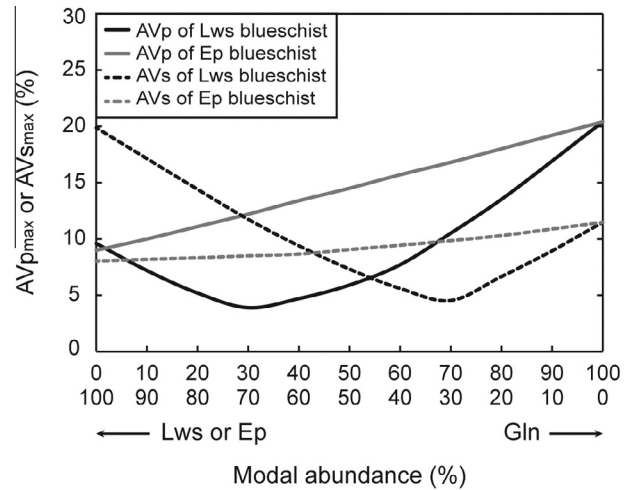


Fig. 12. A graph for AV_{Pmax} and AV_{Smax} according to modal abundance. The AV_{Pmax} and AV_{Smax} of blueschists were computed from the average of the seismic anisotropies of glaucophane and lawsonite with every 10% step.

blueschist). The fastest V_p and AV_s of glaucophane and bulk rocks are along the foliation, whereas V_{pmin} and AV_{smin} are developed normal to the foliation and lineation (Figs. 9a and 10). The results indicate that a weak seismic anisotropy develops subnormal to the shear direction, and also that the V_{Pmax} and AV_{Smax} of glaucophane and the bulk rock are subparallel to the movement direction. Deformation mainly occurs in response to the movement direction of the subducting plate, and the fast shear wave is therefore established subparallel to the trench (trench-parallel fast anisotropy) (Fig. 13). On the other hand, lineation-perpendicular propagations of the fast V_{S1} polarization of lawsonite are generated perpendicular to the movement direction of the subducting oceanic crust, and hence a trench-perpendicular anisotropy can occur (Fig. 13).

The strong anisotropic properties of minerals can also be useful for understanding the nature of the LVL (Nikulin et al., 2009; Bostock, 2012; Wirth and Long, 2012). Chantel et al. (2012) reported a reasonably low V_s of lawsonite with strong anisotropy due to the (010)[001] slip system, which is in contrast to other studies (Fujimoto et al., 2010; Teyssier et al., 2010), including the present study. We therefore apply the results of our study to the LVL according to subducting angles, mainly using the preferred orientations and V_p/V_s ratios of minerals. A low seismic velocity can be produced when seismic waves propagate along the V_{pmin} and V_{smin} directions of minerals. For local events, slow seismic waves can be generated by changes in rock type, such as eclogite to blueschist, and the V_{pmin} and V_{smin} therefore need to be parallel to the lineation in the eclogite. This explains why the [010] axes of lawsonite are more appropriate rather than the (010) planes of epidote for local events. On the other hand, teleseismic waves can be generated normal to the surface of the crust, and this is suitable for a warm slab in which the (100) planes of glaucophane contain V_{pmin} and V_{smin} . The V_p/V_s ratios are calculated as 2.08 for lawsonite ($V_p = 7.66$ km/s and $V_s = 3.69$ km/s) and 1.59 for glaucophane ($V_p = 6.87$ km/s and $V_s = 4.32$ km/s). Although the V_p/V_s ratios estimated for glaucophane are rather low, the values for lawsonite are higher than those for the other minerals present. Therefore, lawsonite might contribute to the low velocity layer with high V_p/V_s ratios, whereas blueschists lacking lawsonite require other minerals such as serpentine or pore fluids along the grain-boundaries.

The thickness of an anisotropic layer is used to compare the seismic properties of glaucophane, lawsonite, and epidote with other well-known anisotropic minerals such as olivine and serpentine (e.g., Katayama, 2009). The thickness (D) of the anisotropic

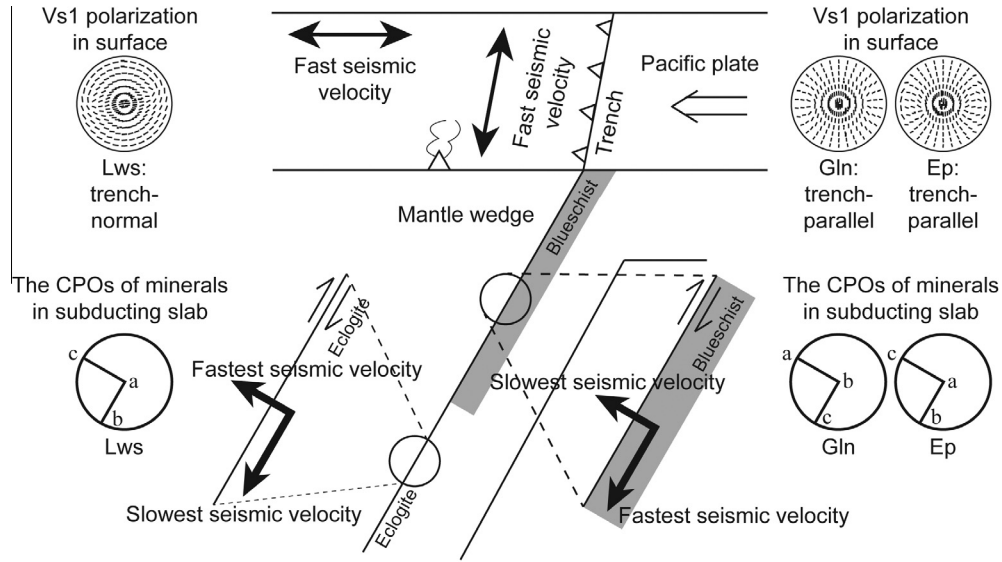


Fig. 13. A schematic model showing trench-parallel and trench-normal fast anisotropies. The subducting angle is assumed to be 60°, however the patterns of V_{s1} polarization at the surface is based on 90° of subducting angle.

layer is decided by the multiplication of velocity (v) and time (t), and hence the delay time (dt) is defined by the following equation:

$$dt = AV_S / \langle V_S \rangle D,$$

where AV_S is the anisotropy of a specific propagation direction and $\langle V_S \rangle$ indicates the average velocity of the fast and slow velocities. Fig. 14 shows the relations between the delay time and the thickness of the seismically anisotropic layer that is composed of glaucophane, lawsonite, and epidote aggregates. The calculated results for olivine ($AV_S = 4.5\%$ and $\langle V_S \rangle = 4.75$ km/s; Katayama and Karato, 2006) and serpentine ($AV_S = 36.0\%$ and $\langle V_S \rangle = 4.13$ km/s; Katayama et al., 2009) are shown for comparison. With respect to the observed delay time (0.06–0.10 s) of trench-parallel AV_S beneath NE Japan (Nakajima and Hasegawa, 2004), the thickness of the anisotropic layer is calculated to be 2–4 km for average glaucophane, and 3–4 km for average epidote (Fig. 14). The estimates are thicker than the calculated thickness for serpentine (1 km), but noticeably thinner than for olivine (6–11 km). Using a 7 ± 1 km thickness for the oceanic crust (White et al., 1992), a 2–4 km anisotropic layer caused by glaucophane is capable of producing the trench-parallel fast anisotropy beneath NE Japan (cold subducting slab). On the other hand, the thickness of the anisotropic layer caused by lawsonite is calculated to be 2–5 km for trench-normal fast anisotropy, based on the observed delay times (0.10–0.26 s) in NE Japan (Nakajima and Hasegawa, 2004). Given the delay time (~ 1 –2 s) beneath the Ryukyu arc (Long and van der Hilst, 2005), the thickness can be computed to be 39–79 km for average glaucophane and 42–83 km for average epidote (Fig. 14). The thickness of an anisotropic layer comprising serpentine (11–23 km) or olivine (105–211 km) is insufficient to explain the strong seismic anisotropy beneath the Ryukyu arc (hot subducting slab) only by a single mineral phase. Our results suggest, therefore, that beneath NE Japan, glaucophane may contribute to the trench-parallel seismic anisotropy in the forearc, and lawsonite to the trench-normal anisotropy in the back-arc. Beneath the Ryukyu arc, serpentine and olivine may also partly help to generate the seismic anisotropy.

Natural rocks, however, are composed of poly-phases, and the mineral assemblages need to be considered along with the subduction processes. The lawsonite blueschists contain 75–91% of glaucophane and 9–25% of lawsonite, and these main constituents show different seismic anisotropic patterns from each other

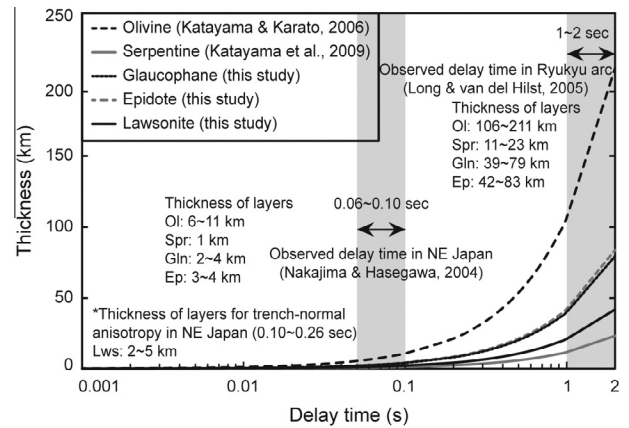


Fig. 14. Relationship between the calculated thickness of the anisotropic layer and the delay time. The delay time and thickness of an anisotropic layer of olivine ($AV_S = 4.5\%$, $\langle V_S \rangle = 4.75$ km/s; Katayama and Karato, 2006) and serpentine ($AV_S = 35.9\%$, $\langle V_S \rangle = 4.13$ km/s; Katayama et al., 2009) are also plotted for comparison.

(Fig. 10a, b; Table 1). On the other hand, the epidote blueschists consist mainly of glaucophane 26–94% and epidote 6–74%, and these minerals have similar anisotropic patterns (Fig. 10c, d; Table 1). The similar anisotropic patterns of epidote and glaucophane lead one to suggest that the seismic anisotropy of epidote blueschist is the same as the average values of the epidote and glaucophane seismic anisotropies (Figs. 9a, c and 10). The differing patterns of seismic anisotropy for lawsonite and glaucophane, however, act against each other, so that a lawsonite blueschist has a lower seismic anisotropy than an epidote blueschist (Figs. 9a, b and 12). The countervailing effect of lawsonite might be related to the weak trench-parallel seismic anisotropy in NE Japan, whereas the complementary patterns of the seismic anisotropies of epidote and glaucophane might be the cause of the strong trench-parallel seismic anisotropy in the Ryukyu arc. Beneath NE Japan, glaucophane, along with the countervailing effects of lawsonite, controls the seismic anisotropy of the subducting slab at ~ 30 –110 km depth. At 110 km depth the glaucophane breaks down, and omphacite forms within the stability field of lawsonite

during eclogitization. The seismic anisotropy of eclogite may be governed, therefore, by a strongly seismic anisotropic mineral such as lawsonite ($AV_P = 9.6\%$ and $AV_S = 19.88\%$ in our samples), because the seismic anisotropy of omphacite is low ($AV_{P_{\max}} = 1.9\%$, $AV_{S_{\max}} = 2.5\%$; Bascou et al., 2001). In addition, lawsonite has a V_{S1} polarization that is perpendicular to the foliation, and this can explain the trench-perpendicular seismic anisotropy observed beneath NE Japan. Other factors, such as physical variables or microstructural conditions (minor phases, grain boundaries, microcracks, and alteration), need to be considered for a complete understanding of seismic velocities, but the above results suggest that trench-parallel and trench-normal seismic anisotropy beneath NE Japan can be explained by glaucophane and lawsonite, respectively, and that the weak trench-parallel anisotropy beneath NE Japan can be attributed to the countervailing effects of lawsonite. In addition, the strong seismic anisotropy beneath the Ryukyu arc might be dominated in the subducting oceanic crust by combinations of minerals with similar seismic anisotropic patterns, such as glaucophane and epidote, and in the mantle wedge by minerals such as serpentine and olivine.

7. Conclusions

We presented important new data concerning (i) the seismic anisotropy of subducting oceanic crust and (ii) the microstructures and deformational behavior of rock-forming minerals in natural lawsonite blueschists from the Diablo Range and the Franciscan Complex in California, and in natural epidote blueschists from the Hida Mountains, Japan. We carefully compared the calculated seismic velocities and anisotropies of glaucophane, lawsonite, and epidote with observatory data for subduction zones. The principal results of our investigations into the microstructures and seismic properties are as follows.

- (1) Glaucophane, as the main constituent of the matrix, is very fine grained, has a strong shape preferred orientations, high aspect ratios, and distinct CPOs (Figs. 1, 2, 4 and 6). All microstructures of the glaucophane suggest *characteristic of dynamic recrystallization probably activated by dislocation creep*. On the other hand, lawsonite and epidote both occur as porphyroclasts, and their euhedral grain shapes and straight grain boundaries (Figs. 1, 2, 4, 7 and 8) indicate that deformation took place primarily by rigid body rotation.
- (2) The calculated average seismic velocities ($V_P = 6.87\text{--}8.42$ km/s, $V_S = 4.32\text{--}4.86$ km/s for glaucophane; $V_P = 7.66\text{--}8.44$ km/s, $V_S = 3.69\text{--}4.55$ km/s for lawsonite; $V_P = 7.09\text{--}7.75$ km/s, $V_S = 4.09\text{--}4.44$ km/s for epidote) are similar to previous observations (Shelly et al., 2006; Tsuji et al., 2008), modeling results (Bezacier et al., 2010), and experimental data (Fujimoto et al., 2010) (Fig. 9). For an average glaucophane and epidote, the propagations of V_P and V_S polarization develop along the lineation and foliation, respectively, while for an average lawsonite they are subnormal to the foliation and lineation, respectively. Foliation-subparallel V_S polarization in glaucophane and epidote can generate a trench-parallel seismic anisotropy owing to the development of a foliation parallel to the direction of the subduction, whereas the V_S polarization of lawsonite can establish a trench-normal seismic anisotropy (Fig. 13).
- (3) Relatively strong seismic anisotropies were calculated for the main mineral phases in blueschists ($AV_P = 20.4\%$, $AV_S = 11.5\%$ for glaucophane; $AV_P = 9.6\%$, $AV_S = 19.9\%$ for lawsonite; $AV_P = 9.0\%$, $AV_S = 8.0\%$ for epidote) (Fig. 9). A thin anisotropic layer composed of glaucophane, epidote, and lawsonite is sufficient to explain the observed delay time

of trench-parallel (0.06–0.10 s) and trench-normal (0.10–0.26 s) shear wave splitting beneath NE Japan (Nakajima and Hasegawa, 2004), but it is insufficient for the Ryukyu arc (1–2 s; Long and van der Hilst, 2005) (Fig. 14). The calculations based on the relative abundance of the constituent minerals are consistent with the ‘concave’ changes of AV_P and AV_S that depend on mineral abundances, and also with the stronger trench-parallel anisotropy in the Ryukyu arc and the weaker seismic anisotropy in NE Japan (Fig. 12). All the data collected from natural blueschists indicate the seismic anisotropies of lawsonite and epidote, in combination with that of glaucophane, play important roles in producing the trench-parallel and trench-normal seismic anisotropies, and they also provide explanations for the low velocity layer in subduction zones.

Acknowledgments

The authors appreciate the technical support of Y. Shibata and T. Satsukawa for the EPMA and EBSD analyses, respectively. Careful comments by L.F.G. Morales and an anonymous reviewer, and editing by K. Hirose significantly improved earlier version of the manuscript. Most of the support for this project came from the Japan Society for the Promotion of Science (JSPS) to I.K. (#21684030), with partial assistance from the JSPS for K.M. (#22244062) and T.T. (#22654058).

References

- Aleksandrov, K.S., Alchikov, U.V., Belikov, B.P., Zaslavskii, B.I., Krupnyi, A.I., 1974. Velocities of elastic waves in minerals at atmospheric pressure and increasing precision of elastic constants by mean of EVM (in Russian). *Izv. Acad. Sci. USSR Seol. Ser.* 10, 15–24.
- Banno, S., 1958. Glaucophane schists and associated rocks in the Omi district, Niigata Prefecture, Japan. *Jpn. J. Geol. Geogr.* 29, 29–44.
- Bascou, J., Barruola, G., Vauchez, A., Mainprice, D., Eglydio-Silva, M., 2001. EBSD-measured lattice-preferred orientations and seismic properties of eclogites. *Tectonophysics* 342, 61–80.
- Bezacier, L., Reynard, B., Bass, J.D., Wang, J., Mainprice, D., 2010. Elasticity of glaucophane, seismic velocities and anisotropy of the subducted oceanic crust. *Tectonophysics* 494, 201–210.
- Bostock, M.G., 2012. The Moho in subduction zones. *Tectonophysics*, in press. <http://dx.doi.org/10.1016/j.tecto.2012.07.007>.
- Bunge, H.J., 1982. *Texture Analysis in Materials Science*. Butterworth, London, p. 559.
- Chantel, J., Mookherjee, M., Frost, D.J., 2012. The elasticity of lawsonite at high pressure and the origin of low velocity layers in subduction zones. *Earth Planet. Sci. Lett.* 349–350, 116–125.
- Coleman, R.G., 1980. Tectonic inclusions in serpentinite. *Arch. Sci. Société de Physique et d'Histoire Naturelle de Genève* 33, 89–102.
- Coleman, R.G., Lee, D.E., 1963. *Ultrahigh-Pressure Metamorphism*. Cambridge University Press, New York, pp. 528.
- Cumbest, R.J., Drury, M.R., Van Roermund, H.L.M., Simpson, C., 1989. Dynamic recrystallization and chemical evolution of clinoamphibole from Senja Norway. *Contrib. Mineral. Petrol.* 101, 339–349.
- Deer, W.A., Howie, R.A., Zussman, J., 1992. *The Rock-forming Minerals*, second ed. Longmans, London, p. 266.
- Díaz Aspiroz, M., Lloyd, G.E., Fernández, C., 2007. Development of lattice preferred orientation in clinoamphiboles deformed under low-pressure metamorphic conditions. A SEM/EBSD study of metabasites from the Aracena metamorphic belt (SW Spain). *J. Struct. Geol.* 29, 629–645.
- Drury, M.R., Urai, J.L., 1990. Deformation-related recrystallization processes. *Tectonophysics* 172, 235–253.
- Evans, B., Renner, J., Hirth, G., 2001. A few remarks on the kinetics of static grain growth in rocks. *Int. J. Earth Sci.* 90, 88–103.
- Fujimoto, Y., Kono, Y., Hirajima, T., Kanagawa, K., Ishikawa, M., Arima, M., 2010. P-wave velocity and anisotropy of lawsonite and epidote blueschists: constraints on water transportation along subducting oceanic crust. *Phys. Earth Planet. Inter.* 183, 219–228.
- Hippert, J.F., Hongn, F.D., 1998. Deformation mechanisms in the mylonite/ultramylonite transition. *J. Struct. Geol.* 20, 1435–1448.
- Ildefonse, B., Lardeauz, J.-M., Caron, J.-M., 1990. The behavior of shape preferred orientations in metamorphic rocks: amphiboles and jadeites from the Monte Mucone area (Sesia-Lanzo zone, Italian Western Alps). *J. Struct. Geol.* 12, 1005–1011.

- Jung, H., Karato, S.-I., 2001. Water-induced fabric transitions in olivine. *Science* 293, 1460–1463.
- Katayama, I., 2009. Thin anisotropic layer in the mantle wedge beneath northeast Japan. *Geology* 37, 211–214.
- Katayama, I., Karato, S.-I., 2006. Effect of temperature on the B- to C-type olivine fabric transition and implication for flow pattern in the subduction zone. *Phys. Earth Planet. Inter.* 157, 33–45.
- Katayama, I., Hirauchi, K., Michibayashi, K., Ando, J., 2009. Trench-parallel anisotropy produced by serpentine deformation in the hydrated mantle wedge. *Nature* 461, 1114–1117.
- Kim, D., Katayama, I., Michibayashi, K., Tsujimori, T., 2013. Rheological contrast between glaucophane and lawsonite in naturally deformed blueschist from Diablo Range, California. *Isl. Arc* 22, 63–73. <http://dx.doi.org/10.1111/iar.12003>.
- Kita, S., Okada, T., Nakajima, J., Matsuzawa, T., Hasegawa, A., 2006. Existence of a seismic belt in the upper plane of the double seismic zone extending in the along-arc direction at depths of 70–100 km beneath NE Japan. *Geophys. Res. Lett.* 33, L24310.
- Leake, B.E., Woolley, A.R., Arps, C.E.S., Birch, W.D., Gilbert, M.C., Grice, J.D., Hawthorne, F.D., Kato, A., Kisch, H.J., Krivovichev, V.G., Linthout, K., Laird, J., Mandarino, J.A., Maresch, W.V., Nickel, E.H., Rock, N.M.S., Schumacher, J.C., Smith, D.C., Stephenson, N.C.N., Ungaretti, L., Whittaker, E.J.W., Youzhi, G., 1997. Nomenclature of amphiboles: report of the subcommittee on amphiboles of the international mineralogical association, commission on new minerals and mineral names. *Can. Mineral.* 35, 219–246.
- Long, D.L., van der Hilst, R.D., 2005. Upper mantle anisotropy beneath Japan from shear wave splitting. *Phys. Earth Planet. Inter.* 151, 206–222.
- Long, M.D., Silver, P.G., 2008. The subduction zone flow field from seismic anisotropy: A global view. *Science* 18, 315–318.
- Mainprice, D., 1990. An efficient Fortran program to calculate seismic anisotropy from the lattice preferred orientation of minerals. *Comput. Geosci.* 16, 385–393.
- Mainprice, D., Silver, P.G., 1993. Interpretation of SKS-waves using samples from the subcontinental lithosphere. *Phys. Earth Planet. Inter.* 78, 257–280.
- Mainprice, D., Barruol, G., Ben Ismail, W., 2000. The anisotropy of the Earth's mantle: from single crystal to polycrystal. In: Karato, S., Forte, A.M., Liebermann, R.C., Masters, G., Stixrude, L. (Eds.), *Mineral Physics and Seismic Tomography: From Atomic to Global*. Geoph. Monog., vol. 117, pp. 237–264.
- Mao, Z., Jiang, F., Duffy, T.S., 2007. Single-crystal elasticity of zoisite $\text{Ca}_2\text{Al}_3\text{Si}_3\text{O}_{12}$ (OH) by Brillouin scattering. *Am. Mineral.* 92, 570–576.
- Maruyama, S., Cho, M., Liou, J.G., 1986. Experimental investigations of blueschist–greenschist transition equilibria: pressure dependence of Al_2O_3 contents in sodic amphiboles—A new barometer. In: Evans, B.W., Brown, E.H. (Eds.), *Blueschist and Eclogite*. Geol. Soc. Am. Mem., vol. 164, pp. 1–16.
- Maruyama, S., Liou, J.G., 1987. Clinopyroxene a mineral telescoped through the processes of blueschist facies metamorphism. *J. Metamorph. Geol.* 5, 529–552.
- Maruyama, S., Liou, J.G., 1988. Petrology of Franciscan metabasites along the jadeite–glaucophane type facies series, Cazadero, California. *J. Petrol.* 29, 1–37.
- Mezger, J.E., 2010. Rotation of irregular staurolite porphyroblasts in a simple shear dominated shear zone controlled by initial growth orientation and aspect ratio. *J. Struct. Geol.* 32, 1147–1157.
- Mookherjee, M., Bezacier, L., 2012. The low velocity layer in subduction zone: structure and elasticity of glaucophane at high pressures. *Phys. Earth Planet. Inter.* 208–209, 50–58.
- Nakajima, J., Hasegawa, A., 2004. Shear-wave polarization anisotropy and subduction induced flow in the mantle wedge of northeastern Japan. *Earth Planet. Sci. Lett.* 225, 365–377.
- Nikulin, A., Levin, V., Park, J., 2009. Receiver function study of the Cascadia megathrust: evidence for localized serpentinization. *Geochem. Geophys. Geosyst.* 10, Q07004.
- Nyman, M.W., Law, R.D., Smelik, E., 1992. Cataclastic deformation for the development of core mantle structures in amphibole. *Geology* 20, 455–458.
- Prior, D.J., Boyle, A.P., Brenker, F., Cheadle, M.C., Day, A., Lopez, G., Peruzzo, L., Potts, G.J., Reddy, S., Spiess, R., Timms, N.E., Trimby, P., Wheeler, J., Zetterstrom, L., 1999. The application of electron backscatter diffraction and orientation contrast imaging in the SEM to textural problems in rocks. *Am. Mineral.* 84, 1741–1759.
- Randle, V., 1992. *Microtexture Determination and its Applications*. The Institute of Materials, Minerals and Mining, London, p. 174.
- Randle, V., Engler, O., 2000. *Introduction to Texture Analysis: Macrotexture, Microtexture and Orientation Mapping*. CRC Press, London, p. 408.
- Reynard, B., Gillet, P., Willaime, C., 1989. Deformation mechanisms in naturally deformed glaucophanes: a TEM and HREM study. *Eur. J. Mineral.* 1, 611–624.
- Satsukawa, T., Michibayashi, K., Anthony, E.Y., Stern, R.J., Gao, S.S., Liu, K.H., 2011. Seismic anisotropy of the uppermost mantle beneath the Rio Grande rift: evidence from Kilbourne Hole peridotite xenoliths, New Mexico. *Earth Planet. Sci. Lett.* 311, 172–181.
- Schmidt, M.W., Poli, S., 1998. Experimentally based water budgets for dehydrating slab and consequences for arc magma generation. *Earth Planet. Sci. Lett.* 163, 361–379.
- Shelly, D.R., Beroza, G.C., Ide, S., Nakamura, S., 2006. Low-frequency earthquake in Shikoku, Japan, and their relationship to episodic tremor and slip. *Nature* 422, 188–191.
- Siegesmund, S., Helming, K., Kruse, R., 1994. Complete texture analysis of a deformed amphibolite: comparison between neutron, diffraction and U-stage data. *J. Struct. Geol.* 16, 131–142.
- Sinogeikin, S.V., Schilling, F.R., Bass, J.D., 2000. Single crystal elasticity of lawsonite. *Am. Mineral.* 85, 1834–1837.
- Syracuse, E.M., van Keken, P.E., Abers, G.A., 2010. The global range of subduction zone thermal models. *Phys. Earth Planet. Inter.* 183, 73–90.
- Teyssier, C., Whitney, D.L., Toraman, E., Seaton, N.C.A., 2010. Lawsonite vorticity and subduction kinematics. *Geology* 38, 1123–1126.
- Tsuji, Y., Nakajima, J., Hasegawa, A., 2008. Tomographic evidence for hydrated oceanic crust of the Pacific slab beneath northeastern Japan: implications for water transportation in subduction zones. *Geophys. Res. Lett.* 35, L14308.
- Tsujimori, T., 2002. Prograde and retrograde *P–T* paths of the Late Paleozoic glaucophane eclogite from the Renge Metamorphic Belt, Hida Mountains, Southwestern Japan. *Int. Geol. Rev.* 44, 797–818.
- Tsujimori, T., Ishiwatari, A., Banno, S., 2000. Eclogitic glaucophane schist from the Yunotani valley in Omi Town, the Renge metamorphic belt, the Inner Zone of southwestern Japan. *J. Geol. Soc. Jpn.* 106, 353–362 (in Japanese with English abstract).
- Tsujimori, T., Sisson, V.B., Liou, J.G., Harlow, G.E., Sorensen, S.S., 2006. Very-low-temperature record in subduction process: a review of worldwide lawsonite eclogites. *Lithos* 92, 609–624.
- Tsujimori, T., Liou, G.J., Coleman, R.G., 2007. Finding of high-grade tectonic blocks from the New Idria serpentinite body, Diablo Range, California: petrologic constraints on the tectonic evolution of an active serpentinite diapir. In: Cloos, M., Carlson, W.D., Gilbert, M.C., Liou, J.G., Sorensen, S.S. (Eds.), *Convergent Margin Terranes and Associated Regions: a Tribute to Ernst, W.G.*, Geol. S. Am. S., vol. 419, pp. 67–80.
- White, R.S., McKenzie, D., O'Nions, R.K., 1992. Oceanic crustal thickness from seismic measurements and rare earth element inversions. *J. Geophys. Res.* 97, 19683–19715.
- Whitney, D.L., Evans, B.W., 2010. Abbreviations for names of rock-forming minerals. *Am. Mineral.* 95, 185–187.
- Wines, D.A., Conder, J.A., Faul, U.J., 2008. The seismic structure and dynamics of the mantle wedge. *Annu. Rev. Earth Planet. Sci.* 36, 421–455.
- Wirth, E.A., Long, M.D., 2012. Multiple layers of seismic anisotropy and a low-velocity region in the mantle wedge beneath Japan: evidence from teleseismic receiver functions. *Geochem. Geophys. Geosyst.* 13, Q08005.
- Zucali, M., Chateigner, D., Dugnani, M., Lutterotti, L., Ouladdiaf, B., 2002. Quantitative texture analysis of glaucophanite deformed under eclogite facies conditions (Sesia–Lanzo Zone, Western Alps): comparison between X-ray and neutron diffraction analysis. *Geol. Soc. Lond. Spec. Publ.* 200, 239–253.

Thematic Article

Rheological contrast between glaucophane and lawsonite in naturally deformed blueschist from Diablo Range, CaliforniaDAEYEONG KIM,^{1*} IKUO KATAYAMA,¹ KATSUYOSHI MICHIBAYASHI,² AND TATSUKI TSUJIMORI³

¹Department of Earth and Planetary Systems Science, Graduate School of Science, Hiroshima University, Higashi-Hiroshima 739-8526, Japan (email: daeyeongkim@hiroshima-u.ac.jp), ²Institute of Geosciences, Shizuoka University, Shizuoka 422-8529, Japan, and ³Pheasant Memorial Laboratory, Institute for Study of the Earth's Interior, Okayama University, Misasa, Tottori 682-0193, Japan

Abstract Deformation microstructures for a lawsonite blueschist from the New Idria serpentinite body, Diablo Range, are investigated to clarify rheological behaviors of glaucophane and lawsonite, which are main mineral assemblages of subducting oceanic crust at relatively cold geotherm. Developments of crystal-preferred orientations (CPOs) with small grain size, irregular grain boundary and high aspect ratio of glaucophane indicate deformation mechanism as recovery and dynamic recrystallization possibly accommodated by dislocation creep, while lawsonite deforms by rigid body rotation based on euhedral grains with angular or straight grain boundaries. Higher aspect ratios, lower angle to foliation, and stronger CPOs of both minerals in the glaucophane-rich layer rather than those in the lawsonite-rich layer suggest the strain localization into the glaucophane-rich layer. Additionally fabric strength (the degree of crystal alignment) and seismic anisotropy are higher in the glaucophane-rich layer than that of the lawsonite-rich layer, which is consistent with the microstructural analyses. All our results imply, therefore, the dominant role of glaucophane rather than lawsonite for rheological behavior and seismic anisotropy of blueschist.

Key words: blueschist, crystal-preferred orientation, glaucophane, lawsonite, rheological contrast, strain localization.

INTRODUCTION

Investigations on strength contrast among minerals or competence contrast among layers can be important to aid understanding of geological problems such as the depth of earthquakes and viscous coupling between the crust and mantle. Especially in subduction zones, dehydration of hydrous phases and formation of high-pressure minerals occur with high stress regimes. Those phenomena are crucial for the comprehension of crust–mantle circulations.

Blueschist usually forms at low-temperature and high-pressure conditions by the subduction and metamorphism of oceanic crust originating from mid-ocean ridge basalt (MORB). High-

pressure minerals, such as glaucophane and lawsonite, can be preserved as an inclusion or a matrix, which might form during subduction or exhumation, respectively. Although dissolution–precipitation creep is one of the dominant deformation mechanisms of calcic amphibole at low temperature (e.g., Imon *et al.* 2004), rigid-body rotation (Ildefonse *et al.* 1990), dislocation creep with recovery (Reynard *et al.* 1989), and dynamic recrystallization (Zucali *et al.* 2002) are also possible deformation mechanisms of natural glaucophane deformed at relatively high pressures. Deformation mechanisms and slip systems of glaucophane during the retrograde stage, however, are poorly understood.

We therefore conducted fabric analyses of lawsonite blueschist from the New Idria serpentinite body of the Diablo Range, California, USA, to delineate the rheological behaviors of subducting

*Correspondence.

Received 28 February 2012; accepted for publication 19 July 2012.

oceanic crust. The body underwent a blueschist-facies overprint during exhumation (Tsuji-mori *et al.* 2007), and therefore represents the rock that was deformed during the retrograde process. The deformation conditions might be similar to those of subduction (especially in the case of grain size), and the deformation mechanisms and relative strength between glaucophane and lawsonite are discussed.

SAMPLE DESCRIPTION

GEOLOGICAL OUTLINE

The New Idria serpentinite body in the Diablo Range, a part of the Coalinga anticline, borders the Upper Cretaceous Panoche and Moreno Formations of the Great Valley Group and Franciscan Complex. The body containing numerous tectonic blocks of greenstone and low-grade blueschists comprises primary chrysotile-lizardite serpentinite and minor antigorite serpentinite which was a moderately depleted harzburgite based on chemical compositions of relict minerals (Coleman 1980; Tsujimori *et al.* 2007). The presence of high-grade tectonic blocks composed of retrograded eclogite and garnet amphibolite indicates the origin of the New Idria serpentinite from mantle depth (Tsuji-mori *et al.* 2007). The investigated lawsonite blueschists were collected as a boulder at near eclogite locality along the Clear Creek (Fig. 1).

MINERAL ASSEMBLAGES AND TEXTURES

In this study, we selected a sample, which contains two distinctively representative parts, a glaucophane-rich layer (GRL) and a lawsonite-rich layer (LRL), on the basis of mineral abundances (Fig. 2). This helps to clarify the rheological contrast between glaucophane and lawsonite, and its effects on active slip systems and seismic anisotropy of subducting oceanic crust. The GRL comprises primarily glaucophane (89%), lawsonite (8%), and rare phengite around lawsonite with minor accessory minerals (titanite and apatite) (Fig. 2a,c). Glaucophane as a main component of the matrix is highly foliated and elongated with very

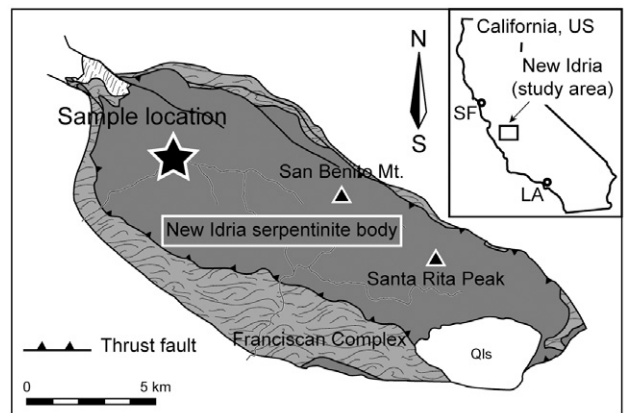


Fig. 1 Simplified geologic map and the sample location. See Tsujimori *et al.* (2007) and Coleman (1996) for a larger-scaled map. Qls: Holocene-Pleistocene alluvium; SF, San Francisco; LA, Los Angeles.

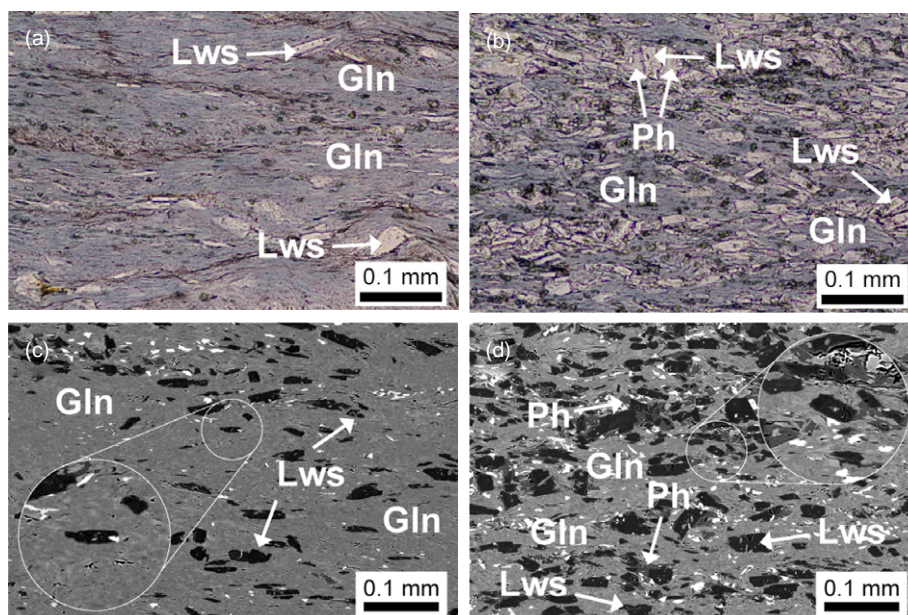


Fig. 2 Photomicrographs and back-scattered electron images (BSE) of two representative domains. (a) and (c) show the glaucophane-rich layer defined by abundant glaucophane (89%), lawsonite (8%) and rare phengite, while (b) and (d) display the lawsonite-rich layer characterized by high concentrations of lawsonite (21%) partly wrapped by secondary phengite (dark grey in BSE). Enlarged figures show euhedral grain shape or straight grain boundaries of lawsonite. Lws, lawsonite; Gln, glaucophane; Ph, phengite. Mineral abbreviations follow Whitney and Evans (2010).

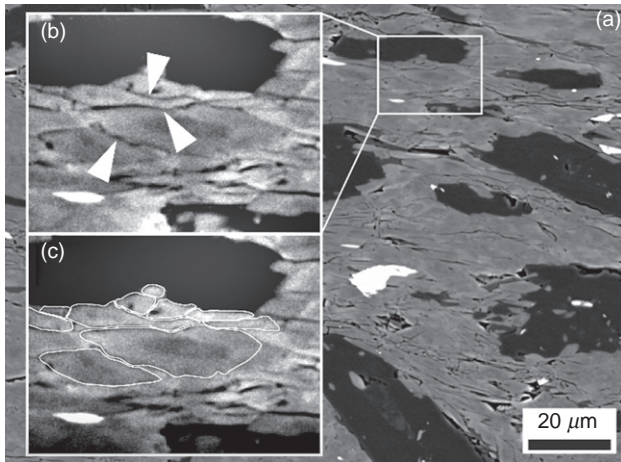


Fig. 3 Microstructures of glaucophane. (b) and (c) show the enlarged rectangle in (a). Sharp apices of triangles indicate curved or irregular grain boundary of glaucophane. (c) displays an example for the image analyses.

fine grain size, suggesting the possible formation of glaucophane during the exhumation process. Often an irregular grain boundary of glaucophane is observed (Fig. 3). Lawsonite having subhedral to euhedral shape with straight grain boundaries is preserved as porphyroclasts wrapped mostly by glaucophane. The LRL chiefly comprises glaucophane (64%), lawsonite (21%) and secondary phengite (11%) enclosing lawsonite (Fig. 2b,d). Grain sizes of minerals in the LRL are somewhat larger than those in the GRL.

MINERAL CHEMISTRY

Major elements of these minerals were measured using the JEOL JXA-8200 (EPMA), housed at Hiroshima University. We employ the average of maximum and minimum estimates on the basis of total cations as 13 for T- and C-sites, and 15 for T-, C- and B-sites, respectively, for the contents of ferric iron in amphibole (Table 1) (Leake *et al.* 1997). All sodic amphiboles ($^{[B]}Na \geq 1.5$) in both GRL and LRL are classified as glaucophane by definitions such as $(Na + K)_A < 0.50$, $Mg/(Mg + Fe^{2+}) \geq 0.5$, and ${}^6Al \geq Fe^{3+}$ (Fig. 4). Only a few grains in the LRL have core-rim structures characterized by the increase of $Fe^{3+}/(Fe^{3+} + {}^6Al)$, defining tschermkite substitution, and the decrease of Al and Na contents from core to rim, classifying the rim composition as winchite or actinolite (Fig. 4). The decrease of Al content from the core to the rim suggests the formation of amphibole during the retrograde stage, due to the systematic correlation between pressure and Al_2O_3

content of sodic amphibole (Maruyama *et al.* 1986). In addition, mineral assemblages (Gln + Lws + Ph + Ttn) are similar to those in blueschist-facies overprinting stage of high-grade blocks from New Idria (Tsuji-mori *et al.* 2007), except the lack of jadeite. We therefore adopt temperature ranges of 200–290°C for pumpellyite-zone metabasites (Maruyama & Liou 1988) and pressure ranges >1.0 GPa for the Jd + Qz stability field (Tsuji-mori *et al.* 2007) in this sample.

MICROSTRUCTURAL AND FABRIC ANALYSES

Measurements of aspect ratios, angle to the foliation, and grain size for minerals in XZ sections (the plane perpendicular to the foliation and parallel to the lineation) of the GRL and LRL were conducted by an image-analysis software ImageJ 1.44, in which best-fit ellipses for each grain were computed for reducing the complexity of various shapes (Fig. 3c) (e.g., Mezger 2010). Aspect ratios of glaucophane in each domain are distinctively diverse (12.8 average in the GRL and 6.0 in the LRL), in contrast to relatively similar results of aspect ratios in lawsonite (5.0 average in the GRL and 3.6 in the LRL) (Fig. 5, Table 2). Angles to the foliation of glaucophane in both layers exhibit almost similar results within 30°, while lawsonite in the LRL shows more scattered patterns than that in the GRL. The grain size of glaucophane in the GRL (7 μm mean value) is smaller than that in the LRL (12 μm), while distributions of grain size for lawsonite are comparable (18 μm in the GRL and 20 μm in the LRL) (Fig. 5, Table 2).

The Kikuchi bands were acquired for XZ sections and analyzed using the HKL–EBSD system attached to the Hitachi S-3400N at Shizuoka University. To unravel the effects of chemical zonings in glaucophane and lawsonite, automatic mappings (1 μm step size) for each domain were carried out. After we confirmed identical crystallographic orientation throughout the whole grain, the EBSD patterns were manually indexed. Pole figures were plotted using the software PFctf, made by D. Mainprice and J- and M-indexes were employed for estimating fabric strength (Mainprice & Silver 1993; Ismail & Mainprice 1998; Skemer *et al.* 2005). As a result, glaucophane and lawsonite in both layers have certain similar crystal-preferred orientations (CPOs) for each mineral except for slightly scattered patterns in the LRL. Glaucophane exhibits the [001] axes parallel to the

Table 1 Representative chemical compositions of minerals in each layer

Area Phase	Gln-rich layer						Lws-rich layer										
	Gln			Lws			Ph			Gln			Lws			Ph	
Spot no.	14	16	1	5	6	4	33	40	48c [†]	49r [‡]	79	80	17				
SiO ₂	56.05	56.05	56.13	38.36	37.67	52.45	55.86	56.77	56.09	56.00	37.92	37.66	52.86				
TiO ₂	0.00	0.03	0.03	0.03	0.13	0.03	0.08	0.08	0.06	0.05	0.09	0.19	0.06				
Al ₂ O ₃	8.12	7.21	8.54	31.55	30.95	24.19	8.01	8.40	9.28	6.87	30.90	31.12	23.11				
Cr ₂ O ₃	0.00	0.06	0.03	0.00	0.07	0.10	0.00	0.04	0.05	0.08	0.02	0.05	0.08				
FeO	16.12	16.21	15.94	1.48	0.97	3.79	14.81	15.20	14.71	15.54	1.31	0.96	3.27				
MnO	0.09	0.16	0.12	0.00	0.02	0.06	0.08	0.09	0.06	0.25	0.01	0.00	0.02				
MgO	8.33	8.84	7.87	0.01	0.05	4.22	8.79	8.66	8.14	9.32	0.04	0.02	4.73				
CaO	1.06	2.16	0.62	17.33	17.08	0.03	0.65	0.74	0.56	2.80	16.78	17.09	0.03				
N ₂ O	7.09	6.46	7.25	0.00	0.01	0.15	7.10	7.37	7.42	6.15	0.02	0.00	0.07				
K ₂ O	0.00	0.00	0.02	0.01	0.01	10.76	0.00	0.02	0.02	0.10	0.02	0.02	10.80				
P ₂ O ₅	0.00	0.00	0.00	0.00	0.00	0.00	0.00	0.00	0.00	0.00	0.00	0.00	0.00				
Total	96.86	97.16	97.53	88.77	86.96	95.79	95.36	97.37	96.38	97.14	87.12	87.09	95.04				
O.N.	23.00	23.00	23.00	8.00	8.00	11.00	23.00	23.00	23.00	23.00	8.00	8.00	11.00				
Si	7.96	7.96	7.98	2.01	2.02	3.51	7.99	7.97	7.95	7.96	2.02	2.01	3.56				
Ti	0.00	0.00	0.00	0.00	0.01	0.00	0.01	0.01	0.01	0.01	0.00	0.01	0.00				
Al	1.36	1.21	1.43	1.95	1.95	1.91	1.35	1.39	1.55	1.15	1.94	1.96	1.83				
Cr	0.00	0.01	0.00	0.00	0.00	0.01	0.00	0.00	0.01	0.01	0.00	0.00	0.10				
Fe ^{3+§}	0.45	0.43	0.43	0.07	0.04		0.46	0.46	0.36	0.41	0.06	0.04					
Fe ²⁺	1.91	1.93	1.90			0.21	1.77	1.78	1.74	1.85			0.18				
Mn	0.01	0.02	0.01	0.00	0.00	0.00	0.01	0.01	0.01	0.03	0.00	0.00	0.00				
Mg	1.76	1.87	1.67	0.00	0.00	0.42	1.88	1.81	1.72	1.97	0.00	0.00	0.47				
Ca	0.16	0.33	0.09	0.97	0.98	0.00	0.10	0.11	0.08	0.43	0.96	0.98	0.00				
Na	1.95	1.78	2.00	0.00	0.00	0.02	1.97	2.01	2.04	1.69	0.00	0.00	0.01				
K	0.00	0.00	0.00	0.00	0.00	0.92	0.00	0.00	0.00	0.02	0.00	0.00	0.93				
P	0.00	0.00	0.00	0.00	0.00	0.00	0.00	0.00	0.00	0.00	0.00	0.00	0.00				
Total	15.11	15.10	15.09	5.01	5.00	7.00	15.08	15.10	15.11	15.11	5.00	5.00	6.99				
gln	0.73	0.65	0.77				0.74	0.75	0.82	0.62							
mr ^b	0.25	0.24	0.23				0.25	0.25	0.20	0.23							
act	0.31	0.64	0.19				0.20	0.22	0.17	0.83							
ts	0.00	0.00	0.00				0.00	0.00	0.00	0.00							

[†] Including core compositions. [‡] Denoting rim compositions. [§] Employing the average of maximum and minimum ferric iron contents in glaucophane (Leake *et al.* 1997).

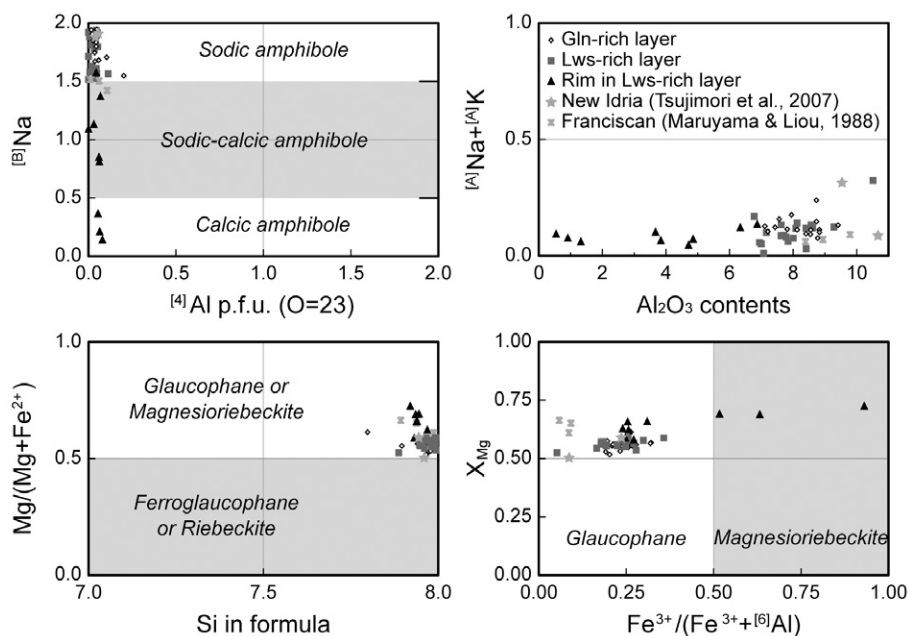


Fig. 4 Chemical compositions of amphibole. The contents of ferric iron in amphibole were calculated as the average of maximum and minimum estimates based on total cations as 15 for T-, C- and B-sites and 13 for T- and C-sites. Major elements of amphiboles in New Idria (Tsuji *et al.* 2007) and those in the Franciscan complex (Maruyama & Liou 1988) were also marked for comparisons.

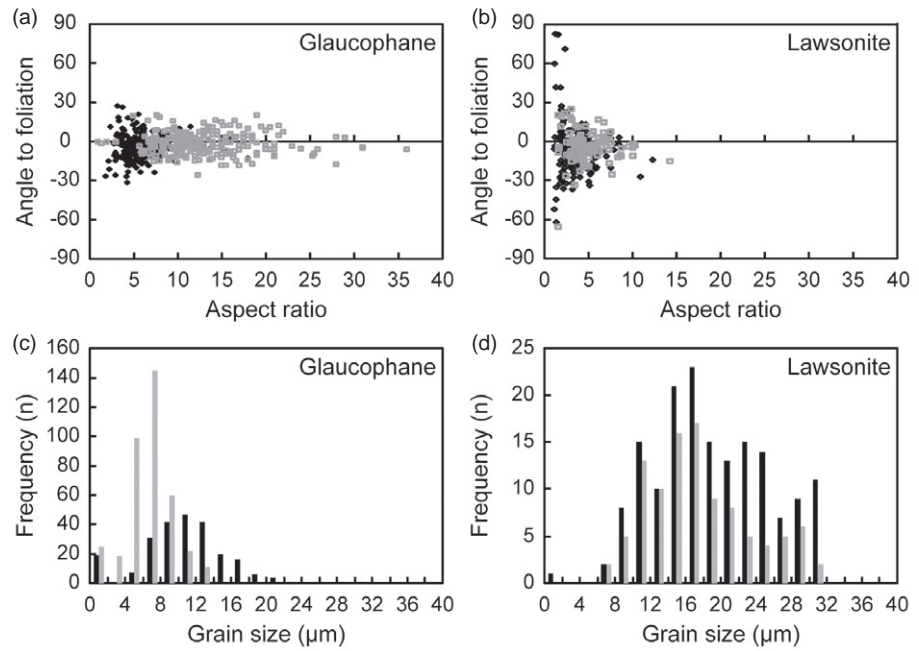


Fig. 5 Diagrams of the angle to foliation against aspect ratio, and the frequency of grain size calculated by ImageJ 1.44 (<http://rsb.info.nih.gov/ij/>). Best-fit ellipses were employed for diminishing the complexity of diverse shapes. Angles to foliation of (a) glaucophane: □, Gln-rich layer ($n = 236$); ◆, Lws-rich layer ($n = 237$), and (b) lawsonite: □, Gln-rich layer ($n = 103$); ◆, Lws-rich layer ($n = 171$). Grain sizes of (c) glaucophane: ■, GRL ($n = 236$); ▨, LRL ($n = 237$); and (d) lawsonite: ■, GRL ($n = 103$); ▨, LRL ($n = 171$).

Table 2 Comparisons of glaucophane and lawsonite in two dominant layers

Domain	Modal abundance [†]	Minerals	Grain size (µm)	Aspect ratio (with standard deviation)	Fabric strength	Seismic anisotropy AV_P	AV_S
Gln-rich layer	Gln89 Lws8	Gln	7	12.8 ± 6.4	$M = 0.20, J = 18.0$	25.3%	13.9%
		Lws	18	5.0 ± 2.3	$M = 0.21, J = 9.6$	10.7%	21.3%
Lws-rich layer	Gln64 Lws21	Gln	12	6.0 ± 2.8	$M = 0.18, J = 16.0$	20.2%	9.9%
		Lws	20	3.6 ± 1.5	$M = 0.15, J = 7.8$	8.8%	19.4%

[†] Excluding phengite, titanite and apatite (abundances of each mineral are less than 5%).

lineation, the (100) planes vertical to foliation plane, and relatively weak central maxima in the (010) planes (Fig. 6a,c). Glaucophane in the GRL ($M = 0.20, J = 18.0$) displays higher fabric strength than that in the LRL ($M = 0.18, J = 16.0$) (Fig. 6 and Table 2). The CPOs of lawsonite are characterized by vertical maxima in the [001] axes, horizontal maxima in the [010] axes, and weak patterns in the [100] axes (Fig. 6b,d). M - and J -indexes of lawsonite in the GRL are estimated as $M = 0.21$ and $J = 9.6$, while those in the LRL are $M = 0.15$ and $J = 7.8$ (Fig. 6 and Table 2).

We computed the seismic properties of glaucophane and lawsonite in the GRL and LRL. The seismic anisotropy of P-wave (AV_P) is defined by the maximum and minimum velocities in two different propagating paths, hence the percentage AV_{Pmax} can be calculated using the formula $200(V_{Pmax} - V_{Pmin})/(V_{Pmax} + V_{Pmin})$. The S-wave anisotropy (AV_S) is described as two different velocities of two orthogonally polarized S-waves separately propa-

gated through an anisotropic medium, therefore the percentage AV_{Smax} is calculated by the formula $200(V_{S1} - V_{S2})/(V_{S1} + V_{S2})$, in which V_{S1} and V_{S2} are faster and slower velocities, respectively. The elastic constants (C_{ij}) of glaucophane (Bezacier *et al.* 2010) and lawsonite (Sinogeikin & Bass 2000) are employed for calculating seismicity of crystals with the Voigt–Reuss–Hill averaging scheme. The V_P , AV_S and orientation of V_{S1} polarization of glaucophane and lawsonite in both layers are projected to lower hemispheres (Fig. 7). Seismic velocities in the GRL are V_P 6.73–8.68 km/s, V_{S1} 4.34–4.93 km/s and V_{S2} 4.27–4.57 km/s for glaucophane with strong anisotropy ($AV_{Pmax} = 25.3\%$ and $AV_{Smax} = 13.9\%$) and V_P 7.68–8.55 km/s, V_{S1} 4.11–4.55 km/s and V_{S2} 3.64–4.29 km/s for lawsonite with P- and S-wave seismic anisotropy as 10.7% and 21.3%, respectively (Fig. 7a,b). The V_P , V_{S1} and V_{S2} in the LRL are calculated to 7.15–8.74 km/s, 4.52–4.82 km/s and 4.29–4.60 km/s for glaucophane ($AV_P = 20.0\%$ and $AV_S = 9.9\%$) and 7.65–8.35 km/s, 3.93–4.56 km/s,

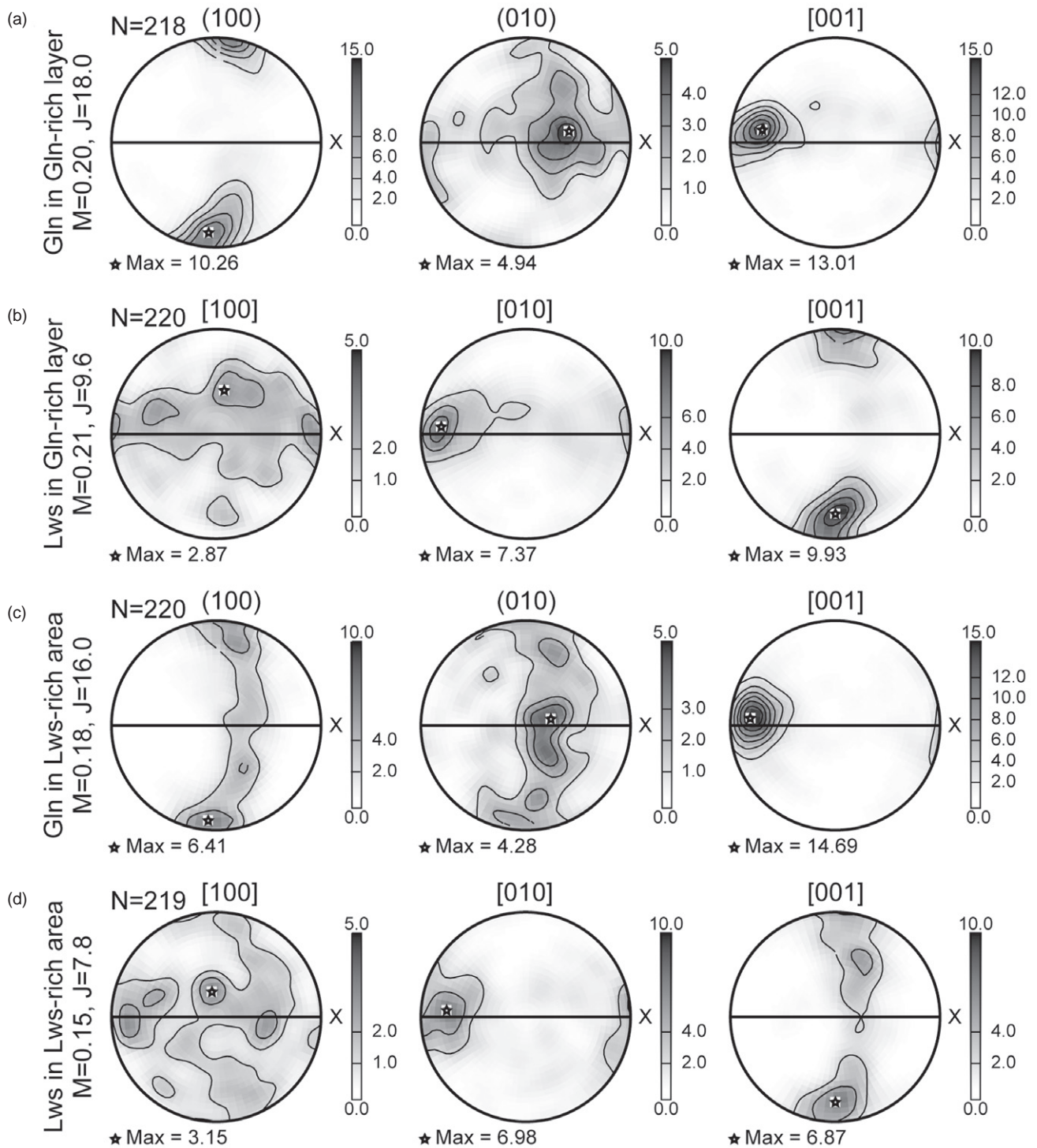


Fig. 6 Pole figures of glaucophane and lawsonite in glaucophane-rich (a and b) and lawsonite-rich (c and d) layers. Poles were plotted employing equal-area projection in lower hemisphere. Density of poles was expressed as contours by the multiples of uniform distribution (m.u.d.). The bold line in the middle of poles and X-axis presents the directions of foliation and lineation, respectively.

3.74–4.19 km/s for lawsonite ($AV_P = 8.8\%$ and $AV_S = 19.4\%$), respectively (Fig. 7c,d). The V_{Pmax} of glaucophane in both layers is developed along the lineation parallel to the [001] axes and the AV_{Smax} and V_{S1max} polarization are established as

girdle type along the foliation perpendicular to the (100) planes in CPOs, while lawsonite shows V_{Pmax} normal to the foliation associated with the [001] axes and AV_{Smax} and V_{S1max} polarization in central maxima.

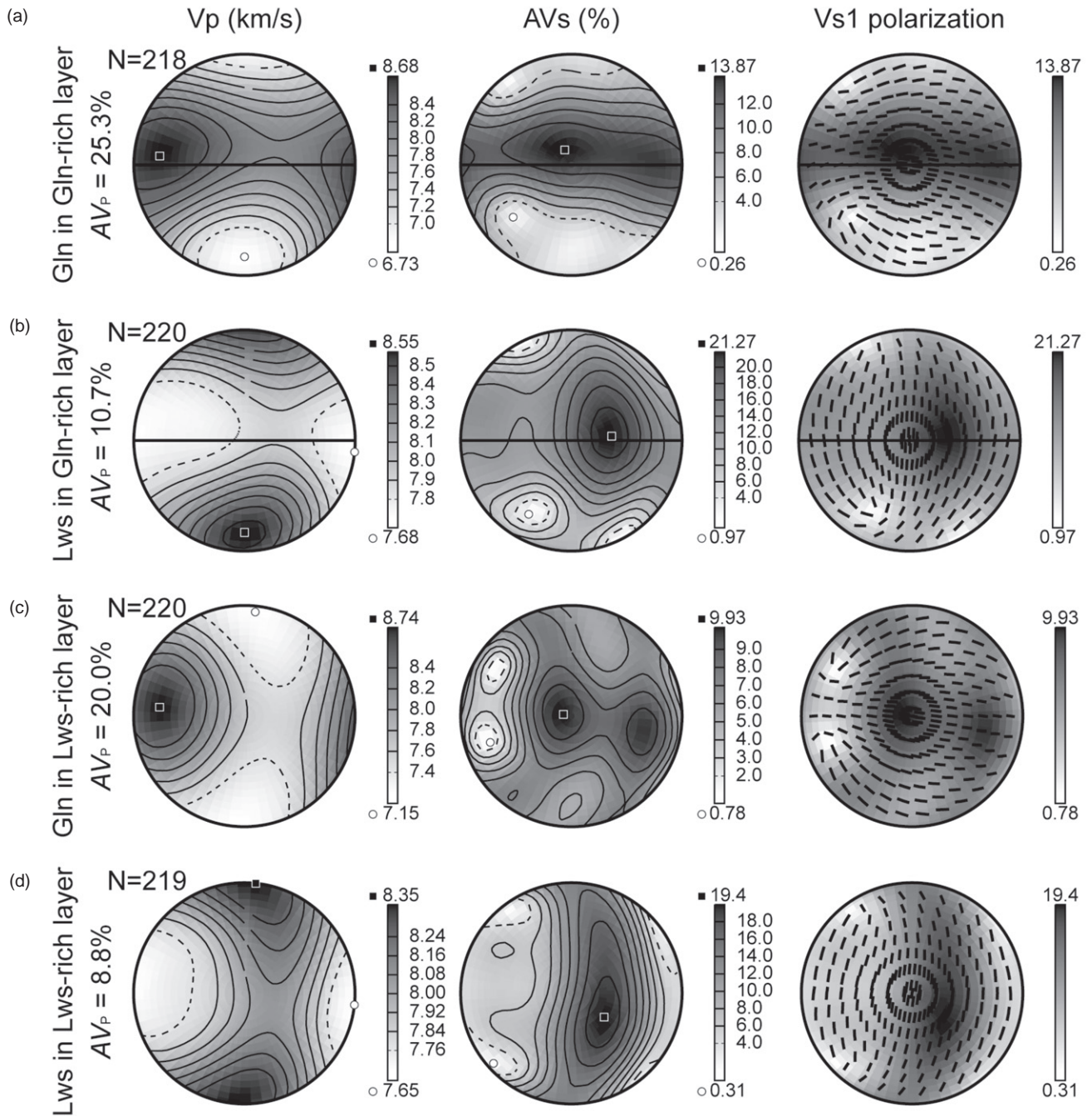


Fig. 7 Computed seismic anisotropy of glaucophane (a, c) and lawsonite (b, d) in the glaucophane-rich and lawsonite-rich layers, respectively. Equal area projection and the Voigt–Reuss–Hill averaging scheme were employed in lower hemisphere.

DISCUSSIONS

DEFORMATION MECHANISMS OF GLAUCOPHANE AND LAWSONITE

Microstructural investigations suggested cataclastic deformation (Nyman *et al.* 1992), rigid-body rotation (Ildefonse *et al.* 1990; Siegesmund *et al.* 1994), and dynamic recrystallization (Cumbest

et al. 1989) as possible deformation mechanisms of natural amphibole. Glaucophane is a relatively weak mineral among amphiboles, attributed to diverse slip systems and an inclination for recovery and recrystallization processes (Reynard *et al.* 1989; Zucali *et al.* 2002). In addition, small grain size is normally attributed to strain-induced recrystallization during or after crystal plastic deformation (e.g., Drury & Urai 1990).

Glauconite in the analyzed samples shows small grain size (possibly owing to grain size reduction) and well-developed CPOs normally considered as products of dynamic recrystallization (Díaz Aspiroz *et al.* 2007). The result can be also supported by the grain size distribution of glauconite into $<2\ \mu\text{m}$ and $4\text{--}22\ \mu\text{m}$ for the LRL, and possibly $<2\ \mu\text{m}$ and $4\text{--}14\ \mu\text{m}$ for the GRL (Fig. 5). Glauconite is, therefore, likely to have been deformed by recovery and dynamic recrystallization mechanisms, perhaps accommodated by dislocation creep. Irregular or curved grain boundaries of glauconite designate the presence of annealing and grain growth ascribed to the reduction of interfacial free energy in a low stress regime (Fig. 3b) (Evans *et al.* 2001). Dissolution and precipitation creep can be operated under low temperatures in the presence of aqueous fluids; however, this may not be the main controlling mechanism for the analyzed sodic amphiboles because of the stronger fabric for fine-grained glauconite and weak chemical zoning, whereas calcic amphiboles are deformed by dissolution and precipitation, as evident by shape preferred orientation and clear chemical zoning (e.g., Imon *et al.* 2004). The deformation mechanism of lawsonite, on the other hand, is poorly understood. Lawsonite in the sample also exhibits relatively strong CPOs, however, grains are euhedral with angular or straight boundaries and are partly wrapped by phengite (Fig. 2). The wide range of the stability field of lawsonite with these microstructures intimates that the predominant deformation mechanism is likely to be rigid body rotation.

DEFORMATION CONDITIONS FOR THE DIABLO RANGE BLUESCHIST

Lawsonite eclogite normally occurs at deeper than 45 km depth in subduction zones (Tsujimori *et al.* 2006), nevertheless its exhumation to the surface is rare without alteration. The Diablo Range exceptionally maintains unaltered lawsonite eclogite, implying rapid exhumation probably due to slab breakoff. Lawsonite in the analyzed sample might have been formed during prograde metamorphism and suffered the maximum pressure condition (1.3 GPa) of the New Idria serpentinite body (Tsujimori *et al.* 2007). On the other hand, glauconite may have appeared during a retrograde P – T path based on the chemical compositions of the core (glauconite) and rim (winchite or actinolite). The strongly aligned grains for both lawsonite and glauconite are proved by low degrees of angle

to the foliation (Fig. 5), indicating the presence of deformation during or after the blueschist-facies overprinting. The development of CPO might be imputed to the flow of dynamically recrystallized small grains, suggesting syn-kinematic microstructures. Consequently the main deformation event that formed these microstructures occurred at temperatures ranging from 200 to 290°C and pressures over 1.0 GPa (Tsujimori *et al.* 2007). The deformation at a relatively high pressure may cause the operation of plastic deformation in sodic amphibole rather than the cataclastic deformation.

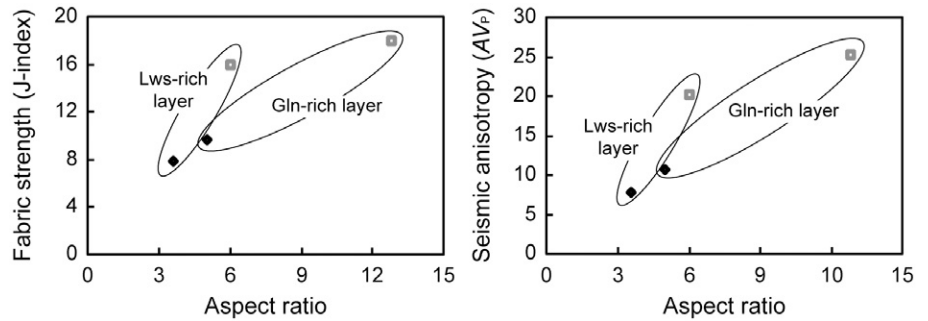
RHEOLOGICAL CONTRAST BETWEEN GLAUCOPHANE AND LAWSONITE

Deformation is generally concentrated into specifically weak minerals or layers (e.g., Ebert *et al.* 2007), therefore the strength contrast between glauconite and lawsonite against deformation can help to understand the rheology of the subducting slab. For examining this concept, we assume that the analyzed rock is composed only of two phases, glauconite and lawsonite. Microscopic observations designate that grains of glauconites and lawsonite in the GRL are comparatively small compared with those in the LRL (Fig. 2). The results of image analyses for glauconite and lawsonite in the GRL intimate higher aspect ratios, larger grain size, and alignment of the longaxes along foliation than those in the LRL (Fig. 5). Higher fabric strength in the GRL is also revealed based on M- and J-indexes, which is corresponding to aspect ratio (Fig. 8 and Table 2). All evidence demonstrates that strain is localized into the GRL rather than the LRL, denoting glauconite as weaker than lawsonite against deformation. Our study, therefore, proves that the rheology of subducting oceanic crusts can be primarily influenced by glauconite. This is in agreement with the results of Teyssier *et al.* (2010) who reported lawsonite vorticity owing to the treatment of lawsonite and glauconite as a rigid grain and a ductile matrix, respectively.

SLIP SYSTEMS AND SEISMIC ANISOTROPY

Slip systems are usually managed by physical variables such as pressure (P), temperature (T), stress (strain or strain rate), and water fugacity (Carter & Avé Lallemand 1970; Jung & Karato 2001; Jung *et al.* 2006). The sample analyzed experienced almost comparable histories for P , T , and water

Fig. 8 Comparisons of fabric strength, seismic anisotropy and aspect ratio. Calculations of fabric strength (J-index) follow Mainprice and Silver (1993) and P-wave seismic anisotropy was computed using the software ANISctf made by D. Mainprice. □, Gln; ◆, Lws.



fugacity hence, in this study, strain could be the only concern for slip systems of glaucophane in the GRL and the LRL. Pole figures of glaucophane show vertical maxima in the (100) planes and horizontal maxima in the [001] axes, insinuating slip plane and direction, respectively (Fig. 5a,c). The results advocate that the strength of stress or strain can scarcely influence the slip systems of glaucophane. Duplicate glaucophane LPOs, which can be used for estimating the slip system, are reported for lawsonite blueschists deformed at 2 GPa and 430°C (Teyssier *et al.* 2010) and at 0.7–0.9 GPa and <350°C (Fujimoto *et al.* 2010). These reveal the same slip systems as glaucophane in diverse P – T conditions when other factors (strain and water fugacity) are fixed, therefore glaucophane possibly has identical slip systems during both subduction and exhumation.

The CPOs of lawsonite show the [010] axis sub-parallel to the lineation and the [001] axis normal to the foliation, possibly developed by solid body rotation (Fig. 5b,d). This pattern is different from that reported in lawsonite, (100)[001] (Teyssier *et al.* 2010) and (001)[100] (Fujimoto *et al.* 2010). These disagreements are probably attributable to the difference in deformation mechanism, deformational P – T conditions, or degree of rotation, nevertheless strain rate, stress (or strain), and water fugacity should also be contemplated.

To evaluate impacts of strain localization on seismic anisotropy, we computed the seismic properties of glaucophane and lawsonite in the GRL and LRL (Fig. 7). The degree of seismic anisotropy of glaucophane and lawsonite in the LRL are relatively low compared with those in the GRL, in agreement with the aspect ratios and fabric strengths (Fig. 7 and Table 2). Those are mainly caused by strain localization, because they were calculated from CPOs. However glaucophane and lawsonite have different CPOs, therefore seismic anisotropy of the rock masses were computed in order to comprehend the effects of mineral abun-

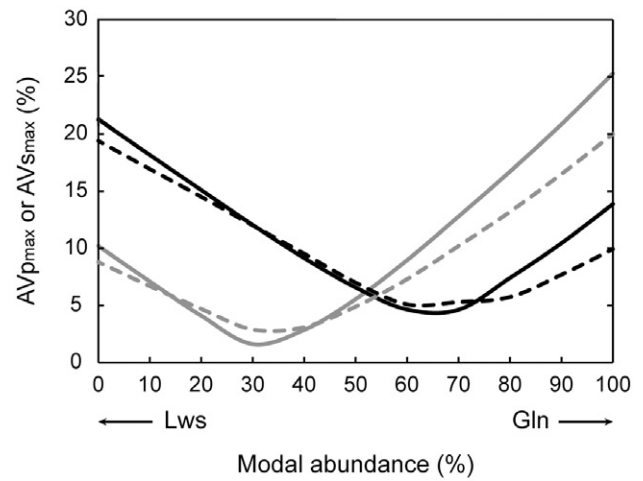


Fig. 9 A graph for P- and S-wave seismic anisotropy according to modal abundance. The AV_p of both layers is the strongest for the rock composed of 100% glaucophane, decreases with the increase of lawsonite abundance, and finally reaches to minimum value when the rock comprises 30% of glaucophane. The opposite patterns are characterized for the AV_s . Therefore the concave shapes are possibly attributed to different propagating directions between P- and S-waves. The calculations of seismic properties were conducted with every 10% step. —, AV_p in Gln-rich layer; - - , AV_p in Lws-rich layer; —, AV_s in Gln-rich layer; - - , AV_s in Lws-rich layer.

dances (Fig. 9) (Mainprice *et al.* 2000). The highest AV_{pmax} for the GRL and LRL were calculated as 20.0 and 25.3%, respectively, for the rock comprising 100% glaucophane, while the highest AV_{smax} were 19.4 and 21.3%, respectively, for the rock containing 100% lawsonite. The lowest AV_{pmax} and AV_{smax} are modeled as the rock composed of 70% glaucophane and 30% lawsonite for AV_p , and of 30% glaucophane and 70% lawsonite. The distinctive ‘concave’ feature is probably attributable to directions of seismic anisotropy originating from CPOs (Figs 6,7). Consequently we denote here that seismic anisotropy of a rock mass, especially one composed of highly anisotropic phases, is controlled by the abundance of rock-forming minerals.

CONCLUSIONS

In summary, we investigated fabric analyses of a Diablo Range blueschist, which preserves two distinctive layers mostly composed of glaucophane and lawsonite. Results show higher aspect ratios, lower angles to the foliation, and higher fabric strengths for glaucophane in the representative two layers, advocating strain partitioning into the glaucophane-rich layer (GRL) rather than the lawsonite-rich layer (LRL), and also indicating the weakness of glaucophane against deformation compared with lawsonite. To conclude, our discovery supports the idea that glaucophane mainly manages rheology and seismic anisotropy of subducting oceanic crusts.

ACKNOWLEDGEMENTS

The authors appreciate the assistance of H. Rehman, Y. Soda and H. Yamamoto for constructive comments, and K. Okamoto for editing. We are also grateful to Y. Shibata and L.F.G. Morales for technical support on the EPMA analyses and seismic property calculations, respectively. This project has been supported by the Japan Society for the Promotion of Science (JSPS) to IK (No. 21684030), KM (No. 22244062) and TT (No. 22654058).

REFERENCES

- BEZACIER L., REYNARD B., BASS J. D., WANG J. & MAINPRICE D. 2010. Elasticity of glaucophane, seismic velocities and anisotropy of the subducted oceanic crust. *Tectonophysics* **494**, 201–10.
- CARTER N. L. & AVÉ LALLEMANT H. G. 1970. High temperature deformation of dunite and peridotites. *Geological Society of America Bulletin* **81**, 2181–202.
- COLEMAN R. G. 1980. Tectonic inclusions in serpentinite. *Archives des Sciences, Société de Physique et d'Histoire Naturelle de Genève* **33**, 89–102.
- COLEMAN R. G. 1996. New Idria Serpentinite: A land management dilemma. *Environmental & Engineering Geoscience* **2**, 9–22.
- CUMBEST R. J., DRURY M. R., VAN ROERMUND H. L. M. & SIMPSON C. 1989. Dynamic recrystallization and chemical evolution of clinoamphibole from Senja Norway. *Contributions to Mineralogy and Petrology* **101**, 339–49.
- DÍAZ ASPIROZ M., LLOYD G. E. & FERNÁNDEZ C. 2007. Development of lattice preferred orientation in clinoamphiboles deformed under low-pressure metamorphic conditions. A SEM/EBSD study of metabasites from the Aracena metamorphic belt (SW Spain). *Journal of Structural Geology* **29**, 629–45.
- DRURY M. R. & URAI J. L. 1990. Deformation-related recrystallization processes. *Tectonophysics* **172**, 235–53.
- EBERT A., HERWEGH M. & PFIFFNER A. 2007. Cooling induced strain localization in carbonate mylonites within a large-scale shear zone (Glarus thrust, Switzerland). *Journal of Structural Geology* **29**, 1164–84.
- EVANS B., RENNER J. & HIRTH G. 2001. A few remarks on the kinetics of static grain growth in rocks. *International Journal of Earth Sciences* **90**, 88–103.
- FUJIMOTO Y., KONO Y., HIRAJIMA T., KANAGAWA K., ISHIKAWA M. & ARIMA M. 2010. P-wave velocity and anisotropy of lawsonite and epidote blueschists: Constraints on water transportation along subducting oceanic crust. *Physics of the Earth and Planetary Interiors* **183**, 219–28.
- ILDEFONSE B., LARDEAUZ J.-M. & CARON J.-M. 1990. The behavior of shape preferred orientations in metamorphic rocks: Amphiboles and jadeites from the Monte Mucrone area (Sesia-Lanzo zone, Italian Western Alps). *Journal of Structural Geology* **12**, 1005–11.
- IMON R., OKUDAIRA T. & KANAGAWA K. 2004. Development of shape- and lattice-preferred orientations of amphibole grains during initial cataclastic deformation and subsequent deformation by dissolution-precipitation creep in amphibolites from the Ryoke metamorphic belt, SW Japan. *Journal of Structural Geology* **26**, 793–805.
- ISMAÏL W. B. & MAINPRICE D. 1998. An olivine fabric database: An overview of upper mantle fabrics and seismic anisotropy. *Tectonophysics* **296**, 145–57.
- JUNG H. & KARATO S.-I. 2001. Water-induced fabric transitions in olivine. *Science* **293**, 1460–3.
- JUNG H., KATAYAMA I., JIANG Z., HIRAGA T. & KARATO S. 2006. Effect of water and stress on the lattice-preferred orientation of olivine. *Tectonophysics* **421**, 1–22.
- LEAKE B. E., WOOLLEY A. R., ARPS C. E. S. *et al.* 1997. Nomenclature of amphiboles; Report of the Subcommittee on Amphiboles of the International Mineralogical Association, Commission on New Minerals and Mineral Names. *Canadian Mineralogist* **35**, 219–46.
- MAINPRICE D. & SILVER P. G. 1993. Interpretation of SKS-waves using samples from the subcontinental lithosphere. *Physics of the Earth and Planetary Interiors* **78**, 257–80.
- MAINPRICE D., BARRUOL G. & BEN ISMAÏL W. 2000. The anisotropy of the Earth's mantle: From single crystal to polycrystal. In Karato S., Forte A. M., Liebermann R. C., Masters G. and Stixrude L. (eds.) *Mineral Physics and Seismic Tomography: From Atomic to Global*, Geophysical Monograph 117, pp. 237–64, AGU, Washington, DC.
- MARUYAMA S. & LIOU J. G. 1988. Petrology of Franciscan metabasites along the jadeite-glaucophane

- type facies series, Cazadero, California. *Journal of Petrology* **29**, 1–37.
- MARUYAMA S., CHO M. & LIOU J. G. 1986. Experimental investigations of blueschist-greenschist transition equilibria: Pressure dependence of Al₂O₃ contents in sodic amphiboles – A new barometer. In Evans B. W. and Brown E. H. (eds.) *Blueschist and Eclogite*, Geological Society of America Memoir, 164, pp. 1–16, The Geological Society of America Inc., Colorado.
- MEZGER J. E. 2010. Rotation of irregular staurolite porphyroblasts in a simple shear dominated shear zone controlled by initial growth orientation and aspect ratio. *Journal of Structural Geology* **32**, 1147–57.
- NYMAN M. W., LAW R. D. & SMELIK E. 1992. Cataclastic deformation for the development of core mantle structures in amphibole. *Geology* **20**, 455–8.
- REYNARD B., GILLET P. & WILLAIME C. 1989. Deformation mechanisms in naturally deformed glaucophanes: A TEM and HREM study. *European Journal of Mineralogy* **1**, 611–24.
- SIEGSMUND S., HELMING K. & KRUSE R. 1994. Complete texture analysis of a deformed amphibolite: Comparison between neutron, diffraction and U-stage data. *Journal of Structural Geology* **16**, 131–42.
- SINOGEIKIN S. V. & BASS J. D. 2000. Single-crystal elasticity of pyrope and MgO to 20 GPa by Brillouin scattering in the diamond cell. *Physics of the Earth and Planetary Interiors* **120**, 43–62.
- SKEMER P., KATAYAMA I., JIANG Z. & KARATO S. 2005. The misorientation index: Development of a new method for calculating the strength of lattice-preferred orientation. *Tectonophysics* **411**, 157–67.
- TEYSSIER C., WHITNEY D. L., TORAMAN E. & SEATON N. C. A. 2010. Lawsonite vorticity and subduction kinematics. *Geology* **38**, 1123–6.
- TSUJIMORI T., SISSON V. B., LIOU J. G., HARLOW G. E. & SORENSEN S. S. 2006. Very-low-temperature record in subduction process: A review of worldwide lawsonite eclogites. *Lithos* **92**, 609–24.
- TSUJIMORI T., LIOU G. J. & COLEMAN R. G. 2007. Finding of high-grade tectonic blocks from the New Idria serpentinite body, Diablo Range, California: Petrologic constraints on the tectonic evolution of an active serpentinite diapir. In Cloos M., Carlson W. D., Gilbert M. C., Liou J. G. and Sorensen S. S. (eds.) *Convergent Margin Terranes and Associated Regions: A Tribute to W. G. Ernst*, Geological Society of America, Special Papers 419, pp. 67–80.
- WHITNEY D. L. & EVANS B. W. 2010. Abbreviations for names of rock-forming minerals. *American Mineralogist* **95**, 185–7.
- ZUCALI M., CHATEIGNER D., DUGNANI M., LUTTEROTTI L. & OULADDIAF B. 2002. Quantitative texture analysis of glaucophanite deformed under eclogite facies conditions (Sesia-Lanzo Zone, Western Alps): Comparison between X-ray and neutron diffraction analysis. *Geological Society, London* **200**, 239–53.